Lawrence Berkeley National Laboratory
LBL Dissertations

## Title

Terahertz Time Domain Interferometry of a SIS Tunnel Junction and a Quantum Point Contact

## Permalink

https://escholarship.org/uc/item/5j55r8tp

## Author

Karadi, C.

## Publication Date

1995-09-01

Thesis/dissertation

eScholarship.org Powered by the California Digital Library
University of California

LBL-37935
UC-404

# Lawrence Berkeley Laboratory

UNIVERSITY OF CALIFORNIA

## Materials Sciences Division

**Terahertz Time Domain Interferometry of a SIS Tunnel Junction and a Quantum Point Contact**

C. Karadi
(Ph.D. Thesis)

September 1995

REFERENCE COPY
Does Not Circulate
Bldg. 50 Library.
LBL-37935
Copy 1

**Prepared for the U.S. Department of Energy under Contract Number DE-AC03-76SF00098**

**DISCLAIMER**

This document was prepared as an account of work sponsored by the United States Government. While this document is believed to contain correct information, neither the United States Government nor any agency thereof, nor the Regents of the University of California, nor any of their employees, makes any warranty, express or implied, or assumes any legal responsibility for the accuracy, completeness, or usefulness of any information, apparatus, product, or process disclosed, or represents that its use would not infringe privately owned rights. Reference herein to any specific commercial product, process, or service by its trade name, trademark, manufacturer, or otherwise, does not necessarily constitute or imply its endorsement, recommendation, or favoring by the United States Government or any agency thereof, or the Regents of the University of California. The views and opinions of authors expressed herein do not necessarily state or reflect those of the United States Government or any agency thereof or the Regents of the University of California.

LBL-37935
UC-404

# Terahertz Time Domain Interferometry of a SIS Tunnel Junction and a Quantum Point Contact

Chandu Karadi

Department of Physics
University of California, Berkeley

and

Materials Sciences Division
Lawrence Berkeley Laboratory
University of California
Berkeley, California 94720

September 1995

This work was supported by the Director, Office of Energy Research, Office of Basic Energy Sciences, Materials Sciences Division, of the U.S. Department of Energy under Contract No. DE-AC03-76SF00098.

# Terahertz Time Domain Interferometry of a SIS Tunnel Junction and a Quantum Point Contact

by

Chandu Karadi

A.B. (University of California at Berkeley) 1989
M.S. (University of California at Berkeley) 1991

A dissertation submitted in partial satisfaction of the
requirements for the degree of
Doctor of Philosophy

in

Physics

in the

GRADUATE DIVISION
of the
UNIVERSITY of CALIFORNIA at BERKELEY

Committee in charge:

Professor Joseph Orenstein, Chair
Professor Daniel Chemla
Professor John R. Whinnery

1995

This work was supported in part by the Director, Office of Energy Research, Office of Basic Energy Sciences, Materials Sciences Division of the U.S. Department of Energy under Contract No. DE-AC-03-76SF00098.

# Terahertz Time Domain Interferometry of a SIS Tunnel Junction and a Quantum Point Contact

Copyright © 1995

by

Chandu Karadi

The U.S. Department of Energy has the right to use this document
for any purpose whatsoever including the right to reproduce
all or any part thereof

**Abstract**

Terahertz Time Domain Interferometry of a
SIS Tunnel Junction and a Quantum Point Contact

by

Chandu Karadi

Doctor of Philosophy in Physics

University of California at Berkeley

Professor Joseph Orenstein, Chair

We have applied the Terahertz Time Domain Interferometric (THz-TDI) technique to probe the ultrafast dynamic response of a Superconducting-Insulating-Superconducting (SIS) tunnel junction and a Quantum Point Contact (QPC). The THz-TDI technique involves monitoring changes in the *dc* current induced by interfering two picosecond electrical pulses on the junction as a function of time delay between them. Measurements of the response of the Nb/$AlO_x$/Nb SIS tunnel junction from 75-200 GHz are in full agreement with the linear theory for photon-assisted tunneling. Likewise, measurements of the induced current in a QPC as a function of source-drain voltage, gate voltage, frequency, and magnetic field also show strong evidence for photon-assisted transport. These experiments together demonstrate the general applicability of the THz-TDI technique to the characterization of the dynamic response of any micron or nanometer scale device that exhibits a non-linear I-V characteristic.

Professor Joseph Orenstein
Dissertation Committee Chair

To my daughters

Tasha-Miyo and Reiko-Amrita

# Contents

**List of Figures** vi

**Acknowledgments** ix

**1. Introduction** 1
- 1.1 Terahertz Spectroscopy 1
- 1.2 Historical Development 3
- 1.3 Terahertz Time Domain Interferometry (THz-TDI) 5
- 1.4 References 8

**2. The Terahertz Technique** 11
- 2.1 Terahertz Source 11
- 2.2 Source Fabrication 13
- 2.3 Theory of Source Operation 16
- 2.4 Source Detection 22
- 2.5 Experimental Source Characterization 23
- 2.6 Device Characterization: Terahertz Time Domain Interferometry 26
  - 2.6.1 Device Admittance 26
  - 2.6.2 Quasioptical Coupling 27
  - 2.6.3 Diode Rectification 29
  - 2.6.4 Terahertz Interferometry 31
- 2.7 Summary 34
- 2.8 References 34
- 2.9 Figure Captions 37
- Figures 38

**3. High Frequency Response of Superconducting Tunnel Junctions: Theory** 49
- 3.1 BCS Theory 49
- 3.1 Superconducting Tunneling 52
- 3.3 High Frequency Response 56
- 3.4 Quantum Efficiency 69
- 3.5 Summary 70
- 3.6 References 70
- 3.7 Figure Captions 72
- Figures 74

**4 . High Frequency Response of Superconducting Tunnel Junctions: Experiment** 81
- 4.1 Introduction 82
- 4.2 SIS Time Domain Interferometer 85

4.3 SIS Junction Fabrication 88
4.4 Single Pulse Experiments 90
4.5 Linear Response: THz-TDI 93
4.6 Nonlinear Spectroscopy - Preliminary Experiments 96
4.7 Summary 102
4.8 References 102
4.9 Figure Captions 104
Figures 106

**5. The Quantum Point Contact: *dc* and High Frequency Transport Theory** 116
5.1 *dc* Transport 117
5.1.1 Fabrication of QPC Device 117
5.1.2 QPC: Quantized Conductance and Nonlinear $I_{dc}$-$V_{sd}$ Curves-Experiment 119
5.1.3 QPC: Quantized Conductance and Nonlinear $I_{dc}$-$V_{sd}$ Curves-Theory 120
5.2 *ac* Transport 126
5.2.1 Buttiker-Landauer Approach: Traversal Time for Tunneling 127
5.2.2 Tien Gordon Approach 130
5.3 Conclusions 134
5.4 References 134
5.5 Figure Captions 137
Figures 138

**6. High Frequency Response of Quantum Point Contact Experiment** 144
6.1 Introduction 144
6.2 The First Terahertz Interferometric Measurements of a QPC 148
6.2.1 QPC Device Fabrication 148
6.2.2 Terahertz Detection 149
6.2.3 Terahertz Spectroscopy-Source/Drain Experiment-Zero Magnetic Field 150
6.2.4 Terahertz Spectroscopy - Magnetic Field Dependence 156
6.2.5 Conclusions 157
6.3 Terahertz Interferometric Measurements of a Mesoscopic Tunnel Barrier 158
6.3.1 Improved Terahertz Spectrometer 158
6.3.2 Antenna-Transmission Line Coupling 160
6.3.3 Device Under Study 162
6.3.4 *dc* Transport 163
6.3.5 Single Pulse Experiment 164
6.3.6 Terahertz Interferometry-Gate Voltage Experiment-Zero Magnetic Field 166
6.3.7 Terahertz Interferometry-Magnetic Field Dependence 171
6.4 Conclusions 175
6.5 References 176
6.6 Figure Captions 180
Figures 183

**7. Conclusions** 200
7.1 References 201

# List of Figures


2.1 Auston dipole antenna source . . . . . . . . . . . . . . . . . . . . . . . 38

2.2 Auston switch fabrication . . . . . . . . . . . . . . . . . . . . . . . . . . . 40

2.3 Electrical pulse generation . . . . . . . . . . . . . . . . . . . . . . . . . . . 41

2.4 Improved radiation coupling with silicon lens . . . . . . . . . . . . 42

2.5 Terahertz Time Domain Spectrometer . . . . . . . . . . . . . . . . . . 43

2.6 Time domain and spectrum of a terahertz pulse . . . . . . . . . . . . 44

2.7 Improved radiation coupling with dipole antenna . . . . . . . . . . . . 46

2.8 Norton equivalent circuit for antenna coupled device . . . . . . 47

2.9 Terahertz Time Domain Interferometer . . . . . . . . . . . . . . . . . . 48

3.1 SIS tunnel junction density of states . . . . . . . . . . . . . . . . . . . . . . . 74

3.2 *dc* I-V curve and Kramers-Kronig transform . . . . . . . . . . . . 75

3.3 SIS tunnel junction density of states in presence of microwave field and pumped V-I curve . . . . . . . . . . . . . . . . . . . . . . . . . . . . 76

3.4 Generation of photonic sidebands . . . . . . . . . . . . . . . . . . . . . . . 77

3.5 Graphical method for calculating quantum conductance . . . . . . 78

3.6 Quantum conductance *vs.* frequency . . . . . . . . . . . . . . . . . . . . . . . 79

3.7 Quantum susceptance *vs.* frequency . . . . . . . . . . . . . . . . . . . . . . . 80

4.1 Beam splitter efficiency . . . . . . . . . . . . . . . . . . . . . . . . . . . . . . . 106

4.2 Bolometric measurements of a terahertz pulse . . . . . . . . . . . . 107

4.3 Cross section diagram of SIS tunnel junction ............ 108
4.4 Circular log periodic antenna ....................... 109
4.5 Rectified current in an SIS tunnel junction with a single picosecond electrical pulse ................................... 110
4.6 Rectified current *vs.* terahertz electric field .................. 111
4.7 Terahertz Time Domain Interferometry of an SIS tunnel junction... 112
4.8 Normalized frequency response of an SIS tunnel junction ...... 113
4.9 Nonlinear Terahertz Time Domain Interferometry ............ 114
4.10 Odd and even portions of nonlinear interferograms ............ 115
5.1 Implementation of a QPC in a GaAs-AlGaAs heterostructure..... 138
5.2 *dc* transport properties of a QPC ......................... 139
5.3 Potential barrier for a QPC ............................. 140
5.4 *ac* transport in the Buttiker-Landauer picture ............ 141
5.5 *ac* transport in the Tien-Gordon picture .................. 143
6.1 Conductance steps in a QPC including depletion ............ 183
6.2 Conductance steps in a QPC........................... 183
6.3 Rectified current in a QPC ............................ 184
6.4 Terahertz time domain interferometry of a QPC, source-drain voltage dependence ....................................... 185
6.5 Normalized frequency response of a QPC, source-drain voltage dependence ....................................... 186
6.6 Time domain interferograms of a QPC in a magnetic field ...... 187
6.7 Rectified response of a QPC *vs.* magnetic field ............ 188
6.8 QPC Terahertz Time Domain Interferometer ............ 189
6.9 Antenna/Transmission line coupling ...................... 190
6.10 Scanning electron micrograph of tunnel barrier device ...... 191
6.11 Rectified response in a tunnel barrier .................. 192

6.12 Spectral response of a tunnel barrier *vs*. gate voltage ...... 193

6.13 Tien-Gordon picture for *ac* transport in a tunnel barrier ...... 194

6.14 Barrier height and broadening *vs*. gate voltage ............ 195

6.15 Rectified response in a tunnel barrier *vs*. magnetic field ...... 196

6.16 Spectral response of a tunnel barrier *vs*. magnetic field ...... 197

6.17 Spectral response at two closely spaced magnetic field points..... 198

6.18 Spectral response of a tunnel barrier *vs*. gate voltage at B=1 T..... 199

**Acknowledgments**

Over the past six years, I have many people to thank for helping me through my thesis work. First and foremost, I would like to thank my daughters Tasha and Rita for all their help in and outside the lab. Their constant enthusiasm provided endless support. With them, I could spend my weekends in the park, by the pool, or on the beach, rather than in the lab. *All* my parents deserve special mention for helping me in any way they possibly could. My advisor, Professor Joseph Orenstein, taught me the value of choosing carefully amongst the morass of research topics. There are an endless number of research problems in this world, but only a few are worth solving. Also, I owe special thanks to Professor Paul McEuen and Dr. Leo Kouwenhoven for their expertise in mesoscopic physics.

Many thanks go to the members of my research group and the LBNL Building 2 lunch bunch. Beth Parks taught me to always look at the world with optimism and Sandeep Jauhar was there to lend a thoughtful ear. David Botkin's desserts could pick me up on a late Friday afternoon. When the wind was up, Gino Segre would always be willing to go windsurfing down at the Berkeley Marina. Rich Mallozzi provided a steady supply of Snapple. David Klein could be counted on for delicious homemade Thai food and great home brewed beer. Dr. Shimon Weiss taught me that even a jet fighter pilot can become a respected physicist.

My committee members, Daniel Chemla, John R. Whinnery, and Steven Louie also deserve special thanks. Daniel Chemla gave me insights into nonlinear optics and politics in Washington. John Whinnery, through his course on electricity and magnetism and his outstanding book, *Fields and Waves in Communication Electronics*, gave me an intuitive grasp of antennas, transmission lines, and electro-magnetism. Steven Louie provided me with a sound foundation in solid state physics.

Lastly I would like to thank all my friends from the supermarket gang for being there. Peter and Penny - Good luck ! I know you will have a great time together. Sam Kao taught me about surgeons and sailing on the San Francisco bay. Jeff Chuang pointed out that an artist doesn't have to starve in New York city. Vivienne gave me new hope that I might live out my days in Hawaii.

This work was supported in part by the Director, Office of Energy Research, Office of Basic Energy Sciences, Materials Sciences Division of the U.S. Department of Energy under Contract No. DE-AC-03-76SF00098.

# Chapter 1

# Introduction

## 1.1 Terahertz Spectroscopy

The terahertz, or far-infrared, region of the electromagnetic spectrum is of critical importance in the spectroscopy of condensed matter systems. For example, the electronic properties of semiconductors, superconductors, and metals are greatly influenced by bound states (excitons, Cooper pairs) with binding energies in the meV range, which corresponds to frequencies in the terahertz regime. Terahertz frequencies are also well matched to typical quasiparticle scattering rates and barrier traversal times. In addition, confinement energies in artificially synthesized 2-dee and 1-dee nanostructures, like quantum wells and quantum point contacts, also lie in the terahertz regime.

In spite of its importance, terahertz spectroscopy has been hindered by the lack of suitable tools. Swept frequency synthesizers for millimeter and submillimeter-waves are limited to below roughly 100 GHz, with higher frequencies only available with discrete sources. On the other hand, Fourier transform infrared (FTIR) [1.1] spectroscopy

applicable above 100 GHz is hampered by the lack of brightness of incoherent sources. In addition, FTIR methods are inherently incoherent and are not applicable to time domain pump-probe spectroscopy. Lastly, FTIR methods are not useful if the real and imaginary parts of the response functions of a material must be measured simultaneously at each frequency.

However, recent developments in Terahertz Time-Domain Spectroscopy (THz-TDS) have overcome these drawbacks in a radical way [1.2]. The advantages of this new technique have resulted in a rapid expansion of research in terahertz spectroscopy. In the last few years, the field has grown from a handful of electrical engineers with expertise in ultrafast lasers to an entire cadre of researchers in a spectrum of disciplines extending from chemistry to materials science to physics. The THz-TDS method is based on electromagnetic transients generated opto-electronically with the help of femtosecond ($1 \text{ fs} = 10^{-15} \text{ s}$) duration laser pulses. These transients are single-cycle bursts of electromagnetic radiation with pulse duration ranging from less than 1 ps to 10 ps. The pulse duration may be adjusted by suitable choice of source dimensions. The pulse spectral density spans the range from below 100 GHz to more than 5 THz. Optically-gated detection allows direct measurement of the terahertz electric field with a time resolution of a few picoseconds. With this measurement technique, both the real and imaginary parts of the dielectric function of a medium may be extracted without having to resort to the Kramers-Kronig relations. As we will discuss in Chapter 2, the brightness of the THz transient greatly exceeds that of conventional thermal sources and the gated detection is as sensitive as a liquid helium cooled bolometer.

Recent developments in the field have shown that THz-TDS also has capabilities far beyond linear far-infrared spectroscopy. Because the THz transients are perfectly time-synchronized with the optical pulses that generate them, THz-TDS is ideally suited for "visible pump, THz-probe" experiments [1.3]. In these measurements, the optical pulse is used to excite the sample and the THz pulse probes the change in the dielectric function as a

function of time delay after optical excitation. Another powerful nonlinear probe is the detection of THz emission following pulsed laser excitation [1.4]. In many cases, these nonlinear techniques are proving even more powerful than linear THz-TDS.

Beyond the characterization of new materials and the study of basic physical phenomena, the impact of THz spectroscopy in the commercial world is growing. Promising applications include industrial process control, contamination measurements, chemical analysis, wafer characterization, and remote sensing. At a recent conference, Hu and Nuss [1.5] demonstrated that the THz-TDS technique, due to its exceptionally high signal to noise ratio and the ability to focus the THz beam to the diffraction limit, is especially well suitable to imaging applications. They showed THz images of an IC package, a leaf, and a slice of bacon. Their results indicate that the THz-TDS technique has the potential to be applied to safe "X-Ray" inspection, food inspection, medical tissue diagnosis, and biomedical imaging.

## 1.2 Historical Development

THz-TDS is a relatively young field which began in the early 1980's. Unlike other spectroscopic techniques that have evolved more incrementally, we can clearly identify the technological breakthroughs that have enabled this technique to flourish. First and foremost, femtosecond laser sources within the last few years have become widely available commercially and can now be easily operated by a non-specialist in laser technology. In the past, only dye lasers were capable of generating optical pulses of roughly 100 fs duration. The industry workhorse of that time was the colliding pulse mode locked laser (CPM) [1.6] which could easily produce 100 fs pulses with an average power in the range of 25 mW. The CPM system, although reliable, required a research group to invest a substantial amount of time in developing expertise in laser technology. Today the situation has changed dramatically with the advent of solid state lasers like the Ti-Sapphire laser [1.7] which easily delivers 100 fs pulses at wavelengths near 800 nm.

This system has largely displaced the CPM systems of the past. This development is mainly due to the fact that the Ti-Sapphire laser is practically a turn-key system, delivers average power levels in excess of 500 mW, and does not require the mixing of toxic dyes. A second technological breakthrough has been in the development of new materials such as low-temperature GaAs [1.8] and poled polymers doped with chromophores [1.9] which have helped to cross fertilize research in the area of optics and electronics. Lastly advances in micro and nanofabrication have allowed the development of transmission line structures which minimize the loss of bandwidth of propagating optoelectronic signals [1.10].

The union of these enabling technologies has been dubbed Ultrafast Optoelectronics [1.11]. Initially, electrical pulses were generated and detected on transmission lines using photoconductors excited by laser pulses [1.12]. Picosecond microwave pulses in free space were first generated by coupling these electrical pulses to a microwave antenna [1.13]. Simultaneously with the development of shorter and shorter laser pulses, advances in VLSI lithographic techniques allowed the fabrication of smaller radiating structures and consequently higher frequency electromagnetic radiation. This development culminated in the generation of terahertz bandwidth single-cycle pulses by photoconducting dipole antennas [1.14]. Although these devices are broadband, they are marginally useful because they radiate isotropically. A breakthrough came with the addition of a substrate lens to couple the radiation in and out of the photoconducting dipole chip. The lens dramatically improved the directionality and efficiency [1.15] of the dipole antenna. This opened the way to *terahertz beams* which could be collimated and focused as easily as light beams in a spectrometer [1.2].

It is interesting to note that in parallel to the development of THz bandwidth photoconductive dipole antennas, THz electromagnetic transients were also generated by optical rectification in electro-optic crystals like $LiTaO_3$. These crystals also allowed for simultaneous electro-optic detection of the terahertz transients [1.16]. Because of the

difficulty of coupling the THz radiation in and out of the electro-optic crystals, this technique has been completely displaced by the photoconductive antenna approach.

## 1.3 Terahertz Time-Domain Interferometry (THz-TDI)

Prior to the work described in this thesis, most research groups focused on the use of the THz-TDS technique to probe the dynamics of electronic devices. The most powerful aspect of this technique is the ability to time resolve the picosecond electrical pulse. By time resolving both the input pulse and the output pulse, the real and the imaginary parts of the device response function can be measured. This technique has been applied to probe the high speed properties of transistors in the 100's of GHz regime [1.17]. Although those experiments were highly successful, there are a number of technical obstacles which are difficult to overcome when studying novel devices which operate at ultra-low temperatures and at high magnetic fields. The fundamental obstacle to the THz-TDS method is the need to deliver a focused pulsed laser beam into a cryogenic environment.

To overcome this fundamental problem we have pioneered a new technique, Terahertz Time-Domain Interferometry (THz-TDI). This technique, a hybrid between THz-TDS and FTIR spectroscopy, is described in Chapter 2. This method is conceptually the same as FTIR in that two beams, with a variable time-delay between them, are combined with a beam-splitter and imaged onto a sample. The simplest form of a THz-TDI uses a Michelson interferometer as an FTIR. Greene *et al.* first used this technique to characterize the spectrum of terahertz pulses generated by optical excitation of a semi-insulating InP wafer [1.18]. Although it possible to time resolve the terahertz pulse with the THz-TDS technique, the measured pulse shape will depend on the response function of the receiving antenna and the photoconductive switch. Thus the true bandwidth of the terahertz pulse in free space can only be inferred with the THz-TDS technique. To find the spectral density of the terahertz source directly, Greene *et al.* substituted the thermal source in a conventional Michelson FTIR spectrometer with the terahertz source. The recombined

beam from the interferometer was imaged onto a $^4$He-cooled bolometer. The bolometer served as a square law detector with a flat frequency response throughout the terahertz regime. As the movable mirror of the Michelson is translated, the bolometer records an "interferogram", whose Fourier transform yields the product of the spectral density of the source and the response function of the detector. This experiment was able to verify that radiation from terahertz sources extends to frequencies as high as 5 THz.

Our main interest is to apply the THz-TDI technique to probe the response of conventional low temperature superconducting-insulating-superconducting (SIS) tunnel junctions [1.19] and mesoscopic systems [1.20]. Our interest in studying the SIS system is motivated by the need to make broadband measurements of the admittance of these devices. Knowledge of the frequency dependent admittance is crucial in the practical application of SIS devices as highly sensitive microwave detectors. The SIS junction has an effectively voltage tunable band gap in the meV range making it an ideal candidate for terahertz spectroscopy. In contrast to the SIS system, experimentalists have only recently started to probe the frequency dependent response functions of mesoscopic systems. These systems, like the SIS junction, have a number of interesting energy scales in the terahertz regime. Due to electrostatic confinement on the nanometer scale, energy gaps on the multi meV scale are formed. Another important energy scale is set by the barrier traversal time as defined by the Buttiker and Landauer [1.21]. This time scale is expected to be in the picosecond range making it ideal for probing with THz-TDI. Lastly collective excitations may also appear in mesoscopic devices in the THz regime.

Our approach to study these systems is a form of photocurrent spectroscopy. We replace the bolometer in the method used by Greene *et al.* [1.18], by the device under test. The device under study is contacted and biased so that its *dc* current can be monitored. At the same time the structure is irradiated with high frequency terahertz pulses. An antenna is placed on the device to maximize the coupling of the radiation from free space since the wavelength of the radiation typically greatly exceeds the size of the device. If the radiation

is resonant with the excitations of the device, its *dc* current undergoes a change. An interferogram is then recorded by measuring the *dc* current as a function of time delay between the two arms of the interferometer. The Fourier transform of the interferogram will once again lead to a spectrum which is the product of the spectral response function of the device and the spectral density of the incident pulses. By normalizing out the spectral density of the incident pulses, we can directly probe the dynamic response of the system.

The main advantage of the THz-TDI technique over the THz-TDS technique is that we do not need to bring the laser beam directly to the device. The device resides in a cryogenic environment which is highly sensitive to heating. Since the terahertz beam has an average power level on the μW scale as compared to the laser with average powers on the ten mW scale, it is highly advantageous to only deliver the THz beam to the device as opposed to the laser beam. An additional difficulty with the THz-TDS technique is that it is technically difficult to focus the laser beam to the required spot size of 5 μm inside the cryostat. For such a small spot size, focusing optics must be placed in the cryogenic sample space, making experimental adjustments extremely difficult. For the terahertz beam, the focusing requirements are much less stringent, since we only need to focus the beam to a spot size of a few mm. For the terahertz beam, the focusing optics may be placed outside the cryostat, greatly facilitating the experimental procedure. These technical advantages of the THz-TDI technique over the THz-TDS technique make it the method of choice for probing nanoscale devices in ultra-low temperature environments. The main disadvantage of the THz-TDI technique is that we lose phase information. To obtain the real and imaginary parts of the response function of the device we need to apply the Kramers-Kronig relations .

In Chapter 3 we describe the application of the THz-TDI technique to make the first measurements of the broadband response of an SIS junction [1.22] The photocurrent in these devices results from photon-assisted tunneling of quasiparticles from one side of the junction to the other. The threshold for observing photocurrent is $2\Delta$-eV, where $2\Delta$ is the

energy gap and V is the applied voltage. By tuning V, the threshold for photon absorption can be varied. Our results are in full agreement with the linear theory for photon assisted tunneling. In addition, our results confirm the importance of the quantum susceptance in determining the linear response.

We have also applied the THz-TDI technique to make the first measurements of the photocurrent spectra in a quantum point contact (QPC) [1.23]. These results are described in Chapter 6. The QPC [1.24] is a narrow nanometer scale constriction separating two regions of electron gas. The QPC was formed by defining narrow metallic gates above the two-dimensional electron gas (2DEG) in a GaAs/AlGaAs heterojunction. The QPC in the region of the constriction can be thought of as a one-dimensional wire with a tunnel barrier in the middle. We can adjust the energy of the electrons in the wire by applying a source drain voltage across the barrier. In addition we can change the barrier height by adjusting the gate voltage. Strong evidence for photon-assisted transport in these structures was found by making measurements as a function of source-drain voltage, gate voltage, and magnetic field. In addition to photon-assisted transport, we also observed spectral lines when the applied radiation was resonant with the magnetoplasmon excitations of the 2DEG.

## 1.4 References

[1.1] P.R. Griffiths and J.A. deHaseth, Fourier Transform Infrared Spectrometry. New York: John Wiley & Sons, 1986.

[1.2] M. van Exter and D. Grischkowsky, *IEEE Trans. MTT* **38**, 1684 (1990).

[1.3] J.F. Federici, B.I. Greene, P.N. Saeta, D.R. Dykaar, F. Sharifi, and R.C. Dynes, *Phys. Rev B* **46**,11153 (1992).

[1.4] H.G. Roskos, M.C. Nuss, J. Shah, K. Leo, D.A.B. Miller, A.M. Fox, S. Schmitt-Rink, and K. Kohler, *Phys. Rev. Lett.* **68**, 2216 (1992).

[1.5] B.B. Hu and M.C. Nuss, OSA Conference on Ultrafast Electronics and Optoelectronics-1995 Postdeadline Session.

[1.6] R.L. Fork, B.I. Greene, and C.V. Shank, *Appl. Phys. Lett.* **38**, 671 (1981); J.A. Valdmanis, R.L. Fork, J.P. Gordon, *Opt. Lett.* **10,** 131 (1985).

[1.7] D.E. Spence, P.N. Kean, and W. Sibbett, *Opt. Lett.* **16**, 42 (1991).

[1.8] S. Gupta, M.Y. Frankel, J.A. Valdmanis, J.F. Whittaker, G.A. Mourou, F.W. Smith, and A.R. Calawa, *Appl. Phys. Lett.* **59**, 3276 (1991).

[1.9] A. Nahata, C. Wu, J.T. Yardley, and D.H. Auston, OSA Conference on Ultrafast Electronics and Optoelectronics-1995 Postdeadline Session.

[1.10] D.R. Dykaar, A.F.J. Levi, M. Anzlowar, *Appl. Phys. Lett.* **57**, 1123 (1990).

[1.11] D.H. Auston in Ultrashort Laser Pulses and Applications-second edition, eds. W. Kaiser. New York: Springer Verlag, 183 (1993).

[1.12] D.H. Auston, *Appl. Phys. Lett.* **26**, 101 (1975).

[1.13] G. Mourou, C.V. Stancampiano, A. Antonetti, and A. Orszag, *Appl. Phys. Lett.* **39**, 295 (1981).

[1.14] D.H. Auston, K.P. Cheung, and P.R. Smith, *Appl. Phys. Lett.* **45**, 284 (1984); P.R. Smith, D.H. Auston, and M.C. Nuss, *Appl. Phys. Lett.* **24**, 255 (1988).

[1.15] C. Fattinger, D. Grischkowsky, *Appl. Phys. Lett.* **54**, 490 (1989).

[1.16] D.H. Auston and M.C. Nuss, *IEEE J. of Quan. Elec.* **24**, 184 (1988).

[1.17] M.Y. Frankel, J.F. Whitaker, and G.A. Mourou, *IEEE J. of Quan. Elec.* **28**, 2313 (1992).

[1.18] B.I. Greene, J.F. Federici, D.R. Dykaar, R.R. Jones, and P.H. Bucksbaum, *Appl. Phys. Lett.* **59**, 893 (1991).

[1.19] For a review of PAT in SIS junctions see J.R. Tucker and M.J. Feldman, *Rev. Mod. Phys.* **57**, 1055 (1985).

[1.20] For a review, see C.W.J. Beenakker and H. van Houten in Semiconductor Heterostructures and Nanostructures, edited by H. Ehrenreich and D. Turnbull. San Diego: Academic Press, 1991.

[1.21] M. Buttiker and R. Landauer, *Phys. Rev. Lett.* **49**, 1739 (1982).

[1.22] S. Verghese, C. Karadi, C.A. Mears, J. Orenstein, P.L. Richards, and A.T. Barfknecht, *Appl. Phys. Lett.* **64**, 915 (1994).

[1.23] J. Orenstein, International Workshop on Infrared and Millimeter Waves Spectroscopy, Bad Honnef, FRG 1993; J. Orenstein, Laboratory Directed Research and Development Program, *Lawrence Berkeley Lab-FY 1993* **PUB-5382**, 65 (1994); C. Karadi, S. Jauhar, L.P. Kouwenhoven, K. Wald, J. Orenstein, P.L. McEuen, Y. Nagamune, and H. Sakaki, *J. Opt. Soc. Am. B* **11**, 2566 (1994); C. Karadi, S. Jauhar, L.P. Kouwenhoven, K. Wald, J. Orenstein, P.L. McEuen, Y. Nagamune, and H. Sakaki, OSA Conference on Ultrafast Electronics and Optoelectronics-*1995 Technical Digest* **13**, 118 (1995); C. Karadi, S. Jauhar, L.P. Kouwenhoven, K. Wald, J. Orenstein, P.L. McEuen, Y. Nagamune, and H. Sakaki, *Phys. Rev. B*, (to be published).

[1.24] B. J. van Wees, H. van Houten, C. W. J. Beenakker, J. G. Williamson, L. P. Kouwenhoven, D. van der Marel, and C. T. Foxon, *Phys Rev. Lett.* **60**,848 (1988); D. A. Wharam, T. J. Thornton, R. Newbury, M. Pepper, H. Ahmed, J. E. F.Frost, D. G. Hasko, D.C. Peacock, D.A. Ritchie, and G.A.C. Jones, *J. Phys.C* **21**, L209 (1988).

# Chapter 2

# The Terahertz Technique

This Chapter provides the information needed to design terahertz pulsed sources and describes how these pulses can be used in a Terahertz Time Domain Interferometer (THz-TDI) to characterize the dynamic response of devices. We will go through the fabrication of these sources and the theory of their operation. In addition, we will discuss the design constraints for maximizing the power output of these sources. We will also describe a method for fully characterizing the temporal and power characteristics of these sources. Lastly we will discuss how these sources can be applied to the characterization of the response of an arbitrary nonlinear device in the terahertz regime.

## 2.1 Terahertz Source

It is vital to choose the right source for your specific spectroscopic application. The frequency scale of interest for our experiments range from approximately 100 GHz to a few THz. This frequency scale is set by the physical fact that most of the phenomena that we are interested in probing only appear at a relatively low temperatures. Typically we require frequencies which are much greater than $K_bT$, where $K_b$ is Boltzmann's

constant. Thus for a temperature range of one to five Kelvin, we requires frequencies in excess of 20 GHz to 100 GHz.

The most common broadband source for this frequency range is the hot lamp (black body) source. Typical radiators range from Globars and Nernst glowers to nichrome coils and high pressure mercury lamps [2.1]. The Globar works well above 3 THz, but below this range a mercury lamp is mandatory. The advantages of a black body source is that a single bulb can cover a wide frequency range. The main drawback, though, is that the source is fairly low power. These black body sources operate in the Rayleigh-Jeans limit. In this limit the power per unit bandwidth into a single mode is simply given by $K_bT_s$ where $T_s$ is the temperature of the source [2.2]. For a source temperature of 2000 K and a 1 THz bandwidth, the output power of a single mode is only 27 nW.

Rather than use a mercury source, we have chosen to use a novel source developed by David Auston. The main advantages of these sources is that they are broadband, bright, and allow for time resolved experiments. An excellent review of the field is given by Auston [2.3]. The fundamentals of the source are based on the "Auston Switch" which consists of a small piece of damaged semiconductor which bridges the leads of a biased antenna structure. Figure 2.1(a) shows a diagram of a typical antenna source. The antenna is connected to a long transmission line which is biased with a battery (typically 50 V to 100 V). The resistance of the silicon switch is high when it is unilluminated. In this state the gap charges up to the applied biased voltage, $V_A$. The switch is then closed with a short 100 fs optical pulse allowing a fast picosecond current transient to pass across the gap and through the antenna terminals. The current transient excites the antenna and leads to the emission of single cycle sine wave with a period which depends on the length of the antenna. A typical 300 $\mu$m long antenna produces a bipolar pulse with a duration of roughly 6 ps. This pulse has a center frequency of

180 GHz and a bandwidth of 150 GHz. We will go through the details of the switch performance later, but first let us consider the steps necessary in fabricating the source.

## 2.2 Source Fabrication:

In this subsection we will go through a detailed description of the fabrication process. Figure 2.1(b) shows a detailed diagram of our antenna source. We will begin with a discussion of the photolithographic steps in processing the silicon box and the metallic lines. This will be followed by a description of the silicon damage process.

There are a number of different types of photoconductors that can be used to form the switch. Typical materials are damaged GaAs [2.4], low temperature (LT) GaAs [2.5], and damaged silicon on sapphire (SOS) [2.6]. We use a silicon photoconductor grown on a sapphire wafer following a fabrication process developed by Ketchen *et al.* [2.7]. Four inch wafers of silicon on sapphire are obtained from Union Carbide. They deposit a thin 0.5 $\mu$m epitaxial layer of silicon (100) on a 0.5 mm thick wafer of sapphire. Sapphire has excellent dielectric properties with exceptionally low absorption up to a THz [2.8].

As shown in Fig. 2.1(b), the metallic lines are grown on top of boxes of silicon. Thus the first step will be to etch the silicon, after which the metallic lines are added. The silicon is etched everywhere, except for small 50 $\mu$m square pads which bridge the leads of the antenna. By etching the silicon, we eliminate any dark currents which might flow across the transmission lines which feed the antenna. To etch the silicon we use standard optical photolithography techniques. First we spin on a thin ($\approx$.7 $\mu$m) layer of photoresist on the wafer. The wafer then undergoes a soft bake for two minutes on the 70°C hot plate. Then we use an optical mask and expose the photoresist with UV light for ten seconds. The wafer is exposed everywhere except above the places where we want the silicon to remain. The wafer is then placed in solution of 50% Kodak developer and 50% deionized (DI) water for sixty seconds. After this time the wafer is immediately placed in a second bath of pure DI water to quench the developer. This process removes the

exposed photoresist leaving behind 50 μm square boxes. The wafer is then placed in a 120°C oven for a 20 minute hard bake. Now the wafer is placed in a standard silicon wet etch which removes everything except the 50 μm square boxes which were protected by photoresist. The photoresist is then washed off with acetone.

The next step is to lay down the aluminum antenna and the transmission line using standard lift off techniques. The orientation of the dipole antenna relative to the sapphire substrate is important. Sapphire is a birefringent material and typically the wafers obtained from manufactures are R-cut. R-cut is defined such that the C-axis of the crystal is at an angle of 56 degrees from the plane of the wafer. We orient the dipole antenna so that it is perpendicular to the C-axis. This ensures that the antenna mostly excites the ordinary ray in the sapphire.

Once the proper orientation is found, the surface of the wafer must be thoroughly cleaned with TCA and baked in a 90°C oven for 20 minutes to drive off any water. Once again photoresist is spun onto the wafer, after which the wafer is immersed in cholorobenzene (highly toxic) for 10 minutes. The wafer then is soft baked for two minutes on the 70°C hot plate. Next the wafer is again exposed to UV light, but this time with a negative mask for the antennas. The wafer is then soaked in developer which removes the photoresist from the area you want the metal to stick. This time since the wafer was soaked in cholorobenzene, a ledge is formed in the photoresist as shown in Figure 2(a).

The next step is to deposit the metallic aluminum lines. We use an electron beam (E-Beam) evaporator to deposit the aluminum. Before the wafer is placed in the E-Beam evaporator, it is soaked for five seconds in a weak solution of 10% hydrofluoric acid. This removes any dirt or oxide layer on the silicon. Next the wafer is placed in an E-Beam evaporator. We evaporate two thin aluminum layers of 0.3 μm each to give a total of 0.6 μm. A ten minute cooling period between the two depositions ensures that the photoresist does not get too hot which would lead to poor lift off. After deposition, the

edge profile of the wafer should look like that in Figure 2.2(b). This figure illustrates the importance of the ledge. The aluminum cannot coat the walls of the photoresist. This allows for easy separation between the metal line and the metal on top of the photoresist in the subsequent liftoff process. Liftoff is achieved by soaking the wafer in acetone. The photoresist along with the metal on top comes off leaving behind a metal line as shown in Figure 2.2(c). It is clear from Fig 2.2(b) that too thick a layer of aluminum would impede the lift off process.

The silicon on the wafer now needs to be damaged with high energy ion implantation to reduce the free carrier lifetime in silicon. Undamaged silicon due to its indirect bandgap has a radiative lifetime ranging from 10's of milliseconds to nanoseconds [2.9]. Ion implantation introduces defects in the silicon which act as traps and recombination centers. Typically a dosage of 100 KeV $O^+$ ions at an areal density of $10^{15}$ cm$^{-2}$ will result in a carrier lifetime of 0.6 ps [2.10]. We use two doses, one at 100 KeV, $10^{15}$ cm$^{-2}$ and another at 200 KeV, $10^{15}$ cm$^{-2}$. During damage, the wafer is cooled by a water cooled plate so that the defects are not annealed by heating from the intense ion beam. Two doses ensure that the damage is uniform throughout the depth of silicon. This is of critical importance since we want all the carriers in the silicon to recombine at the same rate. If there are regions of low damage, then some carriers will recombine with a long carrier lifetime leading to a long tail in the turn off of the switch. After the implantation step, the individual antennas are diced from the wafer with a diamond saw into small chips, 5 mm x 10 mm.

It is important to note that we damage the switch after the wafer is metalized as opposed to before. From a processing perspective, it might appear more convenient to damage the wafer before metalization. We did try this approach, but those antennas produced a signal ten times smaller than those made with the damage after metalization process. One possible reason for this is that a large Schottky barrier forms between the metal and the silicon when the wafer is damaged first. Thus most of the voltage drop

across the switch will appear across the metal semiconductor contact and not across the silicon. It is the field which appears in the silicon that accelerates the free carriers and leads to the observed current transient. In the case where we damaged after, though, we typically find an ohmic contact between the aluminum and the silicon. This leads to a more uniform electric field distribution across the switch.

We have also tried to use ion-implanted GaAs switches but they were fraught with a number of problems. The GaAs wafer is 0.5 mm thick so it serves as both a substrate and a switching layer. The wafer is damaged with ion implantation, but only a thin 0.5 μm layer on top is damaged. This layer can have a fast picosecond carrier lifetime. Unfortunately, the optical radiation can penetrate below the damaged layer and excite free carriers which have carrier lifetimes exceeding a nanosecond. This leads to a long tail in the turn off of the switch. This problem is not encountered in the SOS switches since the entire 0.5 μm thick epi layer of silicon has been uniformly damaged. The other problem with damaged GaAs is that the transmission lines are placed directly on the GaAs substrate which is conductive (semiconductor) as opposed to sapphire which is an insulator. This means that current can flow between transmission lines on GaAs without passing through the switch. This results in large dark currents which limit the maximum voltage that can be placed across the lines. We found that the damaged GaAs switches tended to blow out at a relatively small voltages of 30 V across a 5 μm gap antenna while the SOS switches could hold off 120 V across the same gap.

## 2.3 Theory of Source Operation:

The operation of the Auston switch is relatively straight forward. Figure 2.3 shows a schematic of the silicon switch. First a short 100 fs optical pulse is focused with a 10X or 5X objective onto the silicon switch. This injects free carriers into the silicon switch. The pulses are generated by a Lexel 480 self modelocked Ti-Sapphire laser [2.11], centered at 780 nm with a 100 MHz repetition rate and an average power of

500 mW. The beam is split and attenuated so that the average power on a single switch is 150 mW. Since the optical pulse is short compared to the lifetime, T, of carriers in silicon we can treat the optical pulse as a delta function. The number of carriers generated initially is then given by,

$$n_0 = \frac{U}{\hbar\omega}(1-R)[1-\exp(-\alpha w)] \qquad \{2.1\}$$

Here $U$ is the energy in the incident pulse, $\hbar\omega$ is energy of the incident photon, $R$ is the reflectivity of silicon, and $\alpha$ is the optical absorption coefficient. The first term in the product corresponds to the number of photons in the incident pulse, the term in parenthesis corresponds to the fraction of photons coupled into the silicon, while the term in brackets gives the fraction of absorbed photons. This initial burst of carriers will lead to a current,

$$I_0 = e(\mu_e + \mu_p)\frac{V_A}{G^2} \bullet \frac{U}{\hbar\omega}(1-R)[1-\exp(-\alpha w)]. \qquad \{2.2\}$$

Here $\mu_e$ and $\mu_p$ are the electron and hole mobilities respectively, $V_A$ is the voltage placed across the silicon, and G is the length of the gap. This initial current will decay exponentially with a time constant T which for damaged silicon is 0.6 ps [2.10]. It is important to note that the current is linearly proportional to the applied voltage, $V_A$, and the incident pulse energy or laser power. Both these parameters can easily be adjusted during an experiment.

Expression {2.2} shows explicitly that we obtain the maximum photoresponse when the full voltage applied to the switch appears across the silicon. As mentioned previously, if instead of ohmic contacts between the aluminum and silicon there were Schottky barriers, then most of the voltage would be dropped across the Schottky barriers and very little would be dropped across the silicon. This would lead to a greatly reduced current pulse. As a curious side note, there does exist another type of switch based on

undamaged GaAs in which it is believed that the main mechanism for current pulse generation is due to carriers injected into the Schottky barrier region [2.12].

This initial current in {2.2} will decay exponentially with a time constant T which for damaged silicon is 0.6 ps. This time varying current will drive the dipole antenna. It is a difficult numerical problem to compute exactly the shape of the voltage transient emitted by the dipole antenna in response to the current pulse. In order to obtain a physical understanding of what the emitted pulse should look like, let us consider the case of the short dipole antenna. By short, we mean that the length of the dipole antenna is so short that its corresponding resonant frequency is well above the frequency components in the excitation current pulse. This is just the case of the elementary Hertzian dipole [2.13] in which the emitted spherical wave is given by,

$$E(r,t) = \frac{A\mu_0}{4\pi} \frac{\partial I(t)}{\partial t} \frac{e^{-jkr}}{r}, \qquad \{2.3\}$$

where I(t) is applied current transient, A is the length of the antenna, k is the wavevector, r is the distance to the observation point, and $\mu_0$ is the permeability of free space. For an excitation current I(t) which turns on quickly and decays exponentially with the electronic carrier lifetime, we would expect to see a bipolar emitted pulse. The bipolar pulse will be asymmetric with a sharp peak on the initial lobe followed by a more slowly varying negative lobe. The net area under the time profile of E(t) should be identically zero since it is impossible to radiate a *dc* electric field into the far field. This is seen explicitly in {2.3} since the time derivative of I(t) has no *dc* component. We typically see approximately single cycle behavior in our electric field pulses.

The Hertzian dipole approximation applies to our short 30 μm long dipole antennas. For all the experiments, though, discussed in this thesis we use 300 μm long dipole antennas which cannot be considered short. First let us estimate the resonant frequency, $f_o = c/2An_{eff}$, of this dipole antenna where $n_{eff}$ is effective index of refraction. Since the antenna appears at the interface between air and sapphire, a good approximation

for $n_{eff}$ is the square root of the average dielectric constant of air and sapphire [2.14]. For the frequency range of interest the dielectric constant of the ordinary ray in sapphire is 9.4 [2.8] corresponding to an $f_0 \approx 220$ GHz. This is in rough agreement with our experimentally determined value of 180 GHz.

The driving pulse actually has comparable frequency components above and below this center frequency. This can bee seen by looking at the magnitude of the Fourier transform of the driving pulse, $|I(\omega)| = [T^{-2}+(2\pi f)^2]^{-1/2}$. The driving pulse has equal strength Fourier components extending from *dc* up to the 3 dB corner frequency of 265 GHz which is above our resonant frequency. In addition, this expression for $|I(\omega)|$ also explains why we find experimentally that the low frequency 300 $\mu$m dipole antennas are more powerful then the 30 $\mu$m dipoles. 30 $\mu$m dipoles have a resonant frequency at 2.2 THz. At this high frequency there is very little current to drive the antenna. In fact, I(2.2 THz) is over six times smaller than I(220 GHz).

From this discussion it should be clear that the size of signal should decrease as the resonant frequency is pushed to higher frequency. However, the situation is reversed as we push to lower frequencies. From the expression for the Fourier transform of our driving pulse, there is no low frequency limit to the available frequency components. Thus there is no real low frequency limit to our antenna sources. The only limitations come from diffraction effects. As the frequency is lowered, the size of the optics must be increased beyond practical limits. The lowest frequency system obtained in our lab with 3.5 inch collimating optics had a center frequency at 50 GHz.

To actually compute the shape of the emitted pulse requires rather involved numerical calculations. Our needs are fairly modest, so making such exact calculations is not justified. We only need to know the approximate center frequency and the width of the emitted pulse. The above analysis allows us to estimate the center frequency of the emitted pulse. Finding the pulse width is more difficult. Experimentally we find a pulse width corresponding to only one oscillation at the center frequency. Apparently a dipole

antenna is a very broadband radiator. It has a center frequency on the same order as its bandwidth. This surprising result can be understood by looking at numerical calculations [2.15] of the frequency dependent complex impedance of a dipole antenna. These calculations show that the impedance of a dipole is not sharply peaked at the resonant frequency as one might guess. Instead the impedance varies relatively slowly about the center frequency. The real part of the impedance resembles a Loretzian function with the width of the central peak roughly equal to the center frequency. The slowly varying impedance means that we can couple radiation out of the antenna over a broad frequency range. This broadband response results in the observed single cycle radiated pulse.

Since the antenna appears at the interface between sapphire and air, it is important to know in which direction most of the radiation is emitted. It turns out that much more power is radiated into the dielectric than into the air. The power is divided according to the ratio of $n^3$:1 [2.17]. This can be understood by a simple argument given by Rutledge *et al.* [2.17]. It is easier to consider the dipole antenna as a receiver and then use reciprocity to evaluate its performance as a transmitter. The dipole antenna responds to the local electric field at the dielectric air interface. First consider a wave incident from air into the dielectric. The air has a large impedance while the dielectric has a low impedance, thus the transmitted field into the dielectric is smaller than the incident field and the dipole response is low [2.13]. In the reversed situation, when the wave is incident from the dielectric side, the transmitted field is larger than the incident field and the dipole response is large. By reciprocity, the antenna transmits better into the dielectric than into the air.

As shown in Figure 2.4(a), the radiation into the substrate will eventually reflect off the bottom of the substrate and reduce the coupling into free space. In order to maximize the amount of radiation coupled into free space, we use a hyperhemispherical silicon lens [2.18]. The principle behind the operation of this lens is identical to the oil immersion microscope objective. It turns out that for a spherical surface there are two

conjugate axial points which are free from spherical aberrations, a discovery attributed to Huygens. Figure 2.4(b) is a ray diagram picture showing the focusing properties of a hyperhemisphere of radius R and index n. In the limit of ray optics, if an antenna is placed exactly at a distance R/n from the center of the sphere then all rays emitted in the forward direction appear to come form a single conjugate point a distance nR from the center. This result may be proved easily with Snell's law and elementary geometry. Even rays which are emitted perpendicular to the optic axis will appear to come from the same conjugate point. Thus the lens has a full collection solid angle of $2\pi$ steradians. With a silicon lens, n=3.4, this solid angle is focused down to 0.027 steradians. Thus an optic with an f/#=1.6 or better will be able to collect the entire beam. In our experiments we use a 90 degree parabolic mirror with an f/#=1.3 and focal length of 3.5" to collimate the entire beam. This choice of optics leads to a highly efficient system.

Although the ray diagram picture defines the optimal position for the antenna, it does not tell us how large the radius of the silicon lens should be. In order to understand this design constraint requires taking into account diffraction of the beam by the lens. According to Kasilingam and Rutledge [2.18] the radius should be larger than the free space wavelength to avoid diffraction effects. We chose a radius of 5 mm since the lowest frequency of interest is 50 GHz which has a free space wavelength of 6 mm.

Our choice of a silicon lens over a sapphire lens may appear puzzling at first. Actually for our first experiments, we did use a sapphire lens. Obviously with the sapphire lens we can index match to the sapphire antenna chip eliminating reflections from the chip lens interface. However, as we refined our experimental technique, we opted for a silicon lens since it has superior dielectric properties compared to sapphire above 250 GHz. The silicon is a special grade of Float Zone silicon [2.19]with a resistivity greater than 10,000 Ω-cm. The index of refraction of silicon from 250 GHz to 2 THz is flat to 1 part in a 1000 [2.8]. This means that the lens will be free of chromatic aberrations as well as spherical aberrations. In addition the power absorption coefficient

of silicon is less than 0.05 $cm^{-1}$ in this same range. In contrast sapphire has a large resonance in the THz regime. The power absorption coefficient is 3 $cm^{-1}$ at 1.5 THz [2.8].

## 2.4 Source Detection

Thus far we have only treated the source but we have not explained how to detect these pulses. No conventional detection electronics are available with the necessary bandwidth to time resolve the pulses. In order to time resolve the pulses, we use the Terahertz Time Domain Spectroscopy (THz-TDS) technique. Figure 2.5 shows a typical THz-TDS setup for antenna characterization with a second antenna/lens system identical to the transmitter. The pulse is generated from the transmitter by the method described above. This produces a THz electric field pulse. The pulse is initially focused by the silicon lens and then it is fully collimated by the parabolic mirror. The collimated beam propagates through free space and then is refocused onto the receiver. The fabrication of the receiver is in all respects identical to the transmitter. The only difference is that we replace the dc battery bias to the antenna terminals (see Fig. 2.1(a)) with a high quality low noise current amplifier. On the receiver the "*dc*" bias will come from the THz electric field pulse which polarizes the switch. A second optical pulse is incident on the receiver. At the instant when the optical pulse shorts the receiver, a small amount of photocurrent will flow through leads of the antenna in response to the THz field bias. This current will continue to flow until the free carriers recombine and the switch closes. This photocurrent can be easily measured by the current amplifier. The shape of the electric field pulse can then be read out by measuring the photocurrent as a function of time delay, $\tau$, between the two optical pulses. It is important to recognize that this technique allows us to measure the electric field that is incident on the antenna and not just the average power.

Quantitatively, the photocurrent we measure is the cross correlation between the field across the switch of the receiving antenna, $E_r$, and the sampling function, f(t),

$$I_{pc}(\tau) = B\int_{-\infty}^{\infty} E_r(t) f(t+\tau) dt \;. \qquad \{2.4\}$$

Here B is a constant that depends on the laser power and the detailed properties of the switch. f(t) is simply the normalized time profile of the free carrier density in receiver switch. $E_r$ is the field across the switch, not the actual field, $E_{fs}$, that is propagating through free space. $E_{fs}$ will be modified by the responsivity of the dipole receiver. If we assume for simplicity that we are in the Hertzian dipole limit, then from equation {2.3} we would expect $E_r$ to be the first derivative of $E_{fs}$. If we further assume that our sampling function is a delta function, then $I_{pc}(\tau)$ should look like the derivative of a bipolar pulse. This is indeed what we find experimentally.

## 2.5 Experimental Source Characterization

Let us now look at the performance of one of our 300 μm dipole antennas. Figure 2.6(a) shows the measured time profile of the pulse and Figure 2.6(b) is the magnitude of the Fourier Transform of time profile in Fig. 2.6(a). To zero order, the measured pulse looks like the first derivative of a bipolar pulse as expected. Thus the actual pulse in free space must approximately be a single cycle sine wave with a period of 5.6 ps. This corresponds to a center frequency of 180 GHz which is near the design frequency of 220 GHz. The pull to lower frequencies is most likely due to the limited bandwidth in the optically injected current pulse. Recall from Section 2.3 that the 3 dB bandwidth of the current pulse is 265 GHz. By looking at Fig. 2.6(b) we see that the pulse is extremely broadband, with a FWHM of 150 GHz which is almost equal to the center frequency. A more careful look at Fig. 2.6(a) reveals a few small periodic oscillations after the main pulse. These are possibly due errors in the alignment of the spectrometer.

In addition to the broadband bandwidth, the second obvious characteristic of the pulse is that it is virtually noise free. This trace was taken in four minutes with 150 mW of laser power focused on each antenna chip. We use lock-in techniques to improve the signal to noise. The transmitter is biased with a 2 KHz, 50 V sine wave. We detect the synchronous photocurrent in the receiver with an Ithaco 564 current amplifier coupled to a standard PAR 124A lock-in. By *ac* chopping the bias on the transmitter, we obtain twice the signal at the lock-in as compared to chopping the intensity of the laser with a mechanical chopper.

The maximum signal on peak is 250 nA with a noise level of one part per thousand in a 1 Hz bandwidth at a frequency of 1 KHz. This noise level is less than the 1% fluctuations on the laser. The reduction in noise is probably due to saturation of the number of photoexcited carriers in the transmitter. The noise floor off peak before the main pulse is 10 pA/$\sqrt{Hz}$. This gives us an enormous dynamic range of $2.5\text{x}10^4$ in electric field or $6.25\text{x}10^8$ in power.

We have calibrated our system in order to approximate the average power in the free space pulse. To do this we first measure the amount of current flowing through a switch in response to an applied *dc* bias. In our case we obtain 10 μA for an applied bias of 10 V. As can be seen in Fig. 2.6(a), the maximum photocurrent is 250 nA. This implies that we have an effective bias on the receiver switch of 250 mV. The average power on the receiver then is just 1.5 μW where we have assumed that the dipole antenna has an impedance of 40 Ω (see Section 6.3.2). In addition, we have included a duty factor of 1000 since the THz pulse has a temporal width of roughly 10 ps and the pulses are repeated once every 10 ns. To compute the transmitted power into the silicon lens, we use the fact that for an applied bias of 50 V, the peak current in the transmitter is 50 mA. This corresponds to an average emitted power of 100 μW. If we assume that the losses in going from the transmitter into free space are the same as the losses in going from free space into the receiver, then the average power in free space beam is 12 μW.

These sources are extremely bright. The other common broadband source in this regime is an hot mercury lamp. At first it is not obvious how to make a fair comparison between the antenna source and the black body source. We know that the total power, $P(\lambda)$, emitted from a small hole of area, $\sigma$, from an oven at temperature $T_S$ into a frequency interval $\delta f$ is,

$$P(\lambda) = \frac{2\pi}{\lambda^2} \bullet k_B T_s \bullet \sigma \bullet \delta f. \tag{2.5}$$

Since an antenna on resonance has length $\lambda/2$, we replace $\sigma$ by $(\lambda/2)^2$. In this case the power density, $P(\lambda)/\delta f$, is just $(\pi/2) * k_B T_S$. The antenna sources have an average power density of 320 eV. This corresponds to an effective source temperature of 3.5 million degrees Kelvin! This is many times hotter that the average mercury lamp source temperature of 2000 K.

The large dynamic range of our system means that we have a very sensitive detector. The minimum detectable power is only 20 $fW/\sqrt{Hz}$. Compare this to the 140 $fW/\sqrt{Hz}$ noise floor of a 4.2 Kelvin Silicon Bolometer. It is literally amazing that a room temperature detector can have a noise floor comparable to a helium cooled bolometer. This result can be understood intuitively. The noise floor of the antenna system is so low because we are effectively using a form of gated boxcar detection. We only sample the electric field pulse when the optical pulse is at the switch. During this time we also sample the shot noise in the photocurrent. At other times the receiver switch is unbiased so there is no current and therefore no shot noise to collect.

In summary, the important facts to remember is that these antenna sources are both broadband and bright and they can also be used as very sensitive gated detectors.

| | |
|---|---|
| Length | = 300 μm |
| Center Frequency | =180 GHz |
| FWHM Bandwidth | = 150 GHz |
| Peak Power | = 12 mW |
| Average Power | = 12 μW |
| Min. Detec. Power | = 20 fW/$\sqrt{Hz}$ |

## 2.6 Device Characterization: Terahertz Time Domain Interferometry

### 2.6.1 Device Admittance

Up to this point, we have discussed in detail the picosecond source, but we have not explained how this source can be used to characterize a two terminal device. What we mean by device characterization is that we would like to measure the linear response properties of the device. For devices, the usual linear response function is the admittance, $Y(\omega)$. The admittance relates the input voltage, $V_{\omega}$, to the generated current, $I_{\omega}$,

$$I_{\omega} = Y(\omega)V_{\omega} \quad . \qquad \{2.6\}$$

The most straight forward procedure for measuring the admittance would be to inject a sinusoidal voltage signal at frequency ω into the device and measure the amplitude and phase of the resulting current. Then by tuning the frequency, $Y(\omega)$ could be mapped over a broad frequency scale. This procedure is indeed used and works extremely well for standard devices that operate at room temperature and relatively low frequencies (<20 GHz) where tunable sources and broadband coaxial cable are readily available.

The types of devices, though, that we are interested in studying are exotic and require much more stringent temperature and frequency constraints. For example a Quantum Point Contact (QPC) tunnel barrier operates at temperatures below 0.5 K which means the device must be bathed in superfluid $^3$He. In addition we are interested in learning how the linear response varies with high magnetic field so it must reside inside a superconducting magnet cryostat. Finally the frequency scale that we are interested in probing has as lower bound of 50 GHz and an upper bound in the THz regime. This frequency scale introduces a whole host of problems. The first problem is that at this frequency scale there is no broadband coaxial cable that can easily carry the radiation down into a 0.5 K sample chamber and the carry the output signal back out of the cryostat. In addition, experiments with coaxial cables at high frequencies are plagued by unwanted reflections and large standing waves. Another option is to use hollow rectangular waveguide. The problem is that waveguides are not sufficiently broadband for our needs. The second and equally serious problem is that there is no broadband tunable source or ultrafast detector in our frequency range of interest.

To overcome these obstacles we developed a new technique based on quasioptical methods and interferometry. The quasioptical method will allow us to overcome the bandwidth limitations of waveguides and the interferometric method will allows us to both inject high frequencies and detect the high frequency response.

### 2.6.2 Quasioptical Coupling

The quasioptical scheme was already described above in Section 2.5 where it was used to characterize the terahertz pulse. Looking once again at Fig. 2.5, the idea is to replace the Auston receiver with the device under test. The device will also be placed at the feed of an antenna to maximize the coupling of radiation into the device. The main difference is that the device now resides in the core region of a cryostat. The other difference is that there will be no laser pulse to gate the device and time resolve the

output pulse. As we shall discuss later, the gating action of the laser pulse will be replaced by a second terahertz pulse.

The quasioptical method is extremely broadband. Since the pulses are propagating through free space there is no dispersion or attenuation of the pulses as there is in coaxial cables or waveguides. There is no practical high frequency limit to this method as is suggested by the name quasioptical. In fact these methods are common in the far infrared and optical regime. On the low frequency end we are limited by diffraction effects. The ultimate limit is set by the smallest aperture in the system. In our system the smallest aperture is set by the innermost cryostat window which is adjacent to the sample. We know that for a gaussian beam, the minimum spot size of a focusing system is given by $1.27\lambda * f/\#$. For a window size of 2 cm and an $f/\#=1$, the minimum frequency is 12 GHz which is well below our frequency range of interest. To go below this frequency range it is more natural to switch back to using conventional electronics and coaxial waveguides to measure the admittance.

To maximize the coupling of the pulses to the device, we place the device at the terminals of antenna. Figure 2.7 shows a schematic of the coupling scheme. The antenna is used to overcome the basic limits of diffraction. It turns out that dimensions of most devices are much smaller than the wavelength of the incident radiation. For example, the active area of a QPC is a square region 0.3 μm on a side which is much smaller than our typical wavelength of 3000 μm. The idea is to only focus the electric field down to the antenna which has a length of $\lambda/2$. The antenna then focuses the electric field to the sample which only has a size w.

To fully appreciate the importance of the antenna let us compute the voltage produced across two different antennas of length $\lambda/2$ and w in the presence of incident radiation of wavelength $\lambda$. The voltage developed across an antenna, $V_A$, is given by hE, where h is the effective height of the antenna and E is the incident electric field [2.20]. For a resonant dipole antenna with length $\lambda/2$, $h=0.64\lambda/2$. For the shorter antenna of

length w the effective height is reduced to 0.5w. Thus the voltage developed across the longer antenna is 0.64λ/w times larger than that developed across the smaller antenna. For the QPC example given above, this corresponds to an enhancement by a factor of 6400! It is clear from this example than an antenna is a necessary element whenever the device under study becomes smaller than the wavelength of the incident radiation.

### 2.6.3 Diode Rectification

The quasioptical method allows us to deliver picosecond pulses to the device of interest. The next problem is to devise a method to measure the high frequency response. Since it is impossible to measure the response directly at these high frequencies, we have chosen a different approach. Instead of measuring the high frequency response directly, we measure the change in the *dc* current , $\Delta I_{dc}$, that is induced in the device in the presence of a microwave field. In contrast to the high frequency response, $\Delta I_{dc}$ can easily be measured with standard low frequency (KHz) electronics. In addition, lock-in techniques may be used to dramatically improve the signal to noise ratio. As we will describe in detail below, the magnitude of $\Delta I_{dc}$ will depend on the frequency dependent admittance of the device. Thus a measure of $\Delta I_{dc}(\omega)$ will give an indirect measure of $Y(\omega)$.

The technique that we have developed is absolutely general and can be applied to any device which exhibits a nonlinear *dc* I-V curve. The most common type of device that exhibits nonlinear I-V characteristics is the crystal diode rectifier. In the presence of a voltage, $V=V_0+V_\omega\cos(\omega t)$, across the diode a finite rectified current, $\Delta I_{dc}$, will be generated. To lowest order in $V_\omega$, $\Delta I_{dc}$ is,

$$\Delta I_{dc}(\omega)=\frac{1}{4}\frac{\partial^2 I}{\partial V^2}\bigg|_{V_0}|V_\omega|^2. \qquad \{2.7\}$$

Notice that $\Delta I_{dc}$ is proportional to the second derivative of the *dc* I-V curve evaluated at the *dc* operating point, $I(V_0)$. This expression shows explicitly that the *dc* I-V curve must be nonlinear in order to produce a rectified current. The appearance of the second derivative is quite general. As we shall show in Chapter 3, an SIS tunnel junction can also act as a rectifier. The rectified current in an SIS tunnel junction is proportional to the discrete finite difference second derivative of the *dc* I-V curve. Another important point to notice is that $\Delta I_{dc}$ is proportional to $V_\omega^2$ which means that $\Delta I_{dc}$ is proportional to the power absorbed in the diode. Such devices are often called square law detectors. As we shall show later, the dependence of $\Delta I_{dc}$ on $V_\omega^2$ means that we can use interferometric techniques to measure $\Delta I_{dc}$ .

In order to see explicitly how $\Delta I_{dc}$ depends on $Y(\omega)$ we need to appeal to the circuit model given in Figure 2.8. We have modeled the antenna with its Norton equivalent circuit [2.20]. This consists of an ideal current source, $I_A(\omega)$, and a frequency dependent antenna admittance $Y_A(\omega)$. $I_A(\omega)$ is easily found by taking the product of the antenna voltage, $V_A(\omega)$, described above with the antenna admittance. As usual $Y(\omega)$ represents the admittance of the device. It is important to recognize that $V_\omega$ in {2.7} above is the voltage that appears across the device. This voltage is not directly under experimental control. We can use elementary circuit theory to express $V_\omega$ in equation {2.7} in terms of $Y_A(\omega)$, $I_A(\omega)$, and $Y(\omega)$. The antenna admittance is a property intrinsic to the antenna and can be calculated numerically and in some cases analytically [2.20]. $I_A(\omega)$, unlike $V_\omega$ , is proportional to the incident microwave field which is directly under experimental control. $Y(\omega)$ is of course the quantity we would like to measure. The resulting expression for $\Delta I_{dc}$ is,

$$\Delta I_{dc}(\omega) = \frac{1}{4}\frac{\partial^2 I}{\partial V^2}\bigg|_{V_0} \bullet \frac{I_A^*(\omega) I_A(\omega)}{\left|Y_A(\omega)+Y(\omega)\right|^2}. \qquad \{2.8\}$$

By varying $I_A(\omega)$over a broad frequency scale, $\Delta I_{dc}(\omega)$ can be measured. If the second derivative of the *dc* I-V curve, $Y_A(\omega)$, and $I_A(\omega)$ are all known then $Y(\omega)$ can be extracted.

**2.6.4 Terahertz Interferometry**

Expression {2.8} above gives an explicit method for extracting $Y(\omega)$ from measurements of $\Delta I_{dc}(\omega)$ using a tunable broadband source. Unfortunately, as we have described previously, such sources do not exist and we need to use an interferometric technique based on broadband pulses and a homemade Fourier transform spectrometer depicted in Figure 2.9.

The operation of this spectrometer is straight forward. To begin with let us only consider the arm of the interferometer which passes *through* the terahertz beamsplitter (beam #1). A 100 fs laser pulse is incident on the photoconductive switch which is coupled to an antenna which generates a THz pulse as shown in Fig. 2.6(a). This pulse is then collimated by a parabolic mirror into a large 3.5 inch beam. This beam then passes through a beam splitter. A final parabola is used to focus the beam down onto the sample which resides in the cryostat. Due to the rectification action of the device, a *dc* current is generated in the device, $\Delta I_{dc}$, as in equation {2.8} above. In this case since our pulse contains many different Fourier components, the amount of current generated is given by,

$$\Delta I_{dc} = \int_0^\infty A(\omega) I_1(\omega) I_1^*(\omega) d\omega \quad . \qquad \{2.9\}$$

We must integrate over all the Fourier components to get the full *dc* response. Here $I_1(\omega)$ is the Fourier transform of the current pulse generated by beam #1 and $A(\omega)$ contains the nonlinear mixing coefficient and linear response factors given in equation {2.8}. It is important to extend the above definition to negative frequencies so that we can use standard Fourier transform techniques. It can easily be shown that $A(\omega)=A(-\omega)$ by using

the fact that $Y(\omega)=Y^*(-\omega)$ and $Y_A(\omega)=Y_A^*(-\omega)$. The latter two statements are true for both the device and the antenna since they both are linear time invariant (LTI) causal systems. In addition $I_1(\omega)=I_1^*(-\omega)$ since $I_1(t)$ is real. From these results we obtain,

$$\Delta I_{dc} = \frac{1}{2}\int_{-\infty}^{\infty} A(\omega) I_1(\omega) I_1^*(\omega) d\omega \ . \qquad \{2.10\}$$

Our goal, though , is to measure $A(\omega)$. In order to do this, we must use a second terahertz pulse from the second antenna. This first pulse can be time delayed with a variable time delay, $\tau$, with respect to the pulse from the second antenna. We accomplish this by taking the original optical beam from the laser and splitting it into two. One half of the laser beam is injected into the second photoconductive antenna. The other half of the laser beam first passes through a variable Klinger optical delay line and then is injected into the first photoconductive antenna. The two Terahertz beams are then combined into one with a Mylar (or wire grid )beam splitter. A description of these beam splitters will be given in Chapters 4 and 6. Both beams are then focused onto the sample. We then measure the induced *dc* current generated in the device as a function of time delay, $\tau$, between the two pulses and we obtain an interferogram as shown. By Fourier transforming this interferogram we obtain information about $A(\omega)$.

To see this explicitly, consider the following analysis. The expression for the induced current with two beams $I_1(t-\tau)$ and $I_2(t)$ incident on the device is,

$$\Delta I_{dc}(\tau) = \frac{1}{2}\int_{-\infty}^{\infty} A(\omega)\left[I_2(\omega) + I_1(\omega)e^{j\omega\tau}\right]\left[I_2^*(\omega) + I_1^*(\omega)e^{-j\omega\tau}\right]d\omega. \qquad \{2.11\}$$

There are three contributions to the induced current. The first two are uninteresting and are independent of time delay and will be neglected. They correspond simply to the induced current due to each individual beam when interference is neglected. It is the third interferometric term,

$$\Delta I_{dc}(\tau) = \frac{1}{2}\int_{-\infty}^{\infty} A(\omega)\left[I_1(\omega)I_2^*(\omega)e^{j\omega\tau} + I_1^*(\omega)I_2(\omega)e^{-j\omega\tau}\right]d\omega, \qquad \{2.12\}$$

which allows us to extract A(ω). In the laboratory we measure $\Delta I_{dc}(\tau)$ by varying the time delay, τ, of the second optical pulse. Next we Fourier transform $\Delta I_{dc}(\tau)$ to get $\Delta I_{dc}(\omega)$,

$$\begin{aligned}\Delta I_{dc}(\omega) &= F[\Delta I_{dc}(\tau)] \\ &= 2\pi A(\omega) I_1(\omega) I_2^*(\omega). \end{aligned} \qquad \{2.13\}$$

Thus, $\Delta I_{dc}(\omega)$ is directly proportional to the quantity of interest, A(ω). In a typical experiment, the data is normalized to some fixed reference to remove the contribution from the fixed frequency spectrum of $I_1$ and $I_2$. Once A(ω) is determined we can then return to equation {2.8} to extract Y(ω).

The above discussion has shown in general how interferometric techniques can be used in characterizing an arbitrary nonlinear device. Although in the previous discussion, we have assumed that our source consists of picosecond electrical pulses, the experiment in principle could also be accomplished with a hot lamp black body source and a standard Fourier transform infrared spectrometer [FTIR]. In fact Mears [2.21] has applied the FTIR method to probing SIS tunnel junctions. However, the signal to noise ratio in those experiments was not sufficiently high enough to obtain data over a broad frequency scale.

Our THz-TDI has a number of distinct advantages over a standard FTIR [2.1]. The first advantage is that our antenna source is much brighter than a typical lamp source as was discussed previously in Section 2.5. The other critical advantage is that half of our interferometer lies in the optical domain, while the other half is in the low frequency terahertz regime. This means that we can strategically place our delay line in the optical portion of the interferometer as opposed to the terahertz portion of the interferometer. The advantages of this approach are numerous. First since the optical beam is only a millimeter in diameter, the retroreflector in the delay line can be small and light. In an

FTIR the beam is typically four inches in diameter making the optics bulky and hard to move. On the other hand, the optical retroreflector is small so it can be placed on a rapidly moving arm which allows for the application of powerful signal averaging techniques which can significantly enhance the signal to noise ratio of our system. A second more subtle, but perhaps more important advantage of keeping the delay line in the optical regime is that we are not plagued by the alignment difficulties inherent to an FTIR. In a standard FTIR, the moving mirror needs to be aligned with interferometric accuracy with respect to the rest of the spectrometer. This alignment procedure is difficult and time consuming [2.22]. For our system the terahertz portion of the spectrometer which requires interferometric alignment has no moving parts which makes it trivial to align. The alignment of the delay line in the optical domain is also trivial since it does not require interferometric accuracy. Only one laser beam is incident on a photoconductive switch. It does not have to interfere with the second laser beam.

## 2.7 Summary

In this Chapter we have provided the basic information needed to design terahertz pulsed sources and described how these pulses can be used to characterize the dynamic response of an arbitrary nonlinear device. It should be clear now that the THz-TDI technique is extremely general and can be applied to any device which exhibits a nonlinearity in its I-V characteristics. We believe that this technique will find its niche in probing devices which operate in exotic environments such as ultralow millikelvin temperatures and high magnetic fields.

## 2.8 References

[2.1] P. R. Griffiths and J. A. deHaseth, Fourier Transform Infrared Spectrometry. New York: John Wiley & Sons, 1986.

[2.2] S. Gasiorowicz, Quantum Physics. New York: John Wiley & Sons, 1974.

[2.3] D.H.Auston, in Ultrashort Laser Pulses and Applications, eds W. Kaiser, Springer Verlag, 183 (1988).

[2.4] R. B. Hammond, N.G. Paulter, R.S. Wagner, W.R. Eisenstadt, *Appl. Phys. Lett.* **45**, 404 (1984).

[2.5] M. Y. Frankel, J. F. Whitaker, G. A. Mourou, F. W. Smith, and A. R. Calawa, *IEEE Trans. on Elect. Dev*. **37**, 2493 (1990).

[2.6] P.R. Smith, D. H. Auston, A.M. Johnson, W.M. Augustyniak, *Appl. Phys. Lett.* **38**, 47 (1981).

[2.7] M. B. Ketchen, D. Grischkowsky, T. C. Chen, C-C Chi, I. N. Duling III, N. J. Halas, J-M. Halbout, J. A. Kash, and G. P. Li, *Appl. Phys. Lett.* **48**, 751 (1986).

[2.8] D. Grischkowsky, S. Keiding, M. van Exter, and C. Fattinger, *J. Opt. Soc. Am. B* **7**, 2006 (1990).

[2.9] D.H. Auston, *Appl. Phys. Lett.* **26**, 101 (1975).

[2.10] F.E. Doany, D. Grishkowsky, C.C. Chi: Digest of the second Topical Conference on Picosecond Electronics and Optoelectronics, Optical Society of America, Washington, *dc* (1987).

[2.11] D. E. Spence, P. N. Kean, and W. Sibbett, *Optics Letters* **16**, 42 (1991).

[2.12] S. E. Ralph and D. Grischkowsky, *Appl. Phys. Lett.* **59**, 1972 (1991).

[2.13] S. Ramo, J. R. Whinnery, and T. VanDuzer, Fields and Waves in Communication Electronics, New York: John Wiley & Sons, 1984.

[2.14] D. B. Rutledge and M. S. Muha, *IEEE Trans. Antennas and Prop.* **AP-30**, 535 (1982).

[2.15] M. Kominami, D. M. Pozar, and D. H. Schaubert, *EEE Trans. Antennas and Prop.* **AP-33**, 600 (1985).

[2.16] W. Lukosz and R. E. Kunz, *J. Opt. Soc. Amer.* **67**, 1607 (1977).

[2.17] D. B. Rutledge and M. S. Muha, *IEEE Trans. Antennas and Prop.* **AP-30**, 535 (1982).

[2.18] D. Kasilingam and D. Rutledge, *Inter. J. of Infrared and Millimeter Waves 7*, 1631 (1986).

[2.19] Try Infrared Optical Products ,Farming Dale, New York, 516-694-6035.

[2.20] J. D. Kraus, Antennas 2nd ed., New York: McGraw Hill, 1988.

[2.21] C.A. Mears, Ph.D. Thesis, University of California at Berkeley, 1991.

[2.22] J. C. Mather, Ph.D. Thesis, University of California at Berkeley, 1974.

## 2.9 Figure Captions

Figure 2.1: (a) 100 fs incident optical pulse triggers the silicon photoconductive switch which then drives the antenna to radiate a 6 ps Terahertz pulse. (b) Typical dimensions for 300 μm dipole antenna source.

Figure 2.2: Photolithographic steps for metalization of antenna. (a) Wafer which has been coated with photoresist and developed (b) Evaporate thin aluminum layer (c) Dip wafer in acetone to remove photoresist leaving behind aluminum lines.

Figure 2.3: Auston Switch. A 100 fs incident pulse of energy U is incident on a damaged silicon patch of area wG. The pulse generates free carriers which closes the switch for approximately 0.6 ps.

Figure 2.4: (a) Radiation emitted from an antenna into a sapphire substrate is reflected by the sapphire air interface. (b) Application of a hyperhemispherical lens to fully couple the radiation out of the dipole antenna.

Figure 2.5: Quasioptical method for time resolving a Terahertz pulse.

Figure 2.6: (a) Typical time domain trace of pulse (b) Magnitude of the Fourier transform of the pulse in (a).

Figure 2.7: Method of quasioptical coupling to an antenna

Figure 2.8: Norton equivalent circuit for the antenna and the device.

Figure 2.9: Terahertz Time Domain Interferometer which is used to characterize the dynamic response of the nonlinear device. We measure the *dc* rectified current the flows through the device as a function of time delay, $\tau$, between the two optical pulses.

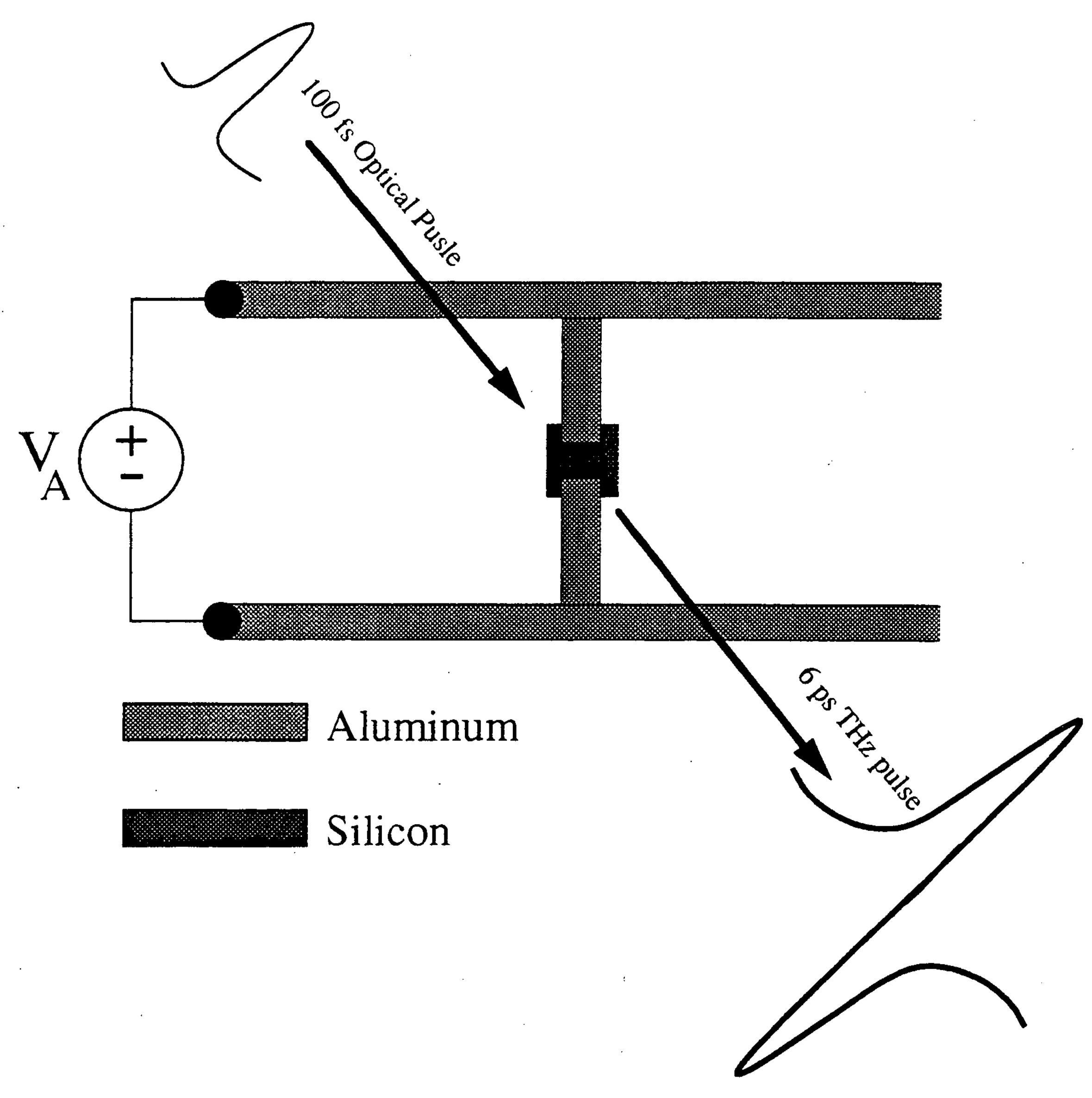


Figure 2.1a

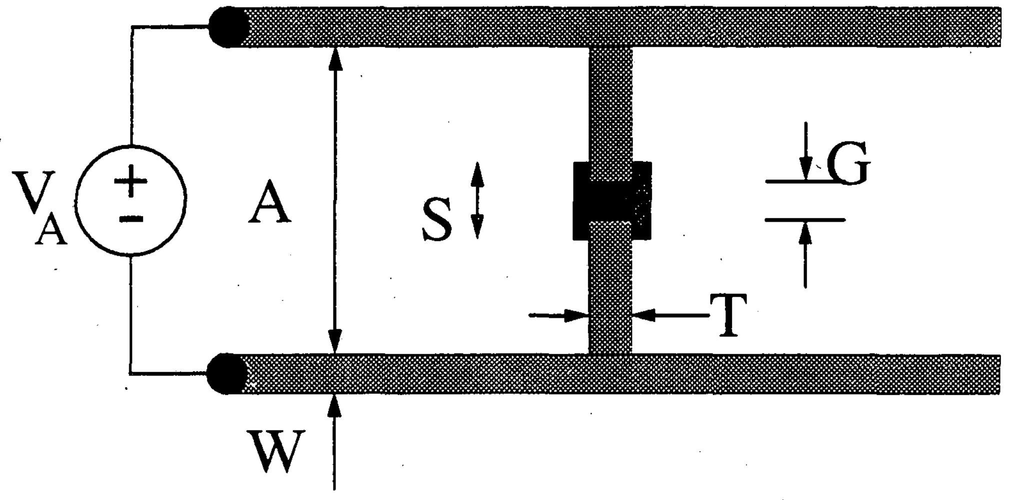


**Typical Dimensions**

$V_A = 50$ V
A = 300 μm
W = 25 μm
S = 50 μm
T = 20 μm
G = 5 μm

Aluminum

Silicon

Figure 2.1b

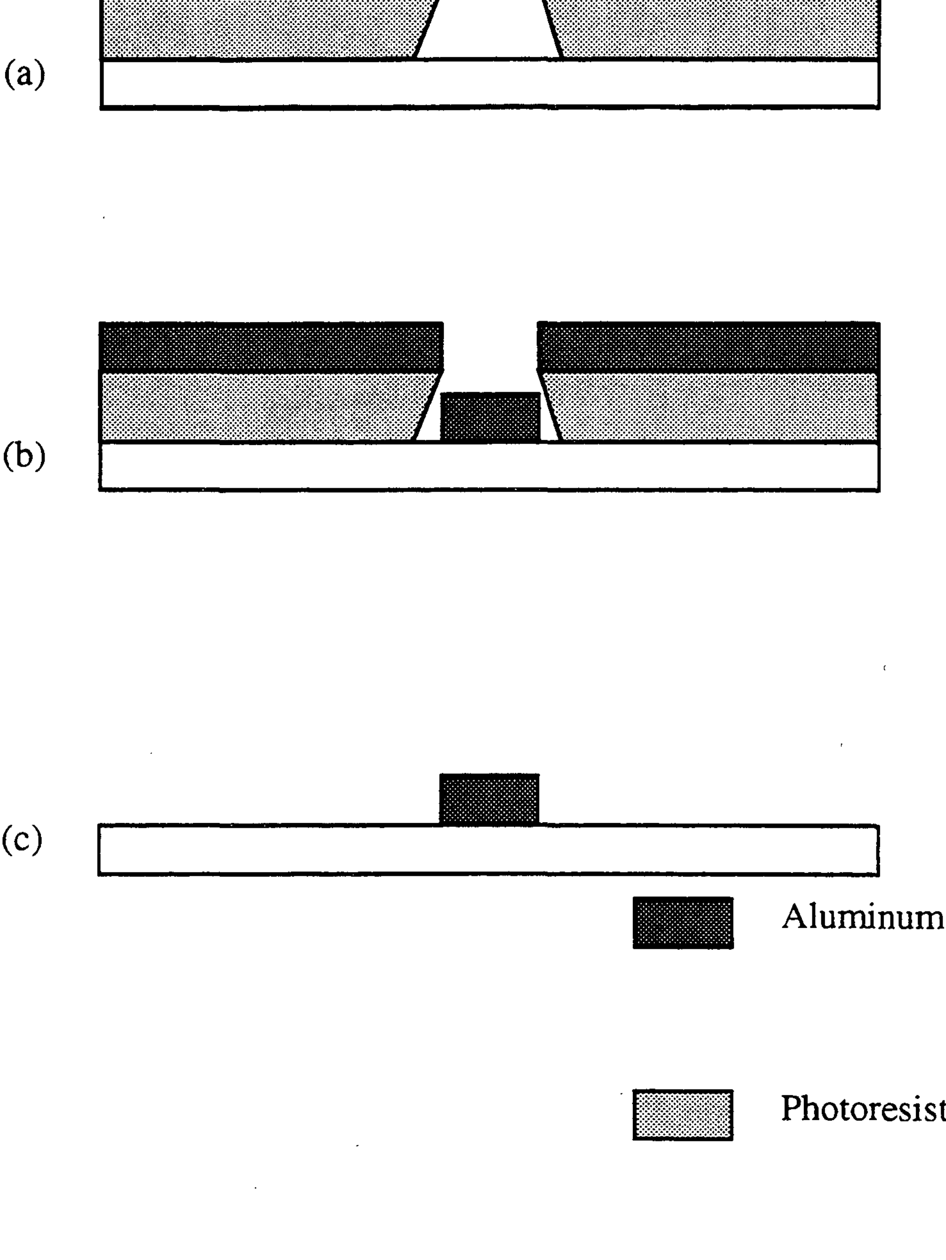


Figure 2.2

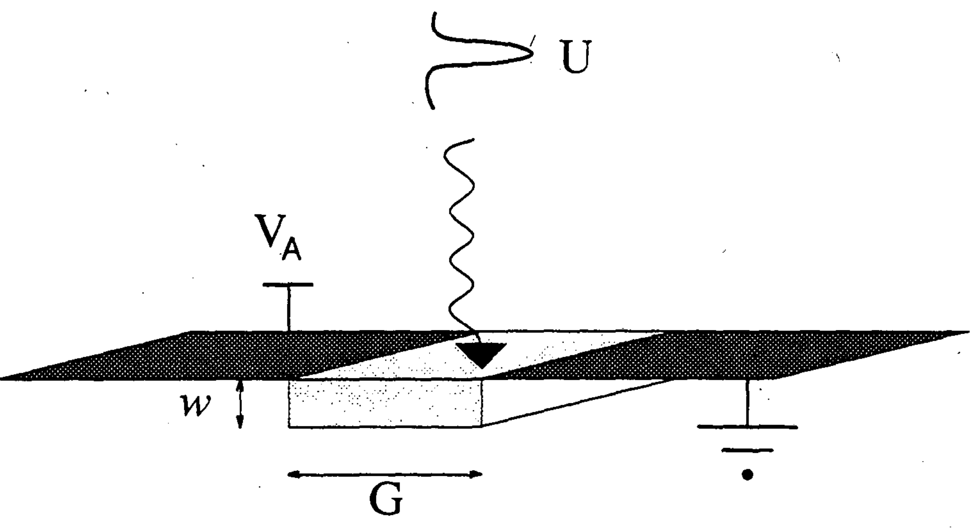


Figure 2.3

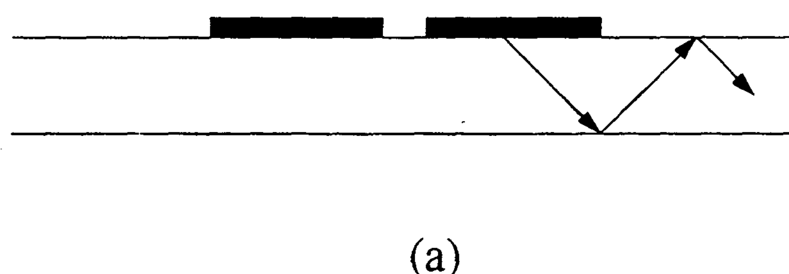

(a)

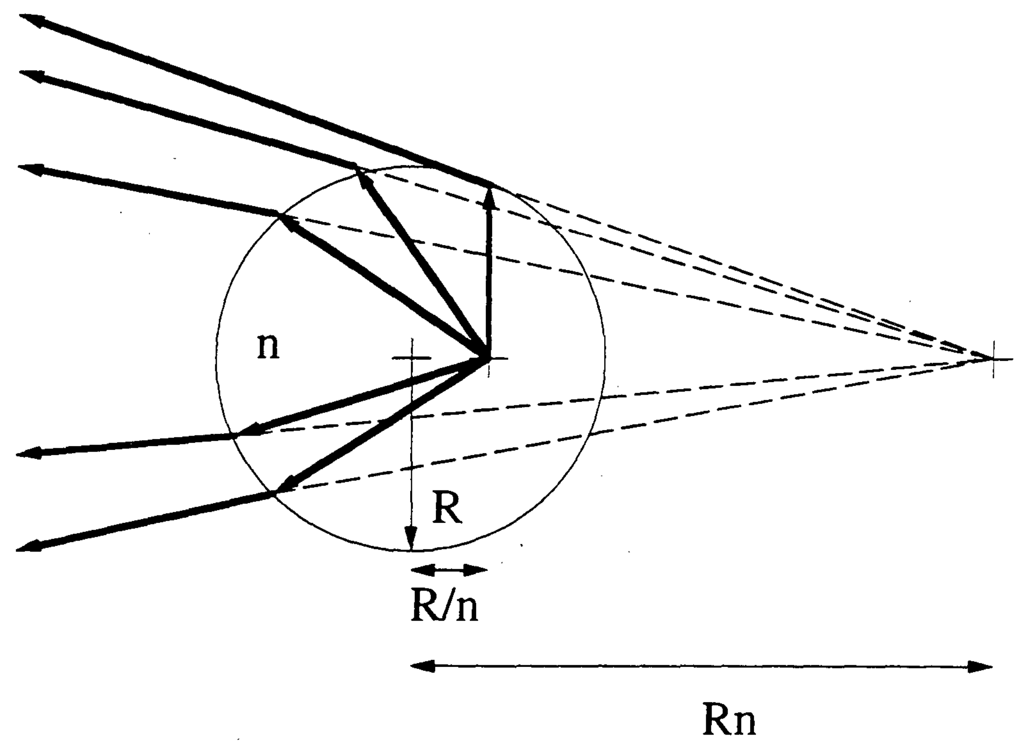


(b) Figure 2.4

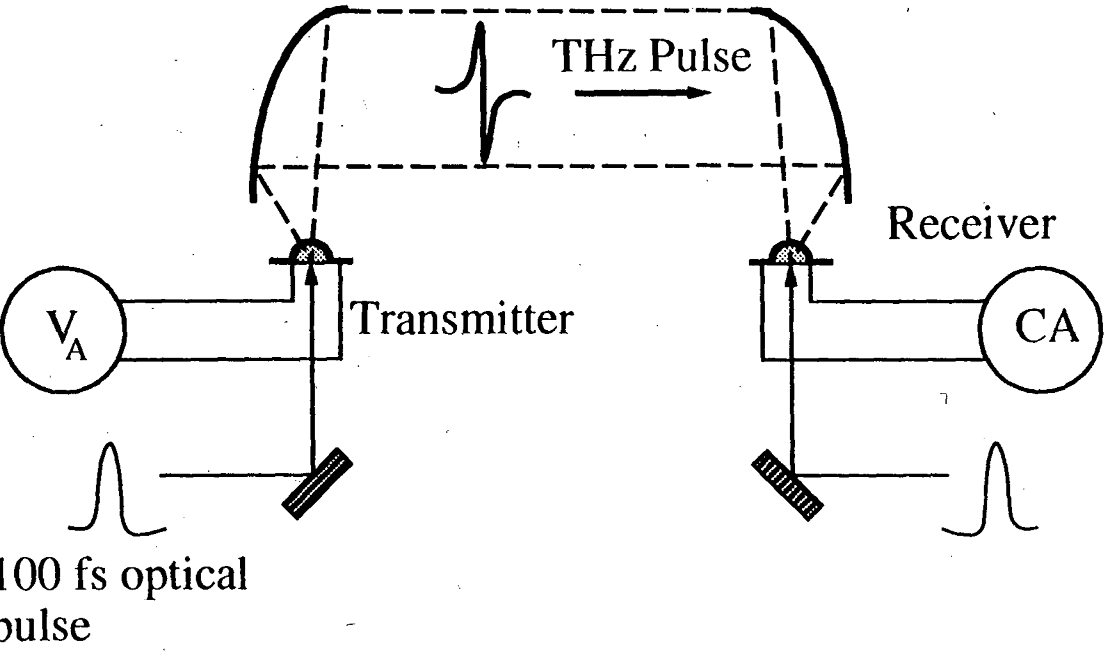


Figure2.5

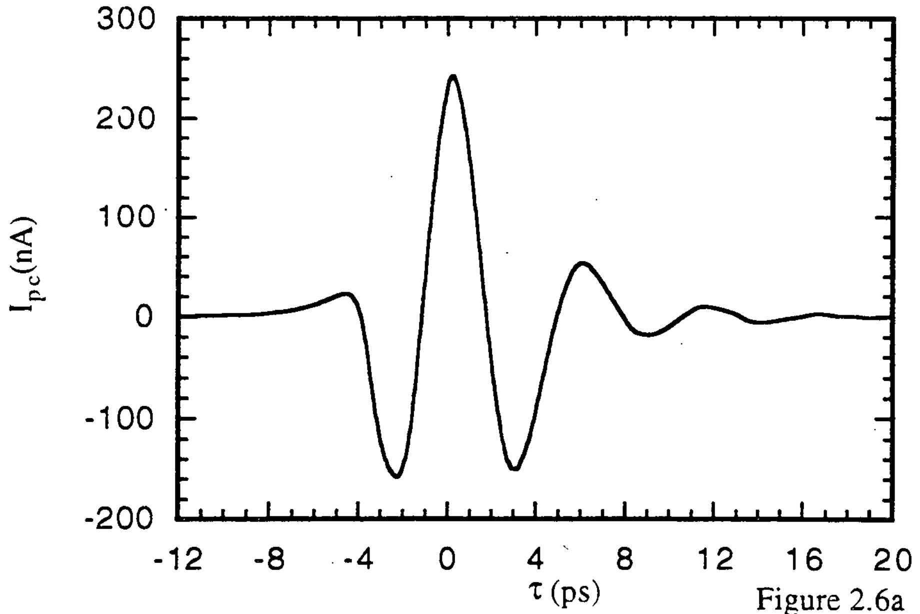


Figure 2.6a

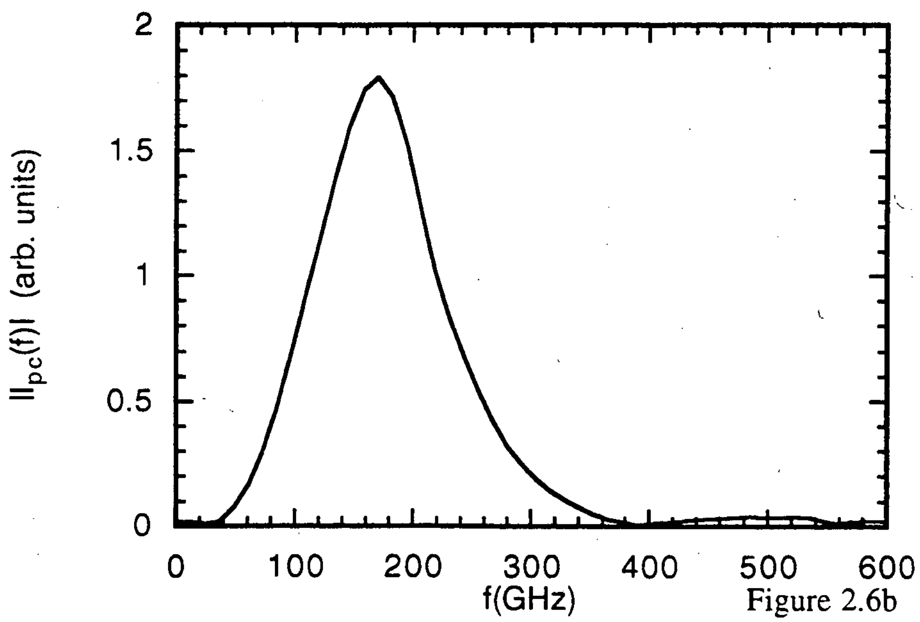

Figure 2.6b

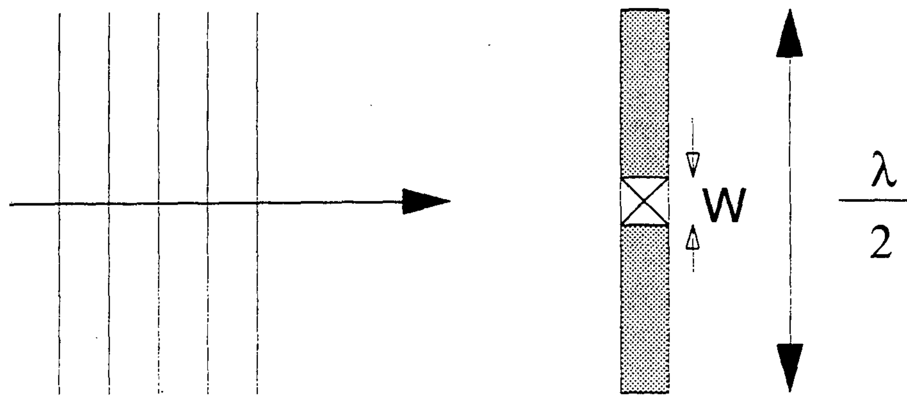


Dipole Antenna

Figure 2.7

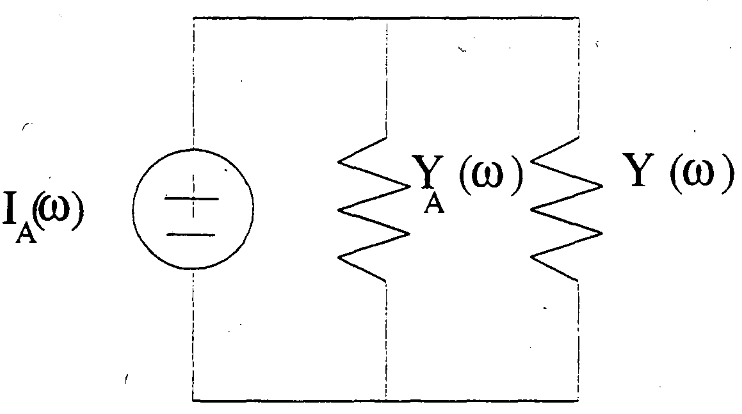


Figure 2.8

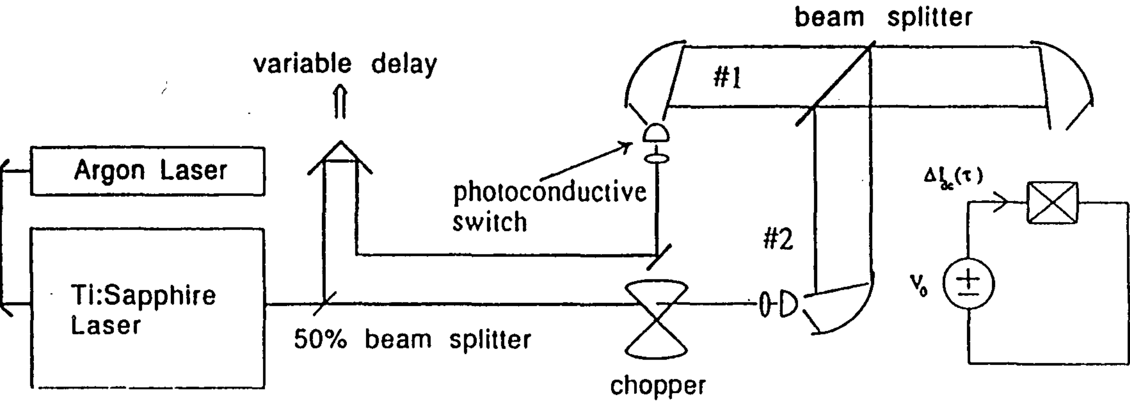


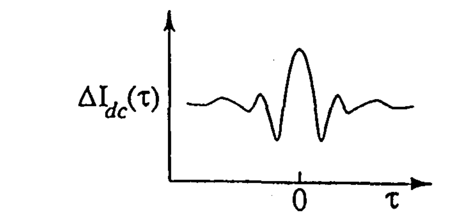


Figure 2.9

# Chapter 3

# *High Frequency Response of Superconducting Tunnel Junctions: Theory*

This Chapter provides the basic theoretical background necessary to understand the high frequency response of conventional low $T_c$ superconducting tunnel junctions. We will begin with the BCS theory [3.1] with its prediction for the density of states and the energy gap of a superconductor. This theory is then applied to problem of quasiparticle tunneling following the theory developed by Cohen, Falicov, and Phillips. Lastly these results will be used in combination with a theory developed by Tucker to explain the linear as well as nonlinear response of superconducting tunnel junctions.

## 3.1 BCS Theory

There are many excellent texts which describe in detail the BCS (Bardeen, Schrieffer, Cooper) theory [3.2-3.4]. Here we only outline the basic results needed to understand quasiparticle tunneling. Specifically we give expressions for the energy gap and the density of states in a superconductor.

Although superconductivity was discovered by Kamerlingh Onnes in 1911 [3.5], it took nearly fifty years before a microscopic theory was developed. It took the insight of Frohlich in 1950 [3.6] to recognize that there can be an effective attractive interaction between pairs of electrons. This effective attraction between electrons is mediated by interactions with crystal lattice vibrations. The origin of the attractive force may be understood by realizing that an electron traveling through a crystal will polarize the medium by attracting the positively charged ions. Physically the electron leaves behind it a track of ion cores. A second electron traveling in the vicinity will see the track of ion cores and will be attracted towards it. In this way there is an apparent attractive interaction between the first and second electron. Obviously there is also a repulsive Coulomb interaction. Normally the Coulomb interaction is a long range interaction, but in a solid Thomas-Fermi screening will reduce the length scale of this interaction.

This idea lead Cooper in 1956 [3.7] to propose that a weak attractive interaction between pairs of electrons can lead to a bound state. He showed that given an arbitrarily small attractive interaction, the Fermi sea of electrons is unstable to the formation of a bound electron pair. This is a direct consequence of the Pauli Exclusion Principle and the existence of a background Fermi sea.

The instability of the Fermi sea forms the basis for the BCS microscopic theory of superconductivity. In a superconductor as the temperature is lowered below $T_c$, the Fermi sea becomes unstable and Cooper pairs form. This is the result of a constant pairwise attractive interaction, -V, between electrons within an energy $\hbar\omega_c$ from the Fermi surface where $\hbar\omega_c$ is the cutoff energy. The new ground state of the system has a lower energy than the unperturbed Fermi sea by an amount, $N(0)\Delta(0)^2/2$, where N(0) is the density of states of the unperturbed normal metal at the Fermi energy and $\Delta(0)$ is the energy gap at zero temperature. The formation of an energy gap means that a minimum energy is needed to excite the system. The elementary excitations of this new system are called quasiparticles.

The BCS theory results in a number of important relations of experimental significance. First $k_BT_c$ is related to $\hbar\omega_c$,

$$k_BT_c = 1.13\hbar\omega_c e^{-1/N(0)V}. \qquad \{3.1\}$$

In the limit of weak coupling ($N(0)V << 1$), $2\Delta(0)\approx3.52k_BT_c$. For bulk niobium, $T_c$=9.25 K and $2\Delta(0)$=3.05 meV [3.4]. In the same weak coupling limit a particularly simple expression is found for the temperature dependence of the energy gap near $T_c$,

$$\Delta(T) \approx \Delta(0) \bullet 1.74\left(1-\frac{T}{T_c}\right)^{1/2}. \qquad \{3.2\}$$

Physically $\Delta$ is a constant as long as long as there are a significant number of Cooper pairs. Only once the number of quasiparticles dominates is the gap driven to zero.

Obviously since the BCS theory predicts the formation of an energy gap, there must be a corresponding change in the density of states. The excitation energies of these new quasiparticles is,

$$E_k = \left(\xi_k{}^2 + |\Delta_k|^2\right)^{1/2}. \qquad \{3.3\}$$

Here $E_k$ is the energy of an excitation with momentum $\hbar k$, and $\xi_k$ is the kinetic energy $\hbar^2k^2/2m$ measured relative to the Fermi energy. In order to compute the density of states in the superconductor, $N_s$, we recognize that there is a one to one correspondence between each quasiparticles and the normal electrons. This gives us a relation between the normal density of states, $N_n$, and $N_s$.

$$N_s(E)dE = N_n(\xi)d\xi. \qquad \{3.4\}$$

Since we are only interested in energies a few mV from the Fermi energy (eV's), we can take $N_n(\xi)=N_n(0)$ which is a constant. Using {3.3} and {3.4} from above, we obtain the simple result,

$$\frac{N_s(E)}{N_n(0)} = \frac{d\xi}{dE} = \frac{E}{\left(E^2 - \Delta^2\right)^{1/2}} \quad (E>\Delta)$$

$$= 0 \quad . \quad (E<\Delta) \qquad \{3.5\}$$

Thus the density of states is divergent at E=Δ. Physically the states which previously had energies within the gap have been pushed up to states with energies greater that Δ. Equation {3.5} predicts that this divergence should be absolutely sharp. The sharpness of this divergence is the result of the assumption that the attractive interaction has a sharp cutoff at $\hbar\omega_c$. In real materials this sharp cutoff will be smeared over the whole range $\hbar\omega_c$ by the phonon mediated interaction. This smearing will in turn smooth out the divergence in the density of states. These corrections are of order $(\Delta/\hbar\omega_c)^2$ or $(T_c/\Theta_D)^2$, where $\Theta_D$ is the Debye temperature.

## 3.2 Superconductive Tunneling

Experiments in the area of superconductive tunneling have proven to be fertile soil for both basic and applied research. The first single particle (quasiparticle) tunneling experiments through a thin insulating barrier between a normal metal and a superconductor (NIS) and between two superconductors (SIS) were performed by Giaver in 1960 [3.8]. He showed that at temperatures well below $T_c$, no current could flow through an NIS junction unless the applied voltage across the junction exceeded Δ. He used this technique to confirm the density of states and temperature dependence of the energy gap as predicted by the BCS theory. Within only two years, Josephson predicted that a pair of electrons might tunnel through an SIS junction even with zero applied voltage [3.9]. Since that time there have been numerous experiments on Josephson and quasiparticle tunneling. The Josephson effect forms the basis for ultrasensitive measurements of small magnetic fields using a SQUID (Superconducting Quantum Interference Device). In addition there has been much recent work on Josephson junction integrated circuits using Rapid Single-Flux

Quantum logic operating at ultrahigh clock frequencies in excess of 100 GHz [3.10]. Quasiparticle tunneling on the other hand has been shown by Paul Richards to have nearly ideal properties for making microwave heterodyne mixers with low-noise. We will concentrate on the quasiparticle tunneling current and follow the treatment of Cohen, Falicov, and Phillips [3.11] to compute the *dc* nonlinear current-voltage(I-V) characteristics of an SIS tunnel junction.

We begin with the Hamiltonian formulation for the tunneling problem. In this case the SIS system is described by an effective Hamiltonian,

$$H = H_L + H_R + H_T + eV(t)N_L, \qquad \{3.6\}$$

where $H_L$ and $H_R$ are the complete many-body Hamiltonians for the left and right side respectively, V(t) is the applied voltage across the junction, and $N_L$ is the number operator on the left hand side,

$$N_L = \sum_k c_k^+ c_k \quad . \qquad \{3.7a\}$$

$H_T$ is the one body Hamiltonian which transfers electrons from one superconductor to the other,

$$H_T = \sum_{k,q} \left( T_{kq} c_k c_q^+ + T_{kq}^* c_q c_k^+ \right) \quad . \qquad \{3.7b\}$$

Here $c_k$ ($c_q$) and $c_k^+$ ($c_q^+$) correspond to electron annihilation and creation operators for the left (right) sides of the barrier. $T_{kq}$ is a phenomenological tunneling matrix element which transfers quasiparticles from the right to the left electrode. Equation {3.7b} simply states that for a thin barrier there is finite quantum mechanical probability that an electron will tunnel across the barrier. This probability will decrease exponentially with the thickness of the barrier and depends on the details of the oxide layer. All these factors are lumped into $T_{kq}$.

If we neglect coherent process which result in Josephson tunneling, then the transition probability and hence the tunneling current through the junction is proportional to the tunneling matrix element squared. In order to calculate this term, c and $c^+$ must be expressed in terms of the elementary (Bogoliubov) quasiparticle excitations of the superconductor,

$$c_k = u_k \alpha_k^+ + v_k^* \beta_k . \qquad \{3.8\}$$

Here $\alpha^+$ and $\beta$ are the electron like creation and hole like destruction operators respectively and u and v are the BCS coherence factors. From this expression and a similar expression for $c^+$, the square of the tunneling matrix can be found. By summing the current from left to right and from right to left, the total current is found to be proportional to,

$$\left(\left|u_k\right|^2 + \left|v_k\right|^2\right)\left|T_{kq}\right|^2 = \left|T_{kq}\right|^2 . \qquad \{3.9\}$$

The above equality holds due to the normalization condition on the coherence factors. Thus the tunneling current only depends on the tunneling matrix element but does not depend on the nature of superconducting ground state through coherence factors of the form $u_k v_k$.

The disappearance of the coherence factors in {3.9} allows us to use the simplified semiconductor model for a superconductor. In this model the superconductor is represented by an ordinary semiconductor with a density of states given by {3.5} which is applied to both positive and negative energies. The chemical potential is set to the zero of energy. At T=0, all states below the chemical potential are filled and all states above the chemical potential are empty. At finite temperature, the occupation number of the states is simply give by the Fermi-Dirac distribution function. In this model the transitions across the barrier are elastic, that is they conserve energy. Inelastic processes such as scattering by phonons in the barrier are neglected. Within this model the current in linear response is given by,

$$I_{dc}(V) = \frac{2\pi e}{\hbar^2} \sum_{kq\sigma} \int_{-\infty}^{\infty} d\omega_L d\omega_R |T_{kq}|^2 A_L(k,\omega_L) A_R(k,\omega_R) \times \qquad \{3.10\}$$
$$[f(\hbar\omega_L) - f(\hbar\omega_R)] \delta(eV/\hbar + \omega_L - \omega_R)$$

Here $f(\hbar\omega)=(\exp(\hbar\omega/k_BT+1)^{-1}$ is just the Fermi function and $A_L$ and $A_R$ are the single particle spectral distribution functions for the left and right sides of the barrier respectively. According to BCS theory the spectral distribution function is given by

$$A(k,\omega) = |u_k|^2 \delta(\omega - E_k/\hbar) + |v_k|^2 \delta(\omega - E_k/\hbar), \qquad \{3.11\}$$

where $v_k^2=1-u_k^2=1/2(1-\xi_k/E_k)$ is the probability that a given pair $(k\uparrow, -k\downarrow)$ is occupied in the BCS ground state. By substituting equation {3.11} into equation {3.10} we obtain the simple result for the *dc* tunneling I-V curve,

$$I_{dc}(V) = \frac{1}{R_N} \int_{-\infty}^{\infty} dE \frac{E - eV}{\sqrt{(eV-E)^2 - \Delta^2}} \frac{E}{\sqrt{E^2 - \Delta^2}} [f(E - eV) - f(E)]. \qquad \{3.12\}$$

In this result $T_{kq}$ is assumed to be constant and is absorbed into the normal state resistance, $R_N$.

The above calculation for the *dc* current may have been obtained in a more simple fashion using the semiconductor model [3.4]. The density of states {3.5} of the single particle excitations at zero temperature is shown in Figure 3.1 in the presence of and applied bias V. The tunneling current from left to right for a quasiparticle at energy E is, according to the Fermi's Golden rule calculation,

$$I_{kq} = (2\pi e/\hbar)|T_{kq}|^2 N_R(E) \qquad \{3.13\}$$

where $N_R(E)$ is the density of states on the right side of the barrier. This expression when summed over all the quasiparticle states on the right side of the barrier leads to expression {3.12}. From Fig 3.1 we see that no tunneling current can flow until the voltage, V, reaches a critical value, $eV=2\Delta$. At this point there are empty states on the right hand side

for the quasiparticles to tunnel into. The sharp divergence in the density of states will lead to a sharp onset in the tunneling current. As the applied bias is increased the tunneling current will asymptotically approach the value $V/R_N$ which is just the normal state tunneling current. The process of quasiparticle tunneling can be thought of as the unbinding of a Cooper pair. The binding energy of a Cooper pair is simply $2\Delta$. When eV exceeds this value, the Cooper pair unbinds and a quasiparticle tunnels across the barrier to an empty state, leaving behind the other quasiparticle. Figure 3.2(a) shows the experimentally measured I-V curve at 1.6 K for the 2x2 μm $Nb/AlO_x/Nb$ SIS tunnel junction used in the experiments of Chapter 4. The most striking feature is the sharp onset in the current at 2.7 mV. The sharp onset, though, is broadened by such effects as gap inhomogeneity, gap anisotropy, and quasiparticle lifetime broadening.

## 3.3 High Frequency Response

In the previous Section we concentrated on the calculation of the *dc* current in response to a *dc* voltage. In this Section we focus on the current which is induced in response to a sinusoidal time dependent voltage, $V(t)=V_0+V_\omega \cos(\omega t)$. Since the I-V curve (Fig. 3.2(a)) for an SIS tunnel junction is nonlinear, we would expect to obtain a rectified current at *dc* as well as oscillating currents at the fundamental frequency, $\omega$, and all higher harmonics. This is similar to the case of a classical crystal rectifier.

In the case of a diode, the currents can be calculated easily using classical mixer theory. This is also true for an SIS tunnel junction when the frequency is sufficiently low. At high frequencies in the hundreds of GHz range, the classical mixer approach breaks down and the SIS response must be evaluated with a semi-classical quantum approach. High frequency is determined by the condition that $\hbar\omega/e$ be much greater than the voltage scale of the nonlinearity, $\delta V$, in the *dc* I-V curve (see Fig. 3.5(a)). At high frequencies, the SIS junction begins to resemble other quantum detectors in the visible and near infrared such as photomultipliers, photoconductors, and photodiodes. These devices are all based

on the photoelectric effect. In the familiar case of a photomultiplier, an individual electron absorbs a single photon. If the photon energy is greater than the work function of the metal, then a free electron is generated and a current may be detected. This current is a measure on the incident photon flux. The SIS tunnel junction operates in a similar fashion but the currents are the result of photon assisted tunneling rather than photoelectron ejection. In addition, the SIS junction has the added benefit that its *work function* can be tuned with an applied *dc* voltage.

To understand the phenomena of photon assisted tunneling we begin with the simplified semiconductor model given previously. Recall that this model neglects the admixture of *electron* and *hole* like properties of quasiparticles near the band edge. These effects were shown in Section 3.2 above to be unimportant for single quasiparticle tunneling. Figure 3.3(a) shows the density of states of the SIS junction in the presence of both an applied *dc* bias, $V_0$, and a microwave signal, $\hbar\omega$. Figure 3.3(b) show the first measurements of photon assisted tunneling in a Al-$Al_2O_3$-In tunnel junction [3.12]. The *dc* V-I curve in the absence of a microwave field is given by the solid curve in Figure 3.3(b). The dashed curve in Fig. 3.3(b) shows the appearance of a step like structure in the *dc* V-I curve in the presence of CW microwaves (pumped V-I curve) at 38 GHz. This step like structure can be understood by referring to Fig. 3.3(a). In the presence of a microwave field, the quasiparticles incident on the barrier may absorb *n* multiple quanta of energy. When the quasiparticle absorbs enough energy so that $n\hbar\omega+eV_0 > 2\Delta$ then a new channel for quasiparticle tunneling will open and photon steps will appear in the *dc* I-V curve. The width of a step in voltage is $\hbar\omega/e$, and as we shall show later, the number of steps that appear is given by $\alpha=eV_\omega/\hbar\omega$. The current steps below the sharp onset correspond to the absorption of multiple quanta, $n\hbar\omega$. Above the sharp onset there are also steps, but this time there is an overall decrease in the current. The decrease in current corresponds to the emission of multiple quanta.

The semiconductor model gives an immediate explanation for the condition that $\hbar\omega/e >> \delta V$ in order to see photon steps. At sufficiently high frequency the step like structure in the pumped I-V curve will be a direct reflection of the sharp step like structure in the original I-V curve. As the frequency is lowered, though, the sharp steps will begin to smear out. At sufficiently low frequency, the applied microwave field will simply average over the nonlinearity and the SIS junction will operate just like a classical mixer. In the classical regime the applied field can be thought of as modulating the applied voltage. Since the I-V curve is nonlinear, a rectified current will result.

A common misconception is that $\hbar\omega/e >> \delta V$ in order to observe photon assisted tunneling. The fact is that any induced current observed in the presence of a microwave field can be understood in terms of the photon-assisted tunneling picture. Even when the frequency is in KHz range the photon-assisted picture can be applied. The problem is that the photon picture becomes unwieldy since at low frequencies we are typically in the multiple photon regime. The number of photons involved is given roughly by $eV_\omega/\hbar\omega$. For example, at a frequency of 1 KHz and a voltage of 1 $\mu$V approximately 250 photons interact with the junction. In this low frequency multiphoton regime it is easiest to treat the SIS junction as a classical mixer rather than use the full quantum mixer theory.

The semiconductor model gives a simple prescription for calculating the induced currents in the SIS junction. We begin with the simple case of two superconducting films separated by a thin insulating barrier. Let the right side of the junction be grounded for convenience and then apply a time dependent voltage, $V(t)=V_0+V_\omega\cos(\omega t)$, to the left side of the barrier.

To compute the resulting tunneling current, we must consider the quasiparticle excitations in the left lead. In order to simplify the calculation, we make the critical assumption that the quasiparticle wave function drops off sharply in the insulating region of the barrier. This is true when the barrier height in the insulator is large which causes the wave function to decay rapidly. This is indeed the case since the barrier height in the

insulator is typically many eV above the Fermi energy in the superconductor. Within this approximation, the interaction between the microwave field and the quasiparticles in the insulating region will be vanishingly small and can be neglected. When this is done, the action of the microwave field is simply to adiabatically modulate the energy of the quasiparticles. The adiabatic approximation assumes that the frequency is below the plasma frequency in the leads. This is typically well into the ultraviolet regime.

In the presence of the microwave field, the new Hamiltonian for the system becomes,

$$H=H_0+eV_0+eV_\omega\cos(\omega t), \qquad \{3.14\}$$

where $H_0$ is the unperturbed Hamiltonian in the absence of the microwave field. The unperturbed wave function incident on the barrier is given by,

$$\Psi(x,t)=\Psi(x)e^{-jEt/\hbar}. \qquad \{3.15\}$$

Here E is the unperturbed energy of the Bloch state. Since the perturbation to the Hamiltonian contains no spatial dependence, the new electronic wave function has the form,

$$\Psi(x,t)=\Psi(x)e^{-j(E+eV_0)t/\hbar}\bullet\sum_{n=-\infty}^{\infty}J_n(eV_\omega/\hbar\omega)e^{-jn\omega t} \qquad \{3.16\}$$

It is important to realize that this is an exact result which is correct to all orders in the perturbation and its validity hinges on the rapid decay of the wave function into the insulator. The interpretation of {3.16} is that each quasiparticle level is displaced by an energy $n\hbar\omega$ with a probability amplitude of occupancy given by $J_n(\alpha=eV_\omega/\hbar\omega)$. Figure 3.4 illustrates the generation of photonic side bands. Since all the levels are modulated together, the displacements in energy are equivalent to an effective *dc* bias, $V_0+n\hbar\omega$, across the junction with a weighting factor of $J_n^2(\alpha)$. From this picture, Tien-Gordan [3.12] obtained an expression for the *dc* tunneling current,

$$I_0(V_0,V_\omega)=\sum_{n=-\infty}^{\infty}J_n^2(\alpha)I_{dc}(V_0+n\hbar\omega), \qquad \{3.17\}$$

where $I_{dc}$ is the tunneling current in the absence of microwaves. In computing this result it is assumed that the barrier in the insulator is infinitely high so that the tunneling probability is independent of quasiparticle energy. Equation {3.17} explains directly the photon steps observed in the pumped V-I curve in Fig. 3.3(b). The tunneling current is just the summation of many *dc* V-I curves displaced by a voltage, $V_0+n\hbar\omega$, and weighted by $J_n^2(eV_\omega/\hbar\omega)$. The number of steps that appear is given roughly by $\alpha$. This can be understood by recognizing that $J_n(\alpha)$ goes rapidly to zero for $n>\alpha$.

For the purposes of this thesis it will be important to obtain an expression for the change in the *dc* tunneling current, $\Delta I_{dc}$, when the amplitude of the microwave voltage or equivalently $\alpha$ is small. By expanding the Bessel functions in {3.17}, we obtain the following result,

$$\Delta I_{dc}(V_0)=\frac{1}{4}V_\omega^2\left[\frac{I_{dc}(V_0+\hbar\omega/e)-2I_{dc}(V_0)+I_{dc}(V_0-\hbar\omega/e)}{(\hbar\omega/e)^2}\right]. \qquad \{3.18\}$$

The quantity in brackets is the finite second difference of the *dc* I-V curve where the term $V_0+\hbar\omega/e$ corresponds to photon absorption and $V_0-\hbar\omega/e$ corresponds to photon emission. All other higher order multiphoton processes are unimportant for this low power case. In the limit that the frequency is small, the finite second difference will eventually approach the second derivative of the *dc* I-V curve. Replacing the term in brackets with the second derivative results in the same expression derived previously in equation {2.7} for classical rectification in a nonlinear diode. It is clear that the crossover between the *quantum* to the *classical* regime occurs when $\hbar\omega/e$ becomes smaller than the voltage scale of the nonlinearity of the I-V curve.

The simplified model above allows us to easily calculate the rectified tunneling current, but it does not allow us to calculate the time dependent currents that flow through

the junction. Werthamer [3.14] has developed via perturbation theory an expression for the full tunneling current based on the Hamiltonian given in equation {3.6},

$$\langle I(t)\rangle = \mathrm{Im}\int_{-\infty}^{\infty} d\omega d\omega' \left(W(\omega)W^*(\omega')e^{-i(\omega-\omega')t} j_{qp}(\omega' + eV_0/\hbar) + W(\omega)W(\omega')e^{-i(\omega+\omega')t+i\phi} j_p(\omega' + eV_0/\hbar)\right). \quad \{3.19\}$$

This technique computes correctly the quasiparticle as well as the Josephson tunneling current. The first term above is the quasiparticle tunneling current while the second term is the Josephson current. Here $j_{qp}$ and $j_p$ are the quasiparticle and Josephson response functions respectively. The Josephson term is similar to the quasiparticle term except that the former depends on the phase difference, $\phi$, between the BCS ground state wave functions on the two sides of the junction. The function $W(\omega)$ is the Fourier transform of the time evolution operator, $W(t)$, which is found in the interaction picture of time-dependent perturbation theory to be,

$$W(t) = \exp\left(-i\frac{e}{\hbar}\int_t dt'\, V(t') - V_0\right) = \int_{-\infty}^{\infty} d\omega W(\omega)e^{-i\omega t}. \quad \{3.20\}$$

$j_{qp}$ and $j_p$ can be calculated exactly for an ideal junction using the density of states for the quasiparticles and the Cooper pairs [3.14]. This calculation is difficult and cannot be applied to real junctions which have a broadened step in the *dc* I-V curve. In the case of a real junction it is better to obtain $j_{qp}$ directly from the *dc* I-V curve. To see how this is done consider the following analysis. When the voltage across the junction contains only a *dc* component, $V_0$, then $W(\omega)=\delta(\omega)$ and {3.19} becomes,

$$\langle I(t)\rangle = \mathrm{Im}\left[j_{qp}(eV_0/\hbar)\right] + \mathrm{Re}\left[j_p(eV_0/\hbar)\right]\sin\phi + \mathrm{Im}\left[j_p(eV_0/\hbar)\right]\cos\phi. \quad \{3.21\}$$

The Josephson relation $\dot{\phi} = 2eV_0/\hbar$ tells us the second and third terms oscillate at the Josephson frequency while the first term results in a *dc* contribution. Thus the imaginary part of the quasiparticle response function is just the *dc* tunneling current,

$$I_{dc}(V_0) = \mathrm{Im}\left[j_{qp}(\omega_0)\right] \qquad \{3.22a\}$$

where $\omega_0 = eV_0/\hbar$. The *dc* tunneling current only depends on the imaginary part of the quasiparticle response function. The real part of the quasiparticle response function plays no role and can only be measured by measuring the reactive time dependent currents through the junction.

The Re[$j_{qp}$] may be found from the Kramers-Kronig transform of Im[$j_{qp}$]. The Kramers-Kronig transform may be applied to any bounded and causal response function. By analogy with equation {3.21}, we can define an $I_{kk}$-V curve which is related to the real part of the quasiparticle response function, $I_{kk}(V_0) = \mathrm{Re}\left[j_{qp}(\omega_0)\right]$. If we assume that we know the *dc* I-V curve for all voltages then we can compute $Im[j_{qp}(\omega_0)]$ for all frequencies. Using $Im[j_{qp}(\omega_0)]$ we can compute $Re[j_{qp}(\omega_0)]$,

$$\mathrm{Re}\left[j_{qp}(\omega)\right] = P\int_{-\infty}^{\infty}\frac{d\omega'}{\pi}\frac{\mathrm{Im}\left[j_{qp}(\omega')\right] - \hbar\omega'/eR_N}{\omega - \omega'}$$

$$I_{kk}(V) = P\int_{-\infty}^{\infty}\frac{dV'}{\pi}\frac{I_{dc}(V') - V'/R_N}{V' - V}. \qquad \{3.22b\}$$

Here P stands for the principle value of the integral. In this formula for $I_{kk}$, the ohmic term from the *dc* I-V curve has been subtracted to avoid a divergence in the integral. The ohmic term does not effect the Kramers-Kronig transform since only the nonlinear part of the I-V curve will result in a reactive component of $I_{kk}$. Figure 3.2(b) shows a direct calculation of $I_{kk}$(V) from the *dc* I-V curve in Fig. 3.2(a). The sharp divergence in $I_{kk}$ at the gap voltage is the result of the sharp step in the *dc* I-V curve. For the case of an ideal BCS junction, $I_{kk}$ diverges logarithmically [3.13,3.14]. This can be understood by noting that the Kramers-Kronig transform of a delta function is a function which diverges as $1/\omega$. Since a step function is the integral of a delta function, the Kramers-Kronig transform will go like the integral of $1/\omega$ which is a logarithmic divergence.

The results developed above by Werthermer give a direct procedure to compute the time dependent current in the presence of an arbitrary voltage waveform. The first step is to measure the *dc* I-V curve which via equations {3.22a,b} can be used to compute the quasiparticle response functions. The next step is to compute the time evolution operator, W(t) in equation {3.20} using as input the time dependent voltage that appears across the junction. With the computed quasiparticle response functions and the Fourier transform of W(t) placed in equation {3.19}, the time dependent current can easily be found. It is important to recognize that the voltage that appears in equation {3.20} must be calculated in a self consistent manner since the applied voltage and the true voltage that appears across the junction can differ due mixing of different harmonics.

Rather that treat the general case with an arbitrary V(t), we follow the treatment by Tucker who considered the specific case of $V(t)=V_0+V_\omega\cos(\omega t)$. In his formulation, he makes the simplifying assumption that all higher harmonics in the voltage that appear across the junction are shorted out. This is typically a good assumption since the geometrical junction capacitance shorts outs the higher harmonics. In this simplified case the applied voltage and the true voltage are equivalent making the calculation relatively straight forward. With the voltage waveform as input, Tucker calculates via equation {3.20} the time evolution operator, W(t). Using this result along with the expressions {3.22a,b} for the quasiparticle response functions in equation {3.19}, Tucker computes an expression for the time dependent tunneling current,

$$I(t) = a_0 + \sum_{m=1}^{\infty} 2a_m \cos(m\omega t) + 2b_m \sin(m\omega t) \qquad \{3.23\}$$

$$2a_m = \sum_{n=-\infty}^{\infty} J_n(\alpha)[J_{n+m}(\alpha) + J_{n-m}(\alpha)] I_{dc}(V_0 + n\hbar\omega / e) \qquad \{3.24\}$$

$$2b_m = \sum_{n=-\infty}^{\infty} J_n(\alpha)[J_{n+m}(\alpha) + J_{n-m}(\alpha)] I_{kk}(V_0 + n\hbar\omega / e). \qquad \{3.25\}$$

The first term, $a_0$, is just the equation for the *dc* current in the presence of microwaves that we obtained earlier in equation {3.17} with the simpler Tien-Gordan approach. The other

terms are at the fundamental and the harmonics of the driving frequency. Harmonic generation is not surprising since any classical nonlinear circuit element is expected to give rise to harmonic signals. What is surprising is that we get two contributions to the current. The first is the expected cosine term which is in phase with the applied voltage. The second term is a sine term which is out of phase by 90 degrees. The sine term has no classical analog and is a direct result of the fact that the tunnel junction has a sharp nonlinearity in the *dc* I-V curve.

In order to understand the cosine and sine terms further, let us make the simplifying assumption that we are in the small signal limit defined by $\alpha \ll 1$. In this limit all harmonic mixing can be neglected and we enter the regime of *linear* response. In the regime of linear response, current at the fundamental frequency, $I_\omega$, can be written as,

$$I_\omega = Y(\omega) \bullet V_\omega = [G(\omega) + jB(\omega)]V_\omega. \qquad \{3.26\}$$

Here we use standard phasor notation in which the true time dependent signal, I(t), is found by taking the real part of $I_\omega \exp[j\omega t]$. The complex admittance, $Y(\omega)$, of the tunnel junction can be written as the sum of the two terms. The first term is the quantum conductance, $G(\omega)$, which gives the amplitude of the in phase currents while the second term is the quantum susceptance, $B(\omega)$, which gives the amplitude of the out of phase currents. The term quantum is used by the SIS community to indicate that the admittance is frequency dependent. As we shall discuss later, the admittance of a tunnel junction is entirely analogous to the admittance of an atomic system. By expanding equations {3.23-3.25} to lowest order in $\alpha$, we obtain the following expressions for $G(\omega)$ and $B(\omega)$,

$$G(\omega) = \frac{e}{2\hbar\omega}[I_{dc}(V_0 + \hbar\omega / e) - I_{dc}(V_0 - \hbar\omega / e)] \qquad \{3.27\}$$

$$B(\omega) = \frac{e}{2\hbar\omega}[I_{kk}(V_0 + \hbar\omega / e) - 2I_{kk}(V_0) + I_{kk}(V_0 - \hbar\omega / e)] \qquad \{3.28\}$$

The equations {3.27,3.28} for the conductance and the susceptance respectively show explicitly that these quantities can be computed from the experimentally accessible *dc* I-V

curves. Thus a simple *dc* transport measurement can reveal the transport properties of an SIS tunnel junction in the 100's of GHz regime.

From equation {3.27}, $G(\omega)$ can be found by taking the finite difference derivative of the *dc* I-V curve. The finite difference interval in this case is given by the *photon voltage*, $\hbar\omega/e$. Figure 3.5 shows a graphical approach to calculating the high frequency conductance. Let us assume that we have applied a *dc* bias of $V_0$=2.3 mV, and that we are operating at a frequency of 180 GHz. For reference, one mV corresponds to the amount of energy in a single 240GHz photon. The conductance at 180 GHz is then just the slope of the solid line drawn through the two points, $V_0 \pm \hbar\omega/e$. For this case the conductance is 155 mmhos. It is clear from this graphical representation that the high frequency conductance differs greatly from the classical small signal conductance which is the slope of the curve at the *dc* bias point. The slope of the dashed curve in Fig. 3.5 is the classical conductance which is just 3 mmhos which is roughly fifty times smaller than the conductance at 180 GHz. Thus it is clear from this example that at high frequencies we cannot neglect the frequency dependence in the conductance. It is also clear from Fig. 3.5 that the *dc* conductance and the high frequency conductance will begin to differ whenever the photon voltage begins to exceed the voltage scale of the nonlinearity, $\delta V$. We obtained a similar criterion previously in equation {3.18} when we discussed the crossover from *classical* to *quantum* rectification.

Figure 3.6 further emphasizes the dramatic frequency dependence of the conductance at two different *dc* bias voltages. At a *dc* bias of 2.6 mV, the low frequency conductance starts at 35 mmhos. As the frequency is raised to 80 GHz the conductance rapidly peaks at 355 mmhos and then goes away slowly as the frequency is raised into the hundreds of GHz regime. The sharp onset in the conductance can be understood easily by referring once again to the semiconductor model in Fig. 3.3(a). A quasiparticle incident from the left at energy $E_A$ will absorb a photon and then tunnel into a state at energy $E_B$. The condition for energy conservation tells us that $E_B - E_A = \hbar\omega$. At low frequencies there

are no available states at $E_B$ so the conductance is nearly zero. As the frequency is raised sufficiently high enough so that $\hbar\omega > 2\Delta\text{-}eV_0$, then at energy $E_B$ there is a sharp increase in the density of states. This sharp increase is directly reflected in the fast onset in the conductance. Fig. 3.6 also shows the frequency dependent conductance as the *dc* bias is lowered to 2.3 mV. As is expected the lowering of the bias pushes the peak in the conductance up to higher frequencies. In fact the bias change of 0.3mV corresponds exactly to the peak shift of 75 GHz.

Although we have discussed the origin of the frequency dependence of the conductance, we have not explained the appearance of the quantum susceptance. We know from quantum mechanics that in addition to *real* transitions which give rise to a conductance there are also *virtual* transitions which will result in a susceptance. In a real transition the energy conservation condition, $E_B\text{-}E_A = \hbar\omega$, must hold. However, in a virtual transition the energy conservation condition need not hold. Refer once again to Fig. 3.3(a). A quasiparticle incident from the left at energy $E_A$ undergoes a virtual excitation to an energy $E_B$ where $E_B \neq E_A + \hbar\omega$. This virtual excitation is short lived. However, if the excited state lives long enough and there are available states to tunnel to on the right side of the barrier, then the quasiparticle can tunnel across. Once on the right side, the quasiparticle tunnels back to the left side and then relaxes to a state with energy $E_A$ with the emission of a photon. There is no net absorption of photons in this process. Instead there is a *quantum mechanical sloshing* of quasiparticles across the barrier [3.15]. The currents produced by this sloshing are non-dissipative and have no classical analog. For example a crystal diode lacks a quantum susceptance.

We can compute $B(\omega)$ for our tunnel junction using equation {3.28}. This process requires the calculation of $I_{kk}$, the Kramers-Kronig transform of the *dc* I-V curve, as shown in Fig. 3.2(b). The next step is to compute the finite second difference of the $I_{kk}$ curve. Figure 3.7 shows the result of this calculation for $B(\omega)$ for two different bias voltages. First consider the case for $V_0$=2.6mV. $B(\omega)$ starts at zero and then it rapidly

rises to 225 mmhos at 50 GHz. This is the same order of magnitude as the peak conductance. As the frequency is increased further, the susceptance drops rapidly and goes through zero at 90 GHz. For still higher frequencies the susceptance remains negative. As expected as the bias is lowered to 2.3 mV, the peak in the susceptance moves to higher frequencies.

A positive susceptance corresponds to a capacitive like response while a negative susceptance corresponds to an inductive response. Thus at low frequencies the tunnel junction responds capacitively while at high frequencies the junction responds inductively. This behavior is of great practical importance since this intrinsic susceptance of the junction can in fact tune out the geometrical capacitance of the device and greatly modify the coupling of power into the junction. In fact Worsham *et. al.* [3.16] has recently proposed that SIS tunnel junctions be used as voltage tunable reactive elements in high performance microwave detectors.

Rather than use equation {3.28} to compute B(ω), B(ω) can also be obtained from the Kramers-Kronig transform of G(ω),

$$B(\omega) = \frac{\omega}{\pi} P \int_{-\infty}^{\infty} \frac{d\omega'}{\omega'} \frac{G(\omega')}{(\omega' - \omega)}. \qquad \{3.29\}$$

The above result can be used to explicitly show the capacitive nature of the tunnel junction at low frequencies. The susceptance for a simple capacitor, C, is just ωC. At low frequencies, equation {3.29} reduces to a similar form with, $B(\omega)=\omega C_j$ , where the junction capacitance $C_j$ is given by,

$$C_j = \frac{1}{\pi} P \int_{-\infty}^{\infty} d\omega' \frac{G(\omega')}{(\omega')^2}. \qquad \{3.30\}$$

This equation shows that the *dc* junction capacitance can be found by integrating the frequency dependent conductance over all frequencies. As we saw in Fig. 3.6, reducing the *dc* bias pushes the onset of the conductance to higher frequencies. From equation

{3.30}, this will lead to a corresponding lower capacitance. This effect is entirely analogous to that seen in atomic systems. We know that an atomic system becomes less polarizable as the spacing between the energy levels is increased.

In the quantum regime, the properties of the SIS tunnel junction resemble most closely an atomic system, rather than a classical nonlinear diode. Just as the SIS tunnel junction has a frequency dependent complex admittance, an atomic system has a frequency dependent complex conductivity, $\sigma$. This complex conductivity it normally separated into real and imaginary parts, $\sigma=\sigma_1+j\sigma_2$. Consider the case of a solid with N atomic systems imbedded in a matrix with dielectric constant $\varepsilon$, each with an infinitely lived resonant absorption line at frequency $\omega_0$. The conductivity of this system is given by [3.17],

$$\sigma_1 = \varepsilon\omega_p^2 \frac{\pi}{2}\delta\left(\omega^2 - \omega_0^2\right) \qquad \{3.31a\}$$

$$\sigma_2 = \varepsilon\omega_p^2 \frac{\omega}{\omega_0^2 - \omega^2}. \qquad \{3.31b\}$$

Here $\omega_p$ is the plasma frequency for the solid.

The delta function in $\sigma_1$ above represents absorption at frequency $\omega_0$. This peak is analogous to the peak like feature seen in G(ω) in Fig 3.6. The peak, though, in G(ω) is broadened on both the high and low frequency side. The origin of the broadening in G(ω) on the high frequency side is due to the fact that the SIS junction is really an ensemble of two level systems each with a different $\omega_0$. Instead of a single resonant frequency, $\omega_0$, there is a threshold for absorption: $\hbar\omega_0>2\Delta-eV_0$. The broadening of G(ω) on the low frequency side has a different origin. It may be due to a number of factors such as a finite quasiparticle lifetime, gap anisotropy, or gap inhomogeneity. Variation in the gap parameter, Δ, would mean that the threshold condition will vary over the area of the junction.

$\sigma_2$ can be related to the susceptance, B(ω). Just as B(ω) in Fig. 3.7 has a bipolar nature, so does $\sigma_2$ in equation {3.31b}. The analogy can be carried further by noting that

in the low frequency limit, $\sigma_2$ is also proportional to frequency so that the capacitance per unit length, C', of solid can be defined to be,

$$C = \varepsilon \frac{\omega_p^2}{\omega_0^2}. \qquad \{3.32\}$$

This is analogous to the expression given for the tunnel junction capacitance given in equation {3.30} above. Note also that C' also decreases as $\omega_0$ increases, that is the system becomes less polarizable as the energy level spacing is increased.

## 3.4 Quantum Efficiency

In the previous Section we have described in detail the response of a tunnel junction to a time dependent sinusoidal voltage. In particular, equation {3.18} tell us that the magnitude of the induced *dc* current is proportion to $V_\omega{}^2$ which implies that the induced current is proportional to the incident power. Thus the SIS tunnel junction is a power or square law detector. Other more familiar types of square law detectors include crystal rectifiers, photoconductors, and photomultiplier tubes. For the later two devices, one typically defines a quantity called the quantum efficiency (QE) or more commonly the quantum yield. The QE is defined as the change in *dc* current per unit of power absorbed. For example, in a photoconductor, the QE is one electron per absorbed photon when the photon energy is greater than the bandgap of the semiconductor.

We can use the results of the previous Section for the induced *dc* current in equation {3.18} and the admittance from equations {3.27,28} to compute the QE($\omega$) of a SIS tunnel junction,

$$QE(\omega) = \frac{\Delta I_{dc}(\omega)}{\frac{1}{2}\mathrm{Re}\left(V_\omega^* I_\omega\right)}. \qquad \{3.33\}$$

As usual, $I_\omega = Y(\omega)V_\omega$. Substituting equations {3.18,27,28} into equation {3.33} results in,

$$QE(\omega) = \frac{e}{\hbar\omega}\left\{\frac{I_{dc}(V_0 + \hbar\omega / e) - 2I_{dc}(V_0) + I_{dc}(V_0 - \hbar\omega / e)}{I_{dc}(V_0 + \hbar\omega / e) - I_{dc}(V_0 - \hbar\omega / e)}\right\}$$

$$= \frac{1}{2}\frac{d^2 I_{dc} / dV_0^2}{dI_{dc} / dV_0}, \qquad \text{Classical Limit}$$

$$= \frac{e}{\hbar\omega}, \qquad \text{Quantum Limit.} \qquad \{3.34\}$$

When $I_{dc}$ varies slowly on a voltage scale compared to $\hbar\omega/e$ we obtain an expression for the QE which is identical to that found for a classical diode rectifier. However, at sufficiently high frequencies the conductance of a SIS tunnel junction varies so rapidly that

$$I_{dc}(V_0 + \hbar\omega / e) - I_{dc}(V_0) >> I_{dc}(V_0) - I_{dc}(V_0 - \hbar\omega / e). \qquad \{3.35\}$$

In this regime, the SIS detector approaches the quantum limit of one electron per absorbed photon. From Fig. 3.2(a) we see that the *dc* current varies on the voltage scale of 0.1mV which implies that for frequencies in excess of 25 GHz we are well into the quantum limit. For the experiments in this thesis, we will be probing the SIS junction in the 100GHz regime which means that all our experiments will be in the quantum regime.

## 3.5 Summary

In this Chapter we have seen that it is possible to calculate using Tucker theory the high frequency response of a tunnel junction by only measuring the *dc* I-V curve of the tunnel junction. In the next Chapter we will show experimental results which verify the Tucker theory.

## 3.6 References


[3.1] J. Bardeen, L. N. Cooper, J. R. Schrieffer, *Phys. Rev.* **108**, 1175 (1957).

[3.2] M. Tinkham, *Introduction to Superconductivity*. New York: McGraw-Hill, 1975.

[3.3] J. R. Schieffer, *Theory of Superconductivity*. New York: Addison-Wesley, 1964.

[3.4] T. Van Duzer and C. W. Turner, *Principles of Superconductive Devices and Circuits*. New York: Elsevier, 1981.

[3.5] H. Kamerlingh Onnes, *Comm. Phys. Lab Univ. Leiden, Nos.* 119, 120, 122 (1911).

[3.6] H. Frohlich, *Phys. Rev.* **79**, 845 (1950).

[3.7] L. N. Cooper, *Phys. Rev.* **104**, 1189 (1956).

[3.8] I. Giaever, *Phys. Rev. Lett.* **5**, 147,264 (1960)

[3.9] B. D. Josephson, *Phys. Rev. Lett.* **1**, 251 (1962).

[3.10] K.K. Likharev and V. K. Semenov, *IEEE Trans. Appl. Supercon.* **1**, 3 (1991).

[3.11] M. H. Cohen, L. M. Falicov, J. C. Phillips, *Phys. Rev. Lett.* **8**, 316 (1962).

[3.12] P. K. Tien and J. P. Gordon, *Phys. Rev.* **129**, 647 (1963).

[3.13] J. R. Tucker and M. J. Feldman, Rev. Mod. Phys. 57, 1055 (1985).

[3.14] N. R. Werthamer, *Phys. Rev.* **147**, 255 (1966).

[3.15] J. R. Tucker, *IEEE J. Quantum Electron.* **QE-15**, 1234 (1979).

[3.16] A. H. Worsham, N. G. Ugras, D. Winkler, D. E. Prober, N. R. Erickson, P.F. Goldsmith, *Phys. Rev. Lett.* **67**, 3034 (1991).

[3.17] J. M. Ziman, Principles of the Theory of Solids, Cambridge: University Press, 1964.

## 3.7 Figure Captions

Figure 3.1: Density of states at zero temperature in a superconducting-insulating-superconducting tunnel junction with gap $2\Delta$ in the presence of an applied bias, $V_0$. The states below $E_f$ are completely filled.

Figure 3.2: (a) Measured *dc* I-V curve in a 2 µm x 2 µm $Nb/AlO_x/Nb$ trilayer SIS tunnel junction. (b) $I_{kk}$ which is the Kramers-Kronig transform of the *dc* I-V curve in (a).

Figure 3.3: (a) Density of states in a superconducting-insulating-superconducting tunnel junction with gap $2\Delta$ in the presence of an applied *dc* bias, $V_0$, and a microwave signal frequency $\omega$. (b) The solid curve is *dc* I-V characteristic for an $Al$-$Al_2O_3$-$In$ tunnel junction. The dashed curve shows the appearance of photon-assisted tunneling steps when the junction is irradiated by microwave radiation at 38 GHz. 38 GHz corresponds to a photon energy of 0.16 mV which is the size of the photon steps.

Figure 3.4: A quasiparticle incident on a SIS tunnel barrier from the left at energy $E_i$ is scattered by the microwave field at frequency $\omega$, into a series of photonic sidebands separated by energy $\hbar\omega$ and weighted by the Bessel functions.

Figure 3.5: Graphical method for calculating the quantum conductance (solid line) and the classical conductance (dashed line) at a bias of 2.3 mV and frequency of 180 GHz. Note that the quantum conductance is much larger than the classical conductance.

Figure 3.6: Quantum conductance as a function of frequency for two different *dc* bias voltages, 2.6 mV and 2.3 mV. As the bias is lowered the peak in the conductance moves to higher frequencies.

Figure 3.7: Quantum susceptance as a function of frequency for two different *dc* bias voltages, 2.6 mV and 2.3 mV. The junction appears capacitive at low frequencies but becomes inductive at high frequencies.

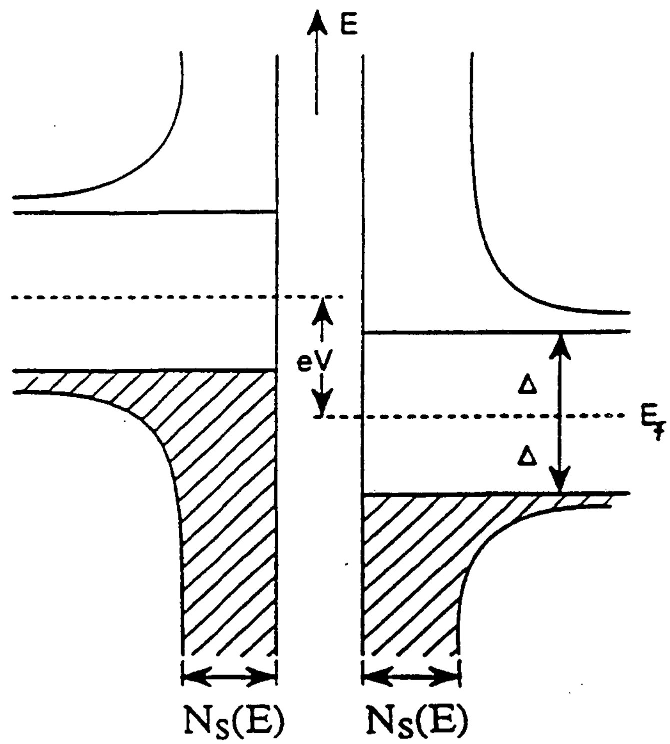


Figure 3.1

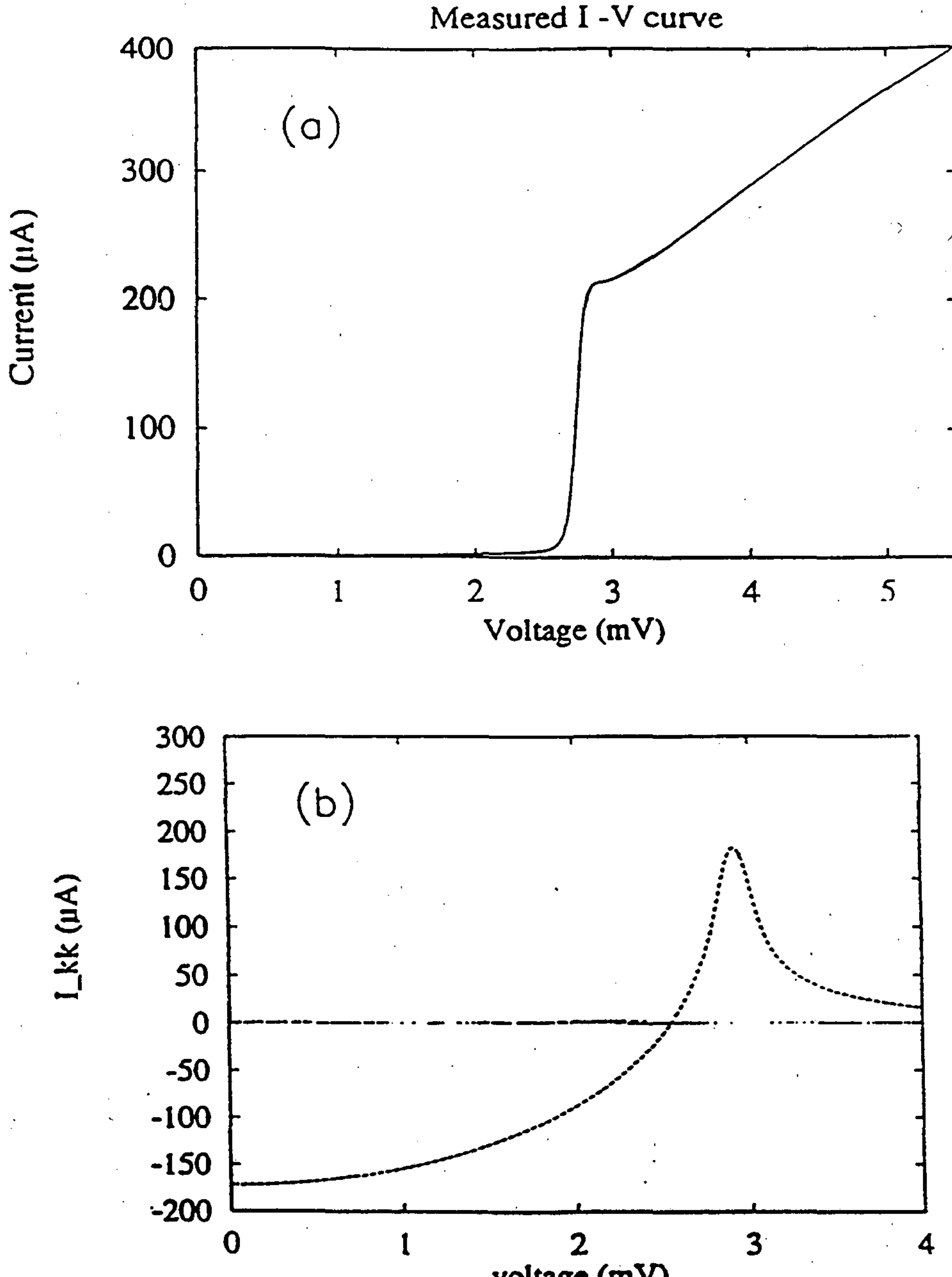


Figure 3.2

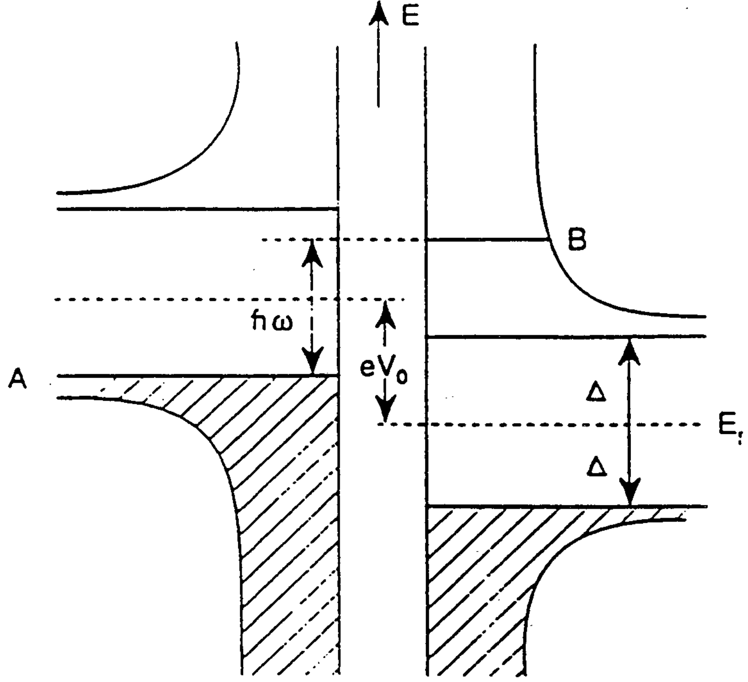


Figure 3.3(a)

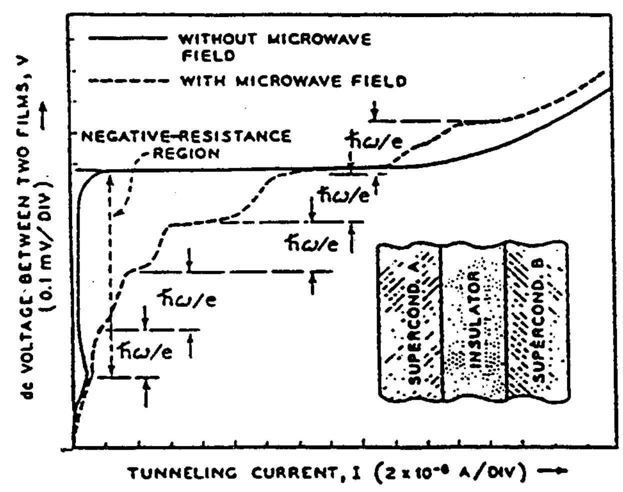


Figure 3.3(b)

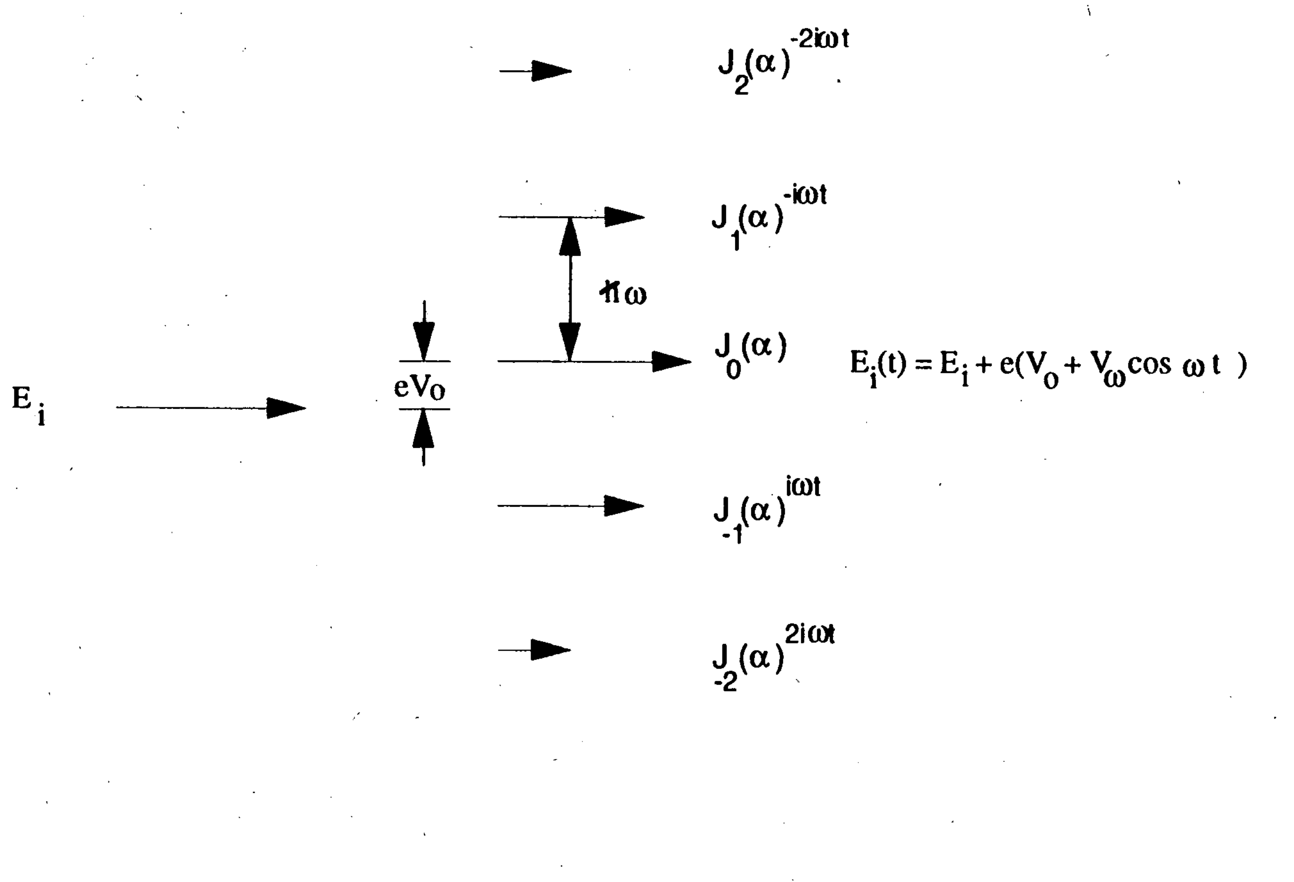


Figure 3.4

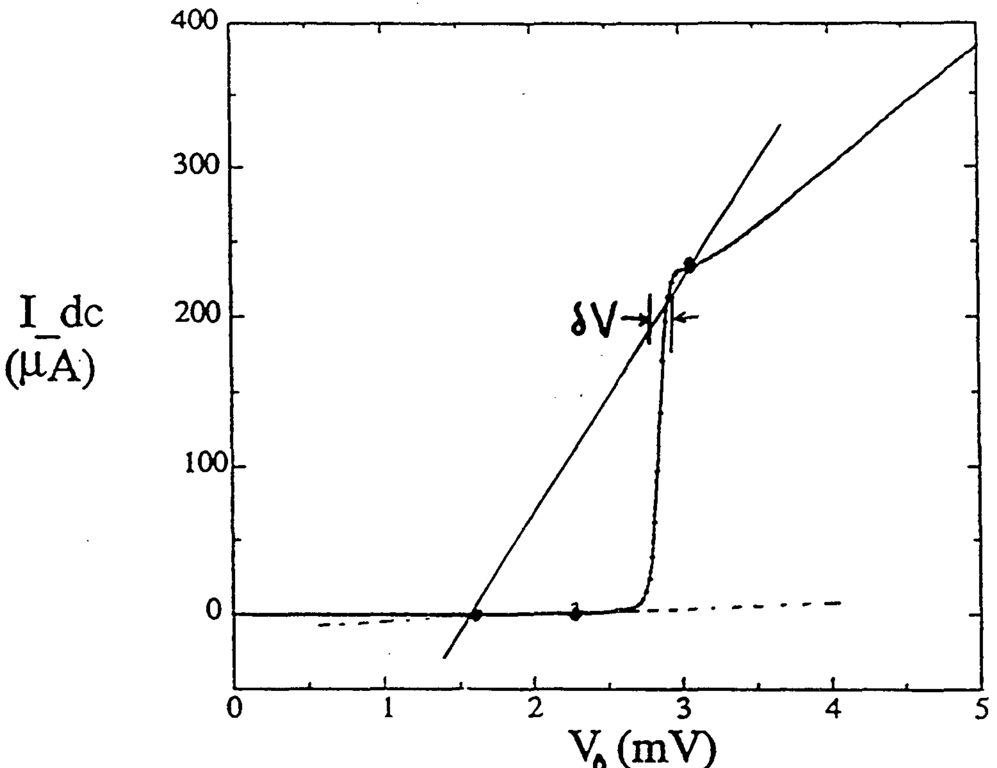


Figure 3.5

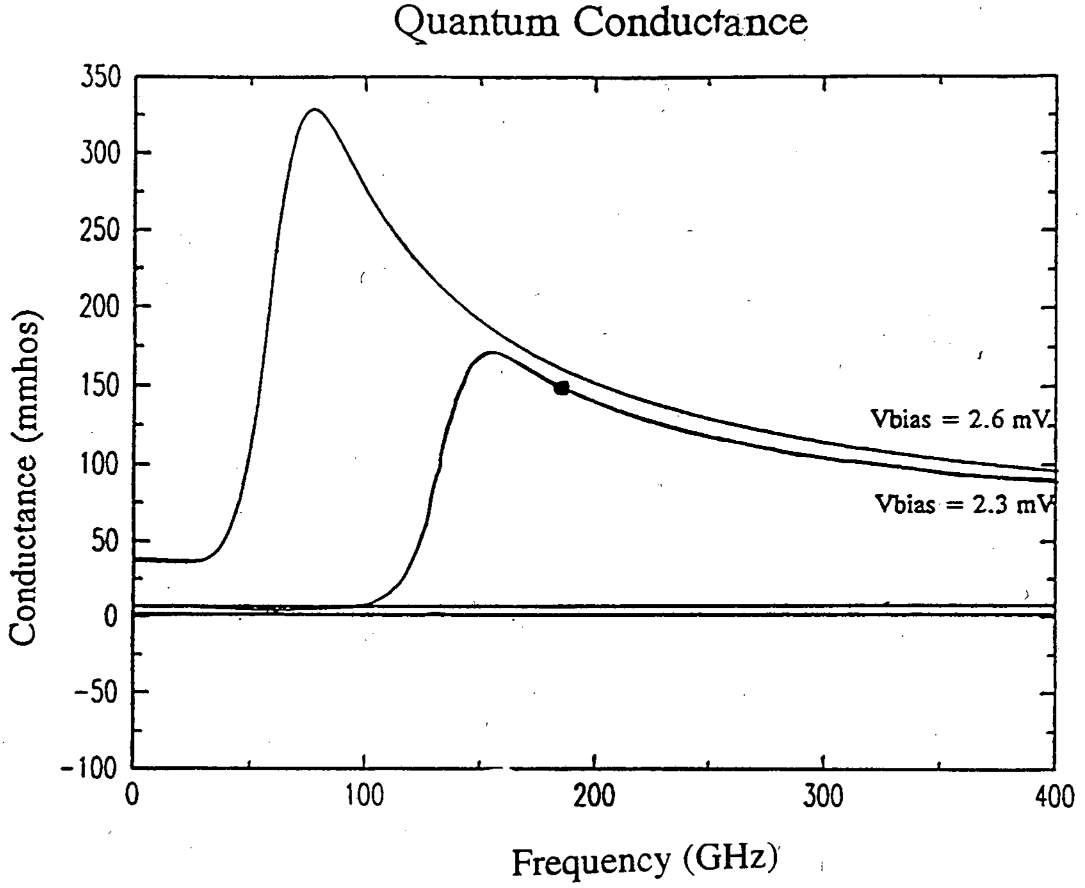


Figure 3.6

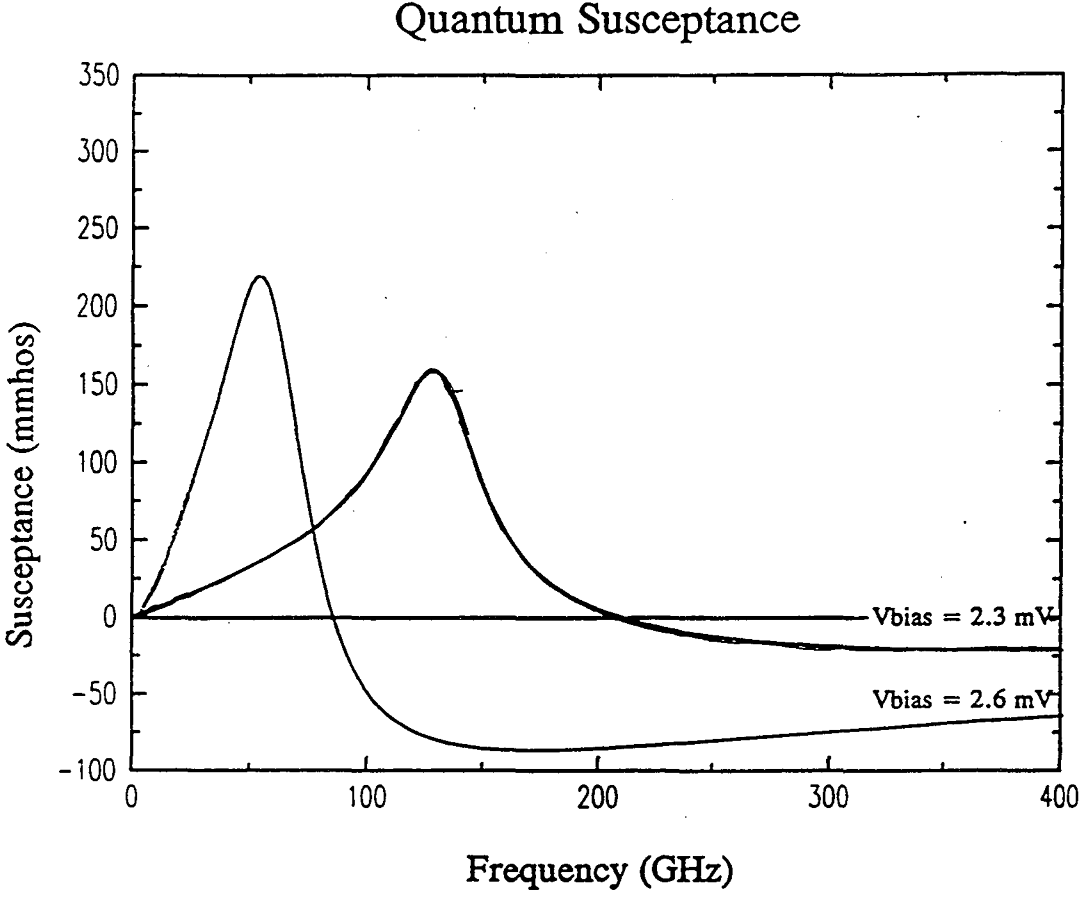


Figure 3.7

# Chapter 4

# High Frequency Response of a Superconducting Tunnel Junction: Experiment

In this Chapter we will describe the experimental measurement of the response of the quasiparticle current in a single Nb/$AlO_x$/Nb tunnel junction in the frequency range from 75-200 GHz [4.1]. This work is the result of a successful collaboration between Professor Joseph Orenstein's group and Dr. Simon Verghese and Dr. Carl A. Mears from Professor Paul Richards group. We have applied the THz-TDI technique described in detail in Chapter 2 to measure the linear admittance of a superconducting-insulating-superconducting (SIS) tunnel junction over a broad frequency scale. Picosecond pulses of millimeter wave radiation were generated by illuminating a photoconductive switch with a femtosecond mode-locked Ti-sapphire laser. The pulses are coupled quasioptically to the junction through a broadband log periodic planer lithographed antenna. The broadband response of the junction is inferred by monitoring changes in the *dc* current induced by

interfering two picosecond electrical pulses at the junction as a function of time delay between them. These data are found to be in complete agreement with the results described in Chapter 3 for the linear theory of photon-assisted tunneling. In addition, to describing our linear response data, we will also describe briefly some of our preliminary measurements of the nonlinear response.

## 4.1 Introduction

A sharp onset in the current-voltage (I-V) curve of an SIS junction occurs at a voltage $2\Delta/e$. The theoretical basis for this phenomena was discussed in Chapter 3 and shown explicitly for a Nb/AlO$_x$/Nb tunnel junction in Fig. 3.2(a). This nonlinearity in the quasiparticle current has been exploited in sensitive, high-frequency mixers and square-law detectors of millimeter wave radiation [4.2,4.3]. We have applied a new terahertz interferometric technique to make broadband measurements of the high frequency response of an SIS square law detector. These measurements are useful for applications such as understanding the ultimate operating speed of interconnections between optical fibers and superconducting tunnel junctions.

As discussed in Chapter 3, a rectified *dc* current, $\Delta I_{dc}(V_0)$, flows across a SIS junction when it is excited with a microwave signal at frequency $\omega$ and is biased at a voltage $V_0 \approx 2\Delta/e$. In the limit of low microwave power, the SIS junction operates as a square-law detector and $\Delta I_{dc}(V_0)$ is proportional to the quantum efficiency, $QE(\omega,V_0)$, of the detector and the amount of microwave power coupled to the junction (see equation {3.33}). With proper experimental design, the amount of power coupled to the junction can be made to sensitively depend on the admittance of the tunnel junction. According to a theory developed by Tucker [4.4], all the information required to predict $QE(\omega,V_0)$ (see equation {3.34}) is embodied in the ratio of the second and first finite difference of the *dc* I-V curve, where each difference is calculated with a finite voltage interval $\hbar\omega/e$. The quantum efficiency $QE(\omega,V_0)$ has two frequency regimes which are separated by a

crossover frequency of order $e\delta V/\hbar$, where $\delta V$ is the width of the onset of the *dc* I-V curve (see Fig. 3.5). In the low-frequency or classical regime, the first and second difference approach the first and second derivative of the *dc* I-V curve evaluated at $V_0$ and $QE(\omega,V_0)$ is independent of $\omega$. In the *quantum* regime, defined by $\omega > e\delta V/\hbar$, the $QE(\omega,V_0)$ is frequency dependent and exhibits a threshold near $(2\Delta - eV_0)/\hbar$. Similarly, Tucker also predicts the appearance of a frequency dependent quantum conductance, $G(\omega)$, in the quantum regime. The prescription for calculation of the quantum conductance is to take the first finite difference of the *dc* I-V curve (see equation {3.27}).

Considerable effort has been devoted to testing Tucker's theory experimentally, for essentially two reasons. First, the ability to characterize the microwave response of an SIS device by making relatively trivial *dc* transport measurements is economically advantageous. Second, the appearance of a frequency dependent quantum conductance implies via the Kramers-Kronig relations the appearance of a frequency dependent quantum susceptance (see equation {3.29}). The appearance of a quantum susceptance has typically been absent in the classical theory for SIS mixers. The quantum susceptance, $B(\omega)$, describes the out-of-phase component of the microwave current generated by the incident microwave voltage. In accordance with the general requirements imposed by causality, $B(\omega)$ becomes large near the onset of absorption at $(2\Delta - eV_0)/\hbar$. According to the theory, $B(\omega)$, can be large and of the same order of magnitude as $G(\omega)$.

Previous experiments using continuous-wave (CW) or narrow-band sources have generally confirmed the predictions of the Tucker theory. Hu *et al.* made the first measurements of the quantum susceptance in SIS tunnel junctions [4.5]. They used cavity perturbation techniques to infer the existence of the quantum susceptance. Using microlithographic techniques they fabricated a planer antenna and SIS junction in parallel with an inductive microstrip stub. The inductive stub and the geometrical capacitance of the junction formed a resonator. By using a Fourier-transform infrared spectrometer (FTIR), they were able to measure small 10% shifts in the resonant frequency as the bias voltage,

$V_0$, was changed. These variation in the resonant frequency could be directly attributed to changes in the quantum susceptance as the bias voltage was swept. Another method for extracting the susceptance was developed by Worsham *et al.* They used conventional phase sensitive microwave reflectometry techniques at 87 GHz on a pair of Nb/$AlO_x$/Nb tunnel junctions mounted at the end of a waveguide [4.6]. By knowing exactly the impedances of the network that the tunnel junctions were imbedded in, they were able to extract absolute numbers for the voltage dependent conductance and susceptance at 87 GHz.

These experiments, although important since they were the first to demonstrate the existence of the quantum susceptance, suffer from the significant drawback that the techniques are inherently narrow band. The experiment by Worsham *et al.* relies on the use of a Gunn oscillator which is a narrow band source with typically less than 5% tuning capability. In addition Gunn sources are only available at discrete frequencies making broadband measurements impossible. On the other hand, the FTIR technique developed by Hu *et al.* has the potential for broadband measurements. However, due to the low power of the lamp source, the experiments were restricted to the use of resonators. The use of the resonator boosted the signal strength near the resonant frequency making the experiments feasible. Unfortunately, the introduction of tuning structures also makes the method inherently narrow band. They were only able to monitor changes in the resonant frequency from 75 GHz to 85 GHz. Even though the resonator improved the signal strength, the overall signal to noise(S/N) still remained poor. In fact 5-10 spectra had to be co-added to obtain a sufficiently high S/N ratio [4.7] and most experimental runs took five to ten hours for a complete data set.

To overcome the limitations of the FTIR lamp source, we have developed a THz-TDI which has been described in detail in Chapter 2. Due to the high brightness of our picosecond sources, we have been able to characterize SIS devices over a broad frequency regime ranging from 75 to 200 GHz. By changing the antenna source, the frequency

regime could easily be extended to several THz. The data obtained with our system are the first broadband measurements of the quasiparticle response of an SIS junction. Overall, our results are consistent with the Tucker theory and demonstrate clearly the importance of B(ω) in determining the quasiparticle response.

## 4.2 SIS Terahertz Time Domain Interferometer

In Chapter 2 we have discussed in detail the characteristics of our picosecond sources and the basic theory behind the THz-TDI technique. Here we will not repeat all that information, but we will briefly summarize the experimental method and describe some of the experimental details which are specific to the SIS experiment.

A block diagram of the time-domain interferometer was given in Fig. 2.9. The key elements of the system are the sources of pulsed electric fields. Each source consists of a 50x50 μm square of ion-damaged silicon which bridges the terminals of a 300 μm dipole antenna. The sources were patterned on a silicon-on-sapphire wafer. Each antenna was *dc* biased between 10 to 20 volts. When the silicon is illuminated with a short optical pulse, a short pulse of photocurrent flows through the antenna terminals. The photocurrent is generated with optical pulses of duration 100 fs, repetition rate of 100 MHz, and average power of 100 mW from a Ti:sapphire laser operating at 800 nm. The photocurrent pulse drives the antenna to radiate a nearly single cycle electric field pulse into free space. As shown in Fig. 2.6(b), the pulse is incredibly broadband with a center frequency of 180 GHz and a FWHM bandwidth of 150 GHz. After generation, the pulses are immediately collimated by a 13 mm diameter sapphire hyperhemispherical lens. The sapphire was z-cut, which means that the optic axis of the sapphire lens was chosen to be perpendicular to the plane of the antenna [4.8]. After the lens, the pulse is fully collimated by a 9cm diameter f/1 parabolic mirror. The two beams are then combined with a 175μm thick Mylar beamsplitter. An f/3 parabolic mirror then focuses the combined beam through a 16mm diameter 25 μm thick polypropylene vacuum window on a small Infrared Labs

liquid helium cryostat which cools the junction. The thickness of the polypropylene window was chosen to be thin enough to eliminate Fabry-Perot effects. After passing through the vacuum window, the beam passes through a 12.7 mm diameter 0.83 mm thick fused quartz window with a 100μm thick black-poly film overlay. Cooled by a 77 K heat shield, this window absorbs radiation above the midinfrared, reducing the heat load on the pumped liquid He coldstage. We pump on the liquid helium to cool the junction down to 1.6 K. Although pumping on our liquid helium reduces the hold time of the cryostat from ten hours (unpumped helium) to five hours, this time is more than sufficient to carry out three to four experimental runs. The FTIR experiments by *Hu et al.* were restricted to measurements at 4.2 K (unpumped liquid helium temperatures) to allow for the lengthy measurement times [4.7]. The helium cryostat rests on a kinematic mount so that it can be replaced temporarily with a helium cooled bolometer for calibration experiments.

Our interferometer has the unusual property that when the spectrometer is properly aligned, the resulting interferogram is purely asymmetric, that is $\Delta I_{dc}(\tau) = -\Delta I_{dc}(-\tau)$. This is in contrast to the standard FTIR with a mylar beam splitter in which the interferograms are symmetric, $\Delta I_{dc}(\tau) = \Delta I_{dc}(-\tau)$. The unusual property of our spectrometer is due to the fact that one arm of our spectrometer interacts with the beamsplitter in reflection while the other arm of the spectrometer only sees the beam in transmission. Since the reflection and transmission coefficients of the beam splitter are frequency dependent, the beams from the two arms of the spectrometer are not identical after the beam splitter. Thus the interferogram does not have to be strictly symmetric. In a standard FTIR both beams see the beam splitter in reflection *and* in transmission. This means that beam from both arms or the interferometer will be identical which will lead to the standard result of a symmetric interferogram.

The unique properties of our interferogram can be understood from the simple mathematical argument given below. In Chapter 2 (equation {2.13}) we derived a general expression for the rectified current spectrum,

$$\Delta I_{dc}(\omega) = F[\Delta I_{dc}(\tau)]$$
$$= 2\pi A(\omega) I_1^*(\omega) I_2(\omega). \qquad \{4.1\}$$

Looking at a schematic of our interferometer in Fig 2.9, we see that $I_1(\omega)=t(\omega)I_{10}(\omega)$ and $I_2(\omega)=r(\omega)I_{20}(\omega)$, where $t(\omega)$ and $r(\omega)$ are the amplitude transmission and reflection coefficients respectively. Since both antennas were fabricated with identical processing, we assume that $I_{10}(\omega)=I_{10}(\omega)=I_0(\omega)$. In this case equation {4.1} can be rewritten as,

$$\Delta I_{dc}(\omega) = 2\pi A(\omega) |I_0(\omega)|^2 t^*(\omega) r(\omega). \qquad \{4.2\}$$

The beam splitter operates on the principle of a Fabry-Perot etalon and is designed to function between the zero and first order transmission peak. For a lossless dielectric beam splitter it can easily be shown using the equations for a Fabry-Perot etalon that the product, $t^*(\omega)r(\omega)$ is purely imaginary [4.9]. Since $A(\omega)$ is strictly real, $\Delta I_{dc}(\omega)$ is also imaginary. From the properties of the Fourier transform we know that if $\Delta I_{dc}(\tau)$ is real and $\Delta I_{dc}(\omega)$ is imaginary then $\Delta I_{dc}(\tau)$ must be an odd function of $\tau$, ie. $\Delta I_{dc}(\tau) = -\Delta I_{dc}(-\tau)$. Figure 4.1 shows a plot of the beam splitter efficiency $2\mathrm{Im}[rt^*]$ for a mylar beamsplitter of thickness 175 μm and index of refraction of 1.85 at millimeter wavelengths [4.10]. This beam splitter is useful over the frequency range from 50 to 450 GHz.

Before beginning experiments with the SIS tunnel junction, we performed a number of calibration tests with a composite bolometer operating at T=1.6 K. Since the SIS cryostat was mounted on a kinematic mount, it was a relatively simple operation to switch out the SIS junction for the bolometer without disturbing the alignment of the interferometer. The bolometer was specially designed for measurements at low microwave power levels. A Winston cone was used to maximize the coupling of power into the bolometer. In addition, a cooled low pass fluorogold filter with a cutoff frequency at 600GHz was used to block room temperature black body radiation from saturating the sensitive bolometer.

The experimental procedure for measuring an interferogram is as follows (see Fig. 2.9). First the *dc* voltage on each antenna is adjusted so that the power from each arm of the interferometer is identical. Next, *one* of the laser beams in the interferometer is mechanically chopped with a chopper wheel at 10 Hz. The synchronous signal is then picked up on the bolometer with a PAR 124A lock-in amplifier. Next a Klinger stepper stage is used as variable path delay to move a mirror a distance D. The delay is placed strategically in the optical portion of our interferometer. The distance change $\Delta D$ can easily be converted to a change in time delay $\Delta\tau$ by the equation, $\Delta\tau=2\Delta D/c$. We then monitor the bolometric signal as a function of D. Figure 4.2(a) shows a typical interferogram. Notice that the interferogram is asymmetric as expected. The point of asymmetry occurs at the position D=1550 μm which defines the condition $\tau=0$. The fact the interferogram is not perfectly asymmetric implies the spectrometer is not perfectly aligned or that the antennas are not absolutely identical. In our data analysis on the SIS junction, we always normalize our data which makes our experiments insensitive to small misalignments. Figure 4.2(b) is the amplitude of the Fourier transform of the interferogram in Fig 4.2(a). From equation {4.2}, it is clear that the Fourier transform is proportional to the power spectrum, $|I_0|^2$, of the incident pulses. The spectrum peaks at 180 GHz and has an approximate 3db bandwidth of 100 GHz. We can compare this spectrum in Fig. 4.2(b) to the spectrum in Fig. 2.6(b) which was measured using the terahertz time domain technique. The spectrum measured with the bolometer has more structure and has less bandwidth. This is most likely due to the filtering action of the Winston cone and the drop in beam splitter efficiency below 100 GHz. Nevertheless the spectrum is sufficiently broadband to make spectroscopic measurements on the SIS tunnel junction.

## 4.3 SIS Junction Fabrication

A cross Section of the SIS junction is shown schematically in Figure 4.3. The junction was fabricated at Conductus Inc. by A.T. Barfknecht using the Nb trilayer process

[4.11] which has been popularized for use in fabrication of digital Josephson Junction technology . The first step is to sputter a Nb base electrode on a four inch diameter silicon wafer. Next a thin aluminum film is deposited on the Nb and then the aluminum is oxidized to form the tunnel barrier. On top of the aluminum oxide, a second layer of Nb is added and anodized to define the junction area. A layer of $Si0_2$ is used for electrical isolation. Lastly a Nb *wire-up* layer is added which will form one terminal of the antenna. The second terminal of the antenna is formed by the base Nb electrode.

The SIS junction has an area of 2x2 μm and a normal state junction resistance, $R_N$, of 14 ohms. The *dc* I-V characteristics of the junction were given in Fig. 3.2(a). Since the junction also has a geometrical capacitance, C, of 200 fF, the SIS junction has a 3 dB corner frequency, $1/2\pi R_N C$ at only 60 GHz. This means that in our frequency range the current will be shunted by the geometrical capacitance. A magnetic field of approximately 100 G is used to cancel out the Josephson Cooper pair tunneling current so that our measurements will solely reflect the high frequency tunneling currents.

As discussed in Section 2.6.2, the coupling of microwave radiation to the SIS junction can be greatly enhanced by placing the junction at the feed of an antenna. This reduces the mismatch between the mm wave radiation and the 2x2 μm square junction. For the SIS experiments we use a circular tooth log-periodic antenna which is shown schematically in Figure 4.4. Both the central bow angle and the tooth angle is 45 degrees. The ratio of the adjacent linear teeth is two and the length of the smallest tooth is 50 μm. This antenna belongs to a special class of self complimentary antennas. Self complimentary means that the metalized and unmetalized portions of the antenna are identical. It has been shown that such an antenna made of lossless conductors and fabricated on a semi-infinite substrate will have the desirable property that the antenna admittance, $Y_A$, is frequency independent and depends only on the dielectric constant of the substrate [4.12]. The admittance is given by the expression,

$$Y_A = \frac{[(1+\varepsilon_r)/2]^{1/2}}{Z_0/2} \quad , \qquad \{4.3\}$$

where $\varepsilon_r$ is the relative dielectric constant of the substrate and $Z_0$ is the impedance of free space. With a dielectric constant of silicon equal to 11.9 at millimeter wavelengths [4.13], the antenna admittance is 1/75 Ω. Preliminary measurements by Nahum *et al.* [4.14] suggest that the beam pattern of a circular tooth log-periodic antenna maybe frequency dependent. This is most likely the result of the fact that adjacent teeth on log-periodic antenna are oriented roughly orthogonal with respect to each other. Different teeth will resonate at different frequencies which means that the polarization will flip flop as the frequency is varied.

## 4.4 Single Pulse Experiments

Before we consider the interferometric experiments, it is instructive to first look at the rectified photoresponse due to a single pulse. These experiments are important in choosing the proper regime to carry out the spectroscopic experiments. We need to choose an appropriate bias voltage range and microwave power level. In Chapters 2 and 3 (equations {2.8} and {3.18}) we have derived the following expression,

$$\Delta I_{dc}(\omega) = \frac{1}{4}\left[\frac{I_{dc}(V_0 + h\omega/e) - 2I_{dc}(V_0) + I_{dc}(V_0 - h\omega/e)}{(h\omega/e)^2}\right]\frac{I_A(\omega)I_A^*(\omega)}{|Y_A(\omega)+Y(\omega)|^2}, \{4.4\}$$

for the rectified current induced in a SIS tunnel junction of admittance Y(ω) by a microwave field at frequency ω. Here $Y_A(\omega)$ is the admittance of the antenna, $I_A(\omega)I_A^*(\omega)$ is proportional to the power spectrum of the incident pulses, and $I_{dc}(V_0)$ is the *dc* current that flows through the junction in response to a *dc* bias $V_0$. If we ignore the frequency dependence of Y(ω) and $Y_A(\omega)$, then the above expression predicts that the rectified response will have a threshold at $\hbar\omega > |2\Delta - eV_0|$. Equation {4.4} is only valid in the regime of low microwave power levels defined by the condition, $eV_\omega/\hbar\omega << 1$ where $V_\omega$

is the voltage induced across the tunnel junction. This is often referred to as the regime of linear response. If the microwave power level is too high and $eV_\omega/\hbar\omega$ approaches unity, we will enter the regime of nonlinear response where multiphoton processes will dominate the rectified current.

We use the following experimental procedure for measuring the rectified current. First we chop the visible laser beam incident on photoconductive switch #2 in Fig. 2.9 at 1 KHz with a mechanical chopper and bias the antenna with a variable voltage source so we can adjust the strength of the microwave pulses on the SIS junction. The microwave pulses induces a small synchronous rectified current in the junction. This current is amplified with a room temperature low noise field effect transistor (FET) amplifier with a spot noise referred to the SIS junction of 0.2 $nV/Hz^{1/2}$ at 1KHz. A PAR 124A lock-in is then used to detect the synchronous signal. The use of an ultra low noise FET amplifier is critical to this experiment since relatively low microwave power levels are necessary to stay in the regime of linear response.

Figure 4.5 shows the results of a measurement of the rectified current induced in a SIS tunnel junction as a function of bias voltage at two different photoconductive antenna voltage levels, $V_{pc}$. The *dc* I-V curve is also superimposed on this plot for comparison. Recall from Chapter 2 that the power emitted by the Terahertz sources is proportional to $V_{pc}^2$ . Thus by changing the antenna voltage from 20 V to 60 V, the microwave power level incident on the junction is increased by a factor nine. Let us begin by considering the rectified current at the lower microwave power level (dotted curve in Fig. 4.5). This signal has many interesting features some of which are easily understood and others that must be left for future investigations. For a bias voltage, $V_0$, less than 1.5 mV the signal is immeasurably small. This is due to the fact that our pulse has very little spectral weight above the requisite frequency of $300GHz \approx (2\Delta - eV_0) / h$. As the bias voltage increases, the rectified current increases as expected since the threshold for photon absorption moves to lower frequencies where our pulse has greater spectral weight. The rectified current

peaks at a bias of 2.5 mV which corresponds to a threshold frequency of 60 GHz. One might naively expected that the peak in the rectified current at 60 GHz should match the peak in the spectrum in the pulse. Experimentally, though, we find that the pulse spectrum peaks at 180 GHz. The peak in the rectified current would only match the peak in pulse spectrum if the SIS junction acted as a single frequency resonant detector. Then the shape of the rectified current versus bias voltage would just be a reversed image of the pulse's spectrum. In reality, though, the SIS junction is a threshold detector, so the rectified current will more naturally reflect the integral of the pulse's spectrum. This integral will have a maximum value when threshold moves below the lowest frequency in the spectrum. From Fig. 4.2(b), 60 GHz is in fact near the low end of the pulse's spectrum.

As the bias is increased further, the rectified current is eventually reduced and finally goes negative when $V_0>2\Delta$. The negative response is due to stimulated emission of photons. As can be seen from Fig. 3.3(a), when $V_0>2\Delta$ quasiparticles can easily tunnel from the right to the left side of the barrier. When the quasiparticles are stimulated to relax by emitting a photon, there will be no states to tunnel into and there will be a corresponding decrease in the current or equivalently a negative rectified current. As the bias is increased further, a sharp negative peak is formed at $V_0$=2.85 mV and then eventually the rectified current returns to zero. The fact the a negative going peak in the rectified current is much sharper than the positive going peak is currently not understood. One hypothesis is that at that bias voltage, the bias dependent intrinsic admittance of tunnel junction exactly cancels the geometrical capacitance of the junction allowing for resonant absorption of power into the tunnel junction.

Now let us consider the case of the higher microwave power level with an antenna voltage of 60 V (solid curve) and compare it to the lower power signal. In order to simplify the comparison, we have multiplied the lower power signal by a factor of nine. In the regime of linear response for the tunnel junction, the rectified current should be proportional to $V_{pc}^2$, ie. linear in the incident power. Thus the signal at $V_{pc}$=60 V should

be nine times greater than that for the rectified current at $V_{pc}$=20 V, hence the dotted and dashed curves should perfectly overlap. There is reasonable overlap for 2.3 mV<$V_0$<2.7 mV which indicates that we are in the regime of linear response for these bias voltages. At lower bias voltages, however, excess rectified current flows through the tunnel junction. At $V_0$=2 mV there is twice as much signal as would be expected from a $V_{pc}^2$ dependence of the rectified current.

The excess current at low bias voltages most likely results from nonlinear multiphoton processes. To investigate this further, we have made measurements of the rectified current as function of $V_{pc}$ for two different tunnel junction bias voltages. These data are shown in Figure 4.6. First consider the dashed curve which is for a tunnel junction bias of 2.3mV. This dashed curve follows relatively closely the upper solid curve which has a $V_{pc}^2$ dependence thus we can assume that we are in the regime of linear response. However, at $V_0$=2.0 mV (dotted curve), the situation is dramatically different. Here the rectified current resembles more closely the $V_{pc}^3$ dependence of the lower solid curve. This is indicative of a multiphoton process. For the case of pure two photon absorption, the rectified current should scale as $V_{pc}^4$. The fact that we are not seeing the full $V_{pc}^4$ dependence is probably because we are in a cross over regime where both one photon and two photon processes are important. Since our pulse is extremely broadband, the different Fourier components may be in different regimes of linear and nonlinear response. We will show later how it is possible with interferometry to separate the signal due two photon processes from the signal due to one photon processes. Such measurements may prove useful in measuring the quasiparticle lifetime.

## 4.5 Linear Response: THz-TDI

The single pulse experiments described in the previous Section has given us a glimpse of the rich parameter space in which to carry out experiments on the SIS tunnel junction. By changing the power level we can probe the crossover between linear and

nonlinear response and by changing the tunnel junction bias we can probe both photon absorption and stimulated emission. Obviously this parameter space is extremely large, so it is crucial to be selective in choosing the first series of experiments. Fortunately, since we are the first to develop a technique to do broadband spectroscopy, we could begin with the simplest experiment: Probing the linear response of photon absorption for an SIS tunnel junction.

From the results of the single pulse experiments in Figs. 4.5 and 4.6, we decided to probe the junction in the bias regime from 2.1 mV to 2.5 mV and keep the photoconductive antenna voltage below 15 V. This will insure that our experiments will remain in the regime of linear response. The technique we use to measure interferograms with the SIS tunnel junction is in many respects identical to that used in measuring interferograms with the bolometer. There are only two important differences. First we chop the laser beam at 1 KHz and second we average two interferograms each of which takes eight minutes to record. Averaging is used to reduce noise due to laser fluctuations. Figure 4.7(a) shows the average rectified current as a function of time delay at five different bias voltages between 2.1 mV and 2.5 mV. The curves at different bias voltages have been offset for clarity. The interferograms are asymmetric about the null position at zero time delay as expected from the discussion in Section 4.2. Figure 4.7(b) shows the amplitude of the Fourier transforms of the interferograms in Fig. 4.7(a). As the bias is lowered from 2.5mV to 2.1mV, the threshold frequency, $(2\Delta - eV_0)/h$, moves to higher frequency. This increase in the threshold frequency is reflected in the spectra by inducing an increasing suppression of the low frequency response relative to the high frequency response. The structure seen in the spectra are most likely the result of interference effects in coupling the electrical pulses through our system and onto the log periodic antenna in the cryostat.

The first step in our analysis is the normalization of the spectra in order to divide out the bias-independent term, $I_A(\omega)I_A^*(\omega)$, which is proportional to the power spectrum of

the incident pulses. Figure 4.8 (symbol curves) shows the spectra in Fig. 4.7(b) divided by the spectrum at $V_0$=2.5 mV. Most of the structure in the spectra in Fig. 4.7(b) are removed by the normalization, indicating that they are related to the spectrum of the incident power and are not intrinsic to the junction itself. The normalized spectra show a gradual onset at $(2\Delta\text{-}eV_0)/h$, indicating the threshold for photon-assisted tunneling. In addition, the curves shift systematically to the right in steps of approximately 25 GHz. This correlates well with the step changes in the *dc* bias on the junction of 0.1 mV (recall 1 mV=240 GHz).

As discussed extensively in Chapter 3, the Tucker theory provides a prescription for predicting the spectral response (equation {4.4}) of the junction from a measurement of the *dc* I-V curve. It is apparent, though, from equation {4.4} that we are also required to know the antenna admittance. As discussed in Section 4.3, the log periodic antenna used in our experiment was designed to have a constant, real admittance over the frequency range of the measurement. To minimize the effect of any possible variation in $Y_A(\omega)$ on the shape of the spectra, the design admittance of the antenna was chosen to be much smaller than the junction admittance. The junction admittance $Y(\omega)$ consists of two parallel components, the intrinsic admittance of the junction calculated in Chapter 3 from the Tucker theory and an extrinsic admittance due to the 200 fF geometrical capacitance of the junction. At 120 GHz, the admittance of the geometrical capacitance of 151 mmhos is much greater than the antenna admittance of 13mmhos which means that most of the microwave currents will be shunted through the junction. In this limit, from equation {4.4}, $\Delta I_{dc}$ will be directly related to the quantity we would like to measure, $1/|Y(\omega)|^2$ or equivalently $|Z(\omega)|^2$ where $Z(\omega)$ is the impedance of the tunnel junction.

In order to stress the importance of including the quantum susceptance in $Y(\omega)$, we first calculated the response of our junction with the quantum susceptance omitted from the calculation of $\Delta I_{dc}$. This calculation is shown as the dashed curves in Figure 4.8. The difference between the data and the dashed lines shows dramatically the significance of the

quantum susceptance in determining the microwave response of the SIS junction. Without the quantum susceptance, the onset is considerably sharper than is observed experimentally. The smearing of the experimentally observed threshold is the direct result of the quantum susceptance modifying the coupling of power to the junction. From Fig. 3.7, we also see that the quantum susceptance is of order 100 mmhos which is comparable to the susceptance of the geometrical capacitance of 150 mmhos at 120 GHz. Thus both the data and the calculations tell us that we cannot ignore the quantum susceptance.

Now let us calculate the response of the junction including the full Tucker theory with the quantum susceptance. The solid lines in Fig. 4.8 show the results of this calculation using the *dc* I-V curves measured at T=1.6 K as input, with no fitting parameters. The calculated lines are in remarkable agreement with the data for $2.1mV \leq V_0 \leq 2.3mV$ . The data for $V_0$=2.4 mV fall slightly below the theoretical curve. For frequencies less 170 GHz, the structure in the ratios is reproducible and may arise from interference effects in the interferometer. For frequencies greater than 170 GHz, the signal is small and amplifier noise contributes to the structure in the ratios.

In summary, we have presented the first broadband measurements of the microwave response of an SIS junction. We observe clearly the onset of photon assisted tunneling at $(2\Delta\text{-}eV_0)/h$. The results are in excellent agreement with Tucker theory with zero fitting parameters. In addition, the effects of the frequency dependent quantum susceptance appear dramatically in our data and cannot be ignored in computing the microwave response. Finally, the success of the SIS experiment is proof that the THz-TDI technique is applicable to probing any micron or nanometer scale device that exhibits a nonlinearity in the *dc* I-V curve.

## 4.6 Nonlinear Spectroscopy - Preliminary Experiments

In the previous Section we presented measurements in the time domain of the linear response of the quasiparticle current to a picosecond pulse. In principle, since we are only

probing the linear response, there is no extra information gained in making measurements in the time domain versus frequency domain. For example, if a tunable CW source were available, then we could simply measure $\Delta I_{dc}$ as a function of frequency directly and obtain the same data as in Fig. 4.8. In the laboratory, though, experiments with CW sources are plagued by difficulties due to formation of large standing waves. These effects may sometimes be minimized by averaging over the frequency spectrum. In any case, the linear spectroscopy experiments do not take advantage of the ultrashort temporal profile of our picosecond pulses except for the fact that the pulses are extremely broadband.

Short pulses are especially well suited for nonlinear experiments as compared to CW sources. A short pulse can provide both a high peak power which is necessary for a nonlinear experiment and also provide a low average power so as not to melt the sample. Our system has a duty factor of 1000 which means that our peak power is 1000 times greater than the average power. In this Section we will describe how large amplitude picosecond pulses can be applied to measuring the quasiparticle lifetime.

There are a number of time scales which appear in the dynamics of quasiparticle excitations. Consider the case of a photon with energy $\hbar\omega > 2\Delta - eV_0$ which generates a quasiparticle excitation. According to the theory developed by Cohen, Falicov, and Phillips [4.15], if the photon is absorbed, the quasiparticle oscillates across the junction at a frequency $\omega/2\pi$ forever. The infinite lifetime is manifest in the sharp discontinuity in the superconducting density of states. In this theory, the current produced by a delta function voltage pulse only decays because the many quasiparticles generated each oscillate with a slightly different frequency. This current decay is extremely slow and goes like $1/T$ [4.16] where T is the time after the delta function voltage pulse. However, if the junction is inhomogeneously broadened due to a variation of the gap function across the junction, then the quasiparticles will dephase with respect to each other in a time, $T_2$. Although the current has gone to zero, the quasiparticles are still excited. These excited quasiparticles will first thermalize with each other by emitting phonons and eventually they will scatter to

the superconducting band edge in a time $T_t$. Once at the band edge, one quasiparticle may scatter with another quasiparticle of opposite spin and momentum, and emit a phonon of energy $2\Delta$. These processes will eventually relax the system to the BCS ground state in time $T_r$, the quasiparticle recombination lifetime. Both $T_t$ and $T_r$ will depend on the temperature of the superconductor and on the density of quasiparticles. Dynes *et al.* were able to extract quasiparticle lifetime information from the *dc* I-V curve of a Pb:Bi alloy tunnel junction [4.17]. Their technique, though, only works with a small class of SIS junctions. They require an SIS junction with an extremely sharp onset in the *dc* I-V curve at $2\Delta$, such that the intrinsic broadening due to inhomogeneous effects is less than the broadening due to the finite quasiparticle lifetime. They measure the smearing in the *dc* I-V curve onset and attribute the smearing to a quasiparticle lifetime. Nonlinear spectroscopic measurements are more general than the *dc* technique and are especially well suited to tunnel junctions with inhomogeneous broadening greater than lifetime broadening.

Let us begin our discussion of the data by looking at a typical nonlinear interferogram in Figure 4.9. This interferogram was taking with the identical technique used in the previous Section, with the only difference that our power levels are now much higher. For Fig. 4.9, the voltage on the photoconductive antenna is 60 V as compared to a voltage of 15V for the linear spectroscopy measurements. In addition, the junction is biased at $V_0$=1.35 mV. We notice immediately two significant differences between the nonlinear interferogram and the linear interferograms in Fig. 4.7(a). The nonlinear interferogram is rectified, that it goes more positive than negative, and the interferogram is symmetric (cosine symmetry).

To understand these observations, let us begin with the phenomenological expression for $\Delta I_{dc}$ in the nonlinear regime at a fixed frequency,

$$\Delta I_{dc} = A|V|^2 + B|V|^4. \qquad \{4.5\}$$

We have omitted the term proportional to $|V|^3$ since this term cannot mix a high frequency microwave signal to *dc*. Let us first consider the rectification of the interferogram. If our signal in Fig. 4.9 is completely due to the second term above, then the ratio of the peak signal to the background should be 16 to 1 (remember that we only chop one arm of the interferometer). The first term above will only lead to a peak to background ratio of 4 to 1. The fact that we observe a peak to background ratio of 12 to 1 indicates that a significant component of our signal is due to second term in {4.5} above.

The cosine symmetry of the nonlinear interferogram can also be understood from equation {4.5}. Let us begin with a review of the origin of the sine (asymmetric) symmetry of the linear interferograms. We can replace V by,

$$V = t_B V_1 + r_B V_2 e^{j\omega\tau}, \qquad \{4.6\}$$

where $t_B$ and $r_B$ are the transmission and reflection coefficients of the beam splitter in Fig. 2.9, $V_1$ and $V_2$ are proportional to the electric field pulses from the photoconductive antennas, and $\tau$ is the time delay between the pulses. The first term in {4.5} can be rewritten as,

$$A|V|^2 = A\left[|t_B|^2|V_1|^2 + |r_B|^2|V_2|^2 + 2V_1V_2|t_B r_B^*|\sin(\omega\tau)\right]. \qquad \{4.7\}$$

In computing the above expression, we have used the fact that $t_B r_B^*$ is purely imaginary. The last term in {4.7} above shows explicitly the appearance of a sine symmetry in the interferogram. The second nonlinear term in {4.5} above can be rewritten as the sum of four terms,

$$\begin{aligned} B|V|^4 = {} & B\left[|t_B|^2|V_1|^2 + |r_B|^2|V_2|^2\right]^2 + \\ & 2B|t_B r_B^*|^2|V_1|^2|V_2|^2 - \\ & 2B\cos(2\omega\tau)|t_B r_B^*|^2|V_1|^2|V_2|^2 + \\ & 2B\sin(\omega\tau)|t_B r_B^*|V_1V_2\left[|t_B|^2|V_1|^2 + |r_B|^2|V_2|^2\right]. \end{aligned} \qquad \{4.8\}$$

The first two terms are uninteresting since they do not depend on the time delay, $\tau$. The third term shows explicitly the appearance of a term with cosine symmetry which must be the dominant term in nonlinear interferogram in Fig. 4.9. This term in optics is often called the interferometric pump-probe term since it depends on the product of the intensity in the two beams [4.18]. In our experiment the pump and probe are of similar magnitude. The fourth term still retains the odd symmetry of the linear interferogram. It depends on the intensity of one beam and the interference product of beam one with beam two. In optics this is called the four wave mixing term [4.18]. The above calculation gives a simple prescription for extracting the pump-probe term from the other terms in the spectra. We can simply separate the interferogram into even and odd components via the sine and cosine Fourier transforms. The resulting even interferogram will be due strictly to the nonlinear pump-probe term while the odd term will contain contributions from the linear response and the four wave mixing signal.

Let us now discuss how the linear and nonlinear experiments can give us information about the dynamic processes appearing in the junction. The linear spectroscopic measurements can only measure a coherence time $T_c$ which is given by the equation,

$$\frac{1}{T_c} = \frac{1}{T_2} + \frac{1}{T_t} + \frac{1}{T_r}. \qquad \{4.9\}$$

It is clear from the above expression that $T_c$ will be dominated by the shortest time scale in the problem. If the system is strongly inhomogeneously broadened, then $T_2$ will be short and $T_c$ will effectively only measure $T_2$ and be insensitive to the thermalization and recombination lifetimes, $T_t$ and $T_r$ respectively. This problem also plagues the *dc* transport experiments by Dynes *et al.* [4.17] described at the beginning of this Section. If the tunnel junction is heavily inhomogeneously broadened, then the smearing of the I-V curve onset will only measure $T_2$. In this limit, no information can be gained about the quasiparticle lifetimes from the *dc* transport data. In sharp contrast, the nonlinear pump-probe signal is a

direct measure of the quasiparticle lifetime. Consider once again the pump-probe term in equation {4.8} above. The physical interpretation of this term is the following. The first pulse injected into the tunnel junction will generate a large number quasiparticles. This large change in the distribution of quasiparticles will greatly change the mixing properties of the tunnel junction. The second pulse will then probe the modified tunnel junction. By varying the time delay between the pump and the probe a nonlinear interferogram can be measured. The width of the nonlinear interferogram will be related to quasiparticle lifetime. Since our pump and probe beam are of equal intensity, the nonlinear interferogram should be symmetric. In addition the interferogram will have interference fringes. In optics the fringes can be removed by using pump and probe beams of opposite polarizations. Unfortunately, since we couple to the junction with an antenna, the antenna terminals will always apply a field in a fixed direction, irrespective of the direction of the incident microwave field polarization. Thus, it is not possible to remove the fringe pattern.

Figure 4.10 shows preliminary data for the odd and even parts of the interferograms. These data were collected at various microwave power levels with the SIS junction at T=1.6 K. The incident microwave power levels were calibrated with a bolometer. The curves in Fig. 4.10 have been offset for clarity. These data have not been analyzed in detail and are meant only to demonstrate our ability to carry out nonlinear experiments. Nevertheless, some preliminary comments are appropriate. First consider the odd symmetry interferograms. These interferograms are roughly proportional to the microwave power and their shape does not change significantly. If we assume that the effect of increasing the microwave power is to increase the density of excited quasiparticles, then apparently $T_c$ is independent of number of quasiparticles. This would be consistent with the interpretation that the SIS junction is strongly inhomogeneously broadened and $T_c$ is dominated by the dephasing time $T_2$. The inhomogeneous broadening is expected to be independent of quasiparticle number. On the other hand, the even interferograms change in both shape and magnitude as the microwave power increased

above 4.6 μW. These changes in the interferogram may represent changes in the quasiparticle lifetime due to a higher density of excited carriers. Unfortunately, our pulse width is of order the width of the even interferogram, which makes it difficult to extract lifetime information. In future experiments, shorter 2 ps pulses may be used to more easily extract the quasiparticle lifetime.

In summary, we have shown that we have sufficient pulsed power in the terahertz regime to make nonlinear spectroscopic measurements. Such measurements are ideally suited to measuring the quasiparticle lifetime, which cannot in general be found from *dc* transport measurements. In addition, we are the first group to show that it is possible to do nonlinear experiments with terahertz pulses generated from a high repetition rate unamplified Ti-sapphire laser. The high repetition rate gives us excellent signal to noise characteristics as compared to a amplified Ti-sapphire system [4.19].

## 4.7 Summary

In this Chapter, we describe in detail the measurements of the linear response of the quasiparticle current in a Nb/$AlO_x$/Nb junction from 75-200 GHz. Our results confirm dramatically the importance of the quantum susceptance in determining the linear response. Our results are in full agreement with the linear theory for photon assisted tunneling. In addition we have described preliminary nonlinear spectroscopic measurements that may prove useful in the future for measuring the quasiparticle lifetime.

## 4.8 References


[4.1] S. Verghese, C. Karadi, C. A. Mears, J. Orenstein, P. L. Richards, and A. T. Barfknecht, Appl. Phys. Lett. 64, 915 (1994).

[4.2] P. L. Richards and Q. Hu, *Proc. IEEE* **60**, 1233 (1989).

[4.3] T. H. Buttgenbach, H. G. LeDuc, P.D. Maker, and T. G. Phillips, *IEEE Trans. Appl. Supercond.* **2**, 165 (1992).

[4.4] See reference [3.13].

[4.5] Q. Hu, C. A. Mears, P. L. Richards, F. L. Lloyd, *Phys. Rev. Lett.* **64**, 2945 (1990).

[4.6] A. H. Worsham, N. G. Ugras, D. Winkler, D. E. Prober, N. R. Erikson, P. F. Goldsmith, *Phys. Rev. Lett.* **67**, 3034 (1991).

[4.7] C. A. Mears, Ph.D. Thesis, University of California at Berkeley, 1991.

[4.8] Supplier : Wolf-Engineering in southern California, 714-646-1754.

[4.9] A. Yariv, Optical Electronics-Third Edition, New York: CBS College Publishing, 1985.

[4.10] Chapter2, ref [2.1].

[4.11] M. Gurvitch, M. A. Washington, H. A. Huggins, *Appl. Phys. Lett.* **42**, 472 (1983).

[4.12] P. H. Siegel, *IEEE Trans. Microwave Theory Tech.* **MTT-S Digest**, 6494 (1986).

[4.13] M. N. Afsar, *IEEE Trans. Microwave Theory Tech.* **MTT-32**, 1598 (1984).

[4.14] M. N. Nahum, P.L. Richards, M. Gaidis, D. E. Prober, *Proc. SPIE 1292 IR and MMW Conference Digest,* 278 (1992).

[4.15] See [3.11].

[4.16] R. E. Harris, *Phys. Rev. B* 11, 3329 (1975).

[4.17] R. C. Dynes, V. Narayanamurti, J. P. Garno, *Phys. Rev. Lett.* 41, 1509 (1978).

[4.18] Y. R. Shen, The Principles of Nonlinear Optics, New York: John Wiley & Sons, 1984.

[4.19] R. R. Jones, D. You, P. H. Bucksbaum, *Phys. Rev. Lett* **70**, 1236 (1993).

## 4.9 Figure Captions

Figure 4.1: Beam splitter efficiency $2\text{Im}[r_B t_B^*]$ plotted versus frequency for a 175 μm mylar beamsplitter.

Figure 4.2: Measurement of an interferogram using the interferometer in Fig. 2.9 in which the bolometer is used as the detector. (a) Bolometric interferogram measured as a function of mirror delay line position. The interferogram has odd symmetry about the mirror position of 1550 μm. (b) Amplitude of the Fourier transform of the interferogram in (a). The spectrum has useful bandwidth from 100 to 220 GHz.

Figure 4.3: Cross Section diagram of the $Nb/AlO_x/Nb$ tunnel junction fabricated at Conductus, Inc. The junction has a cross Sectional area of two square microns.

Figure 4.4: Circular toothed log periodic antenna.

Figure 4.5: Measurement of the rectified current, $\Delta I_{dc}$, in the presence of a single picosecond pulse as a function of bias, $V_0$. The dotted curve shows $\Delta I_{dc}$ when the photoconductive antenna is biased at 20 V while the solid curve corresponds to a antenna bias of 60 V. The low power curve has been multiplied by a factor of nine to ease comparison to the high power data. The excess $\Delta I_{dc}$ flowing at 1.5 mV at the higher power level is an indication of multiphoton processes. Also shown is the *dc* I-V curve of the tunnel junction.

Figure 4.6: $\Delta I_{dc}$ measured at two junction bias voltages versus antenna voltage, $V_{pc}$, which is proportional to the incident electric field on the junction. The dashed curve is at a bias of 2.3 mV while the dotted curve is at a bias of 2.0 mV. In the regime of linear response $\Delta I_{dc}$ should scale as $V_{pc}^2$.

Figure 4.7: (a) Shift in the *dc* quasiparticle current $\Delta I_{dc}$ generated by two pulses of millimeter radiation plotted as a function of time delay between the pulses. (b) Amplitude of the Fourier transforms of the data in (a).

Figure 4.8: The symbols are ratios of the spectra shown in Fig. 4.7a to the spectrum measured with $V_0$=2.5 mV. Solid lines show calculations from the linear theory of photon assisted tunneling. Dashed lines show theoretical predictions with the quantum susceptance omitted.

Figure 4.9: Shift in the *dc* quasiparticle current $\Delta I_{dc}$ generated by two pulses of millimeter radiation plotted as a function of time delay between the pulses of high intensity. The interferogram is rectified, indicating the presence of multiphoton processes.

Figure 4.10: (a) Odd part of the interferogram measured at a bias $V_0$=2.4 mV for low and high pulsed power levels. (b) Even part of the interferogram measured at a bias $V_0$=2.4 mV for low and high pulsed power levels. These data may give information relating to the quasiparticle lifetime.

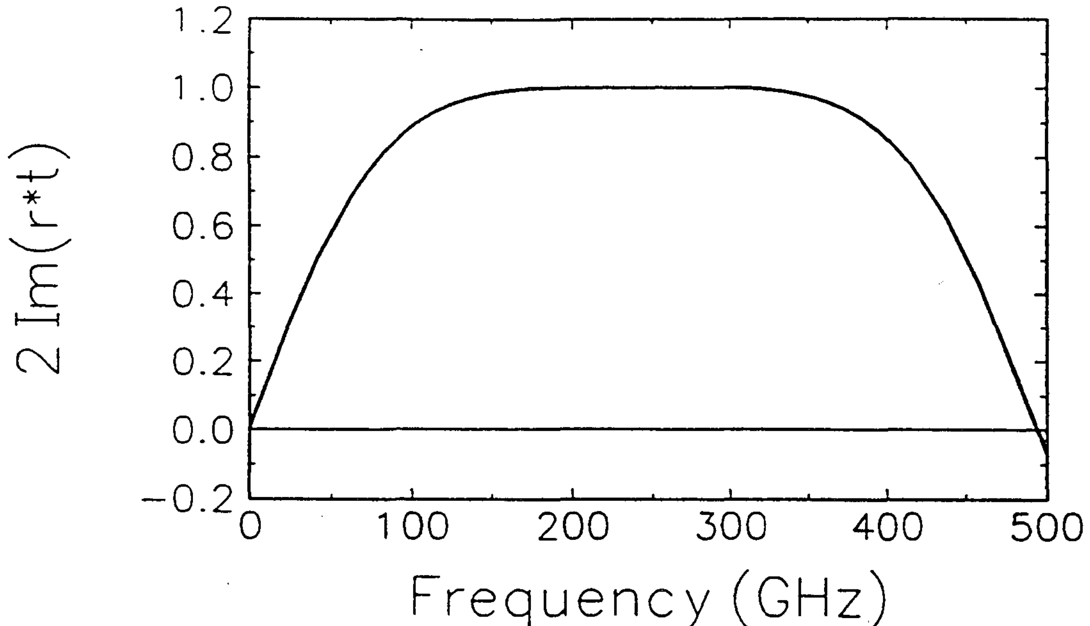


Figure 4.1

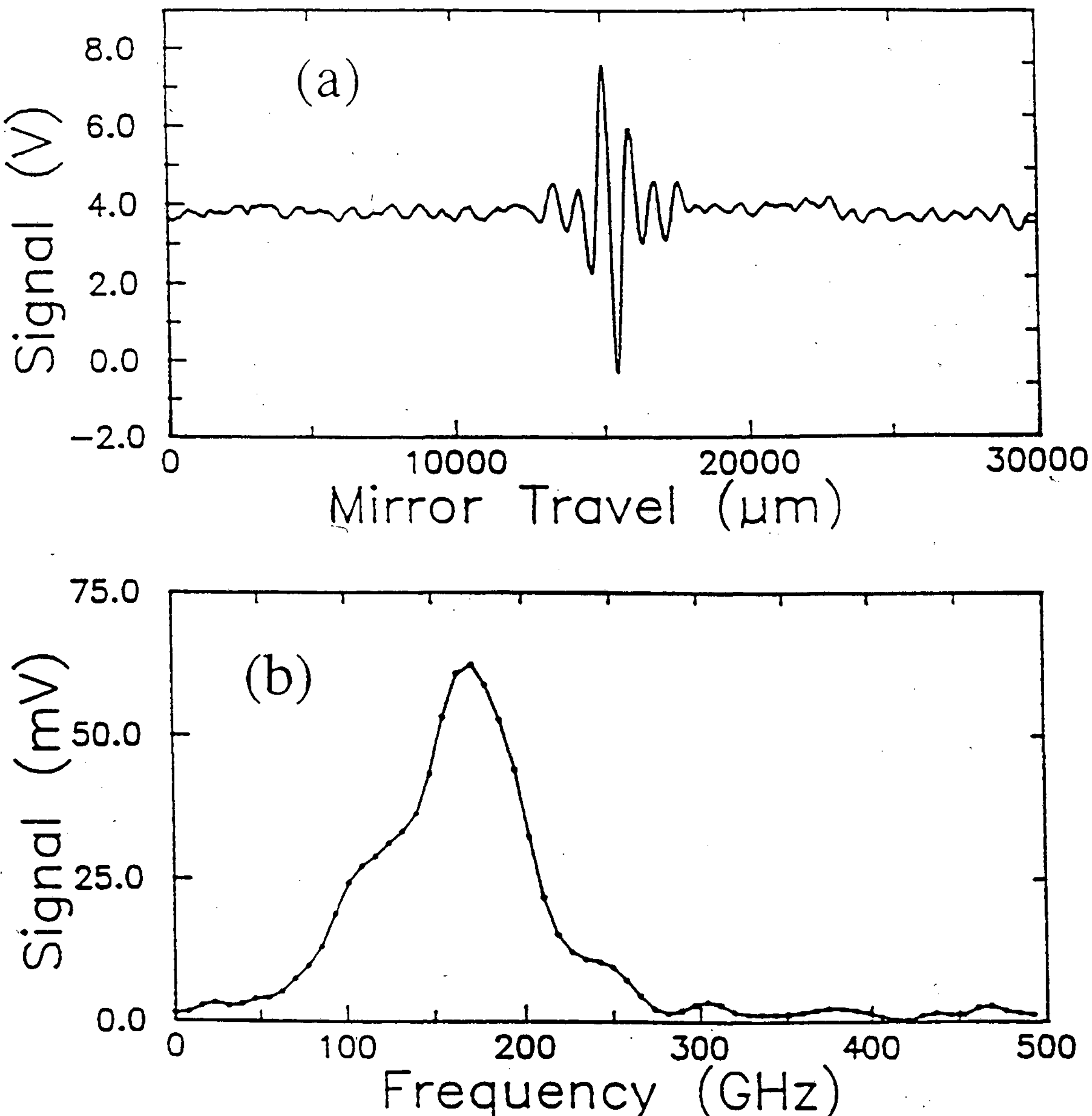


Figure 4.2

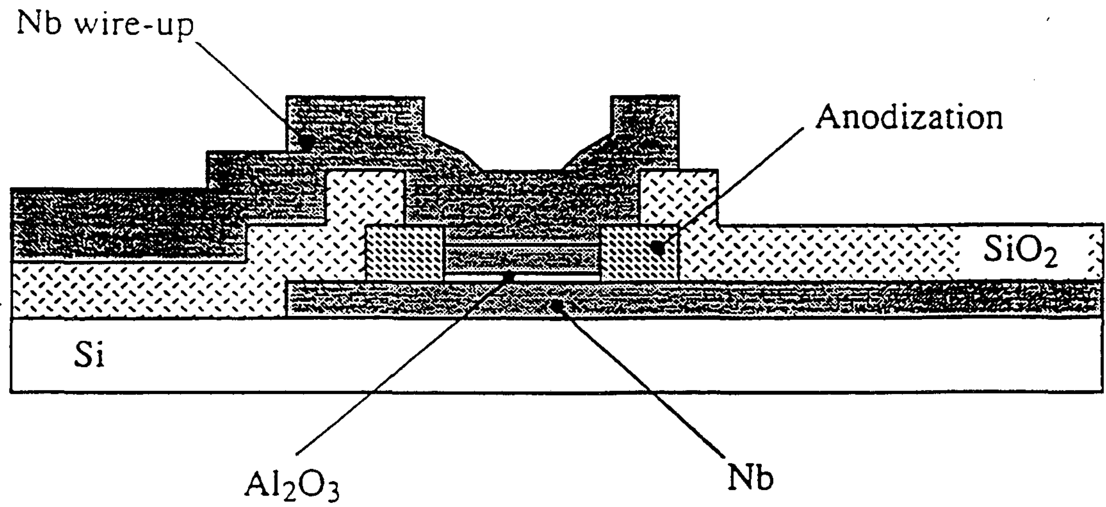


Figure 4.3

Figure 4.4

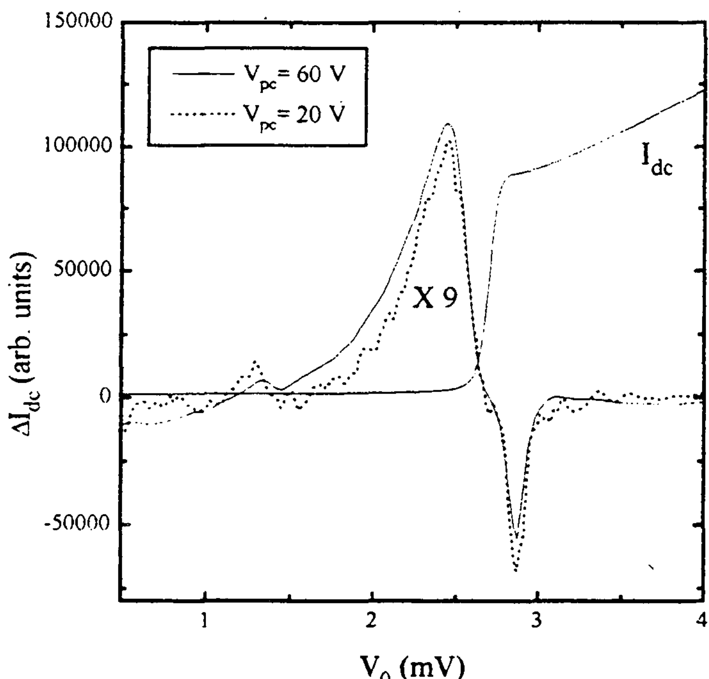


Figure 4.5

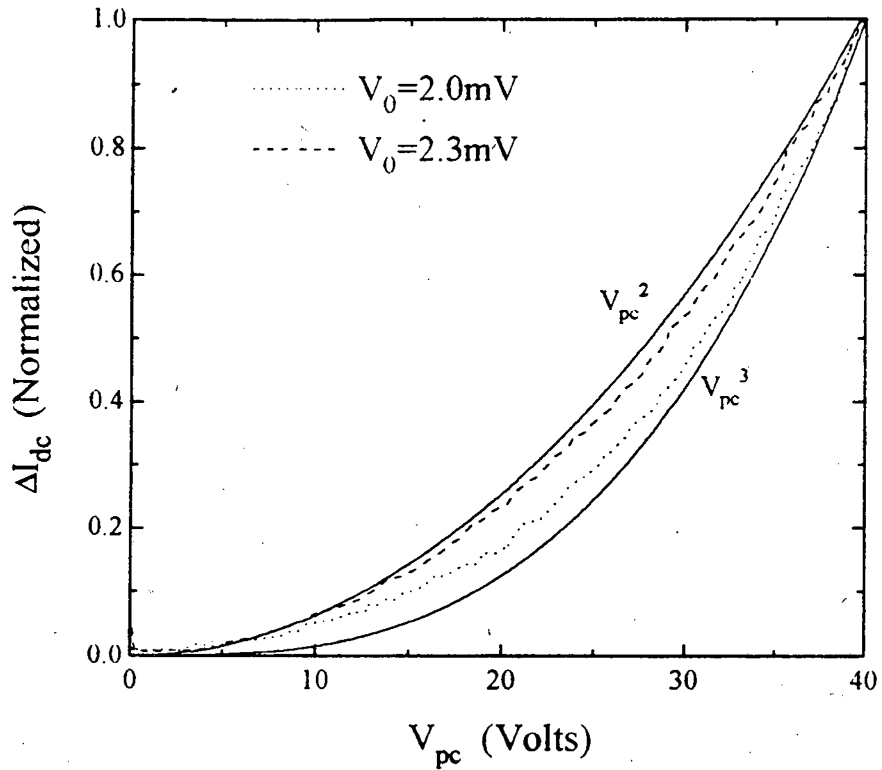


Figure 4.6

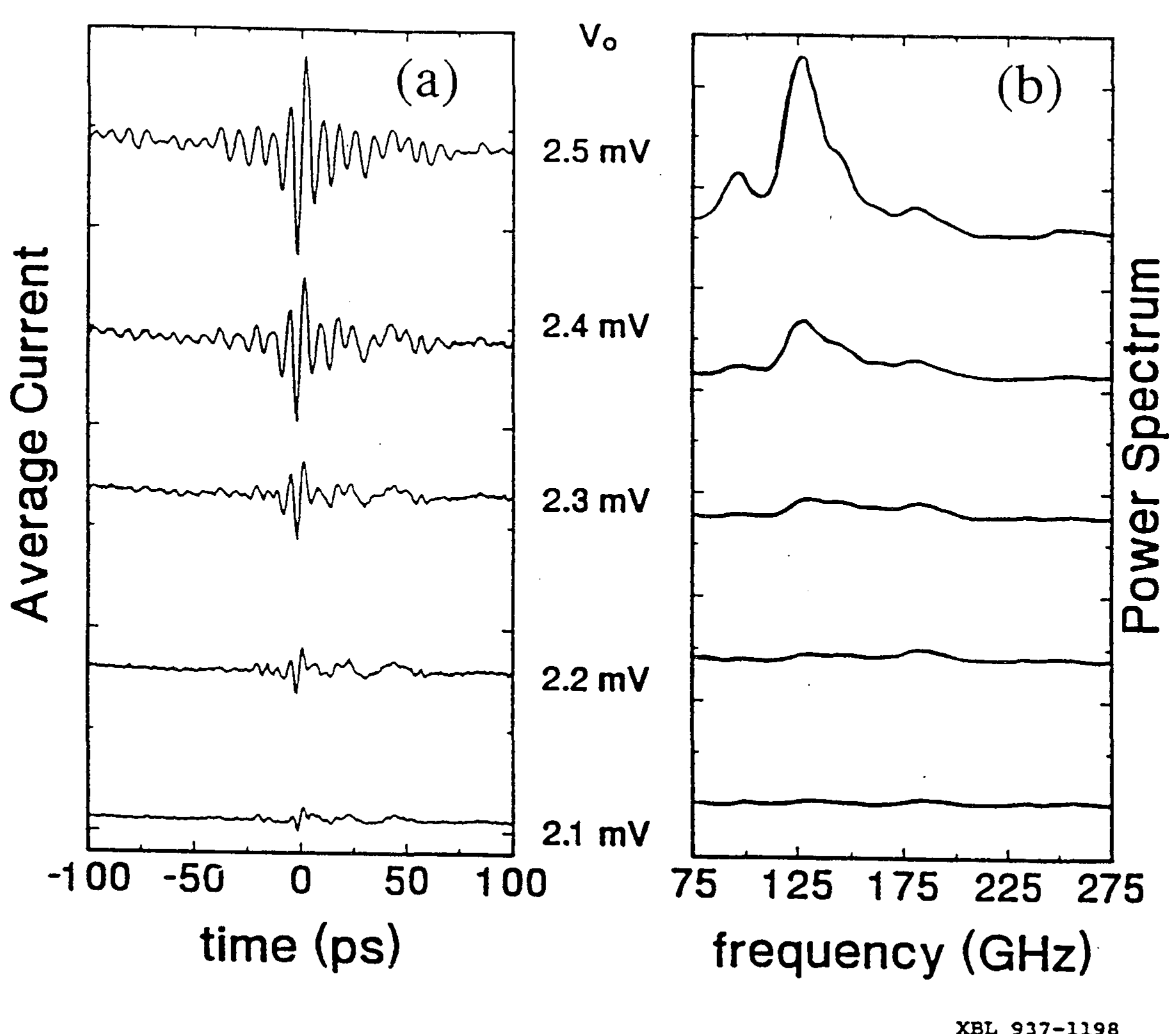


Figure 4.7

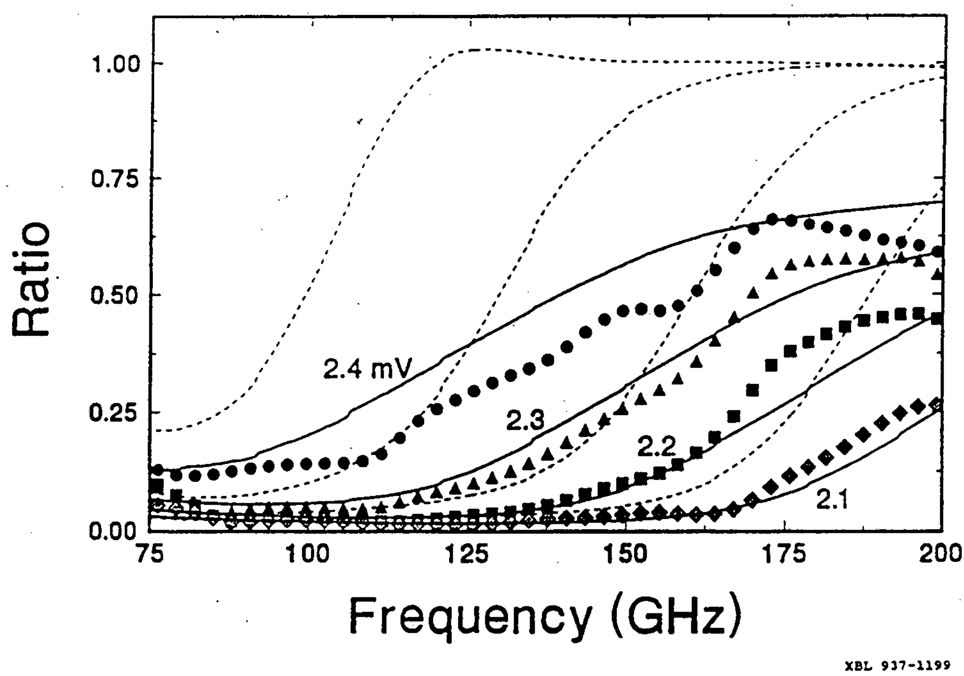


Figure 4.8

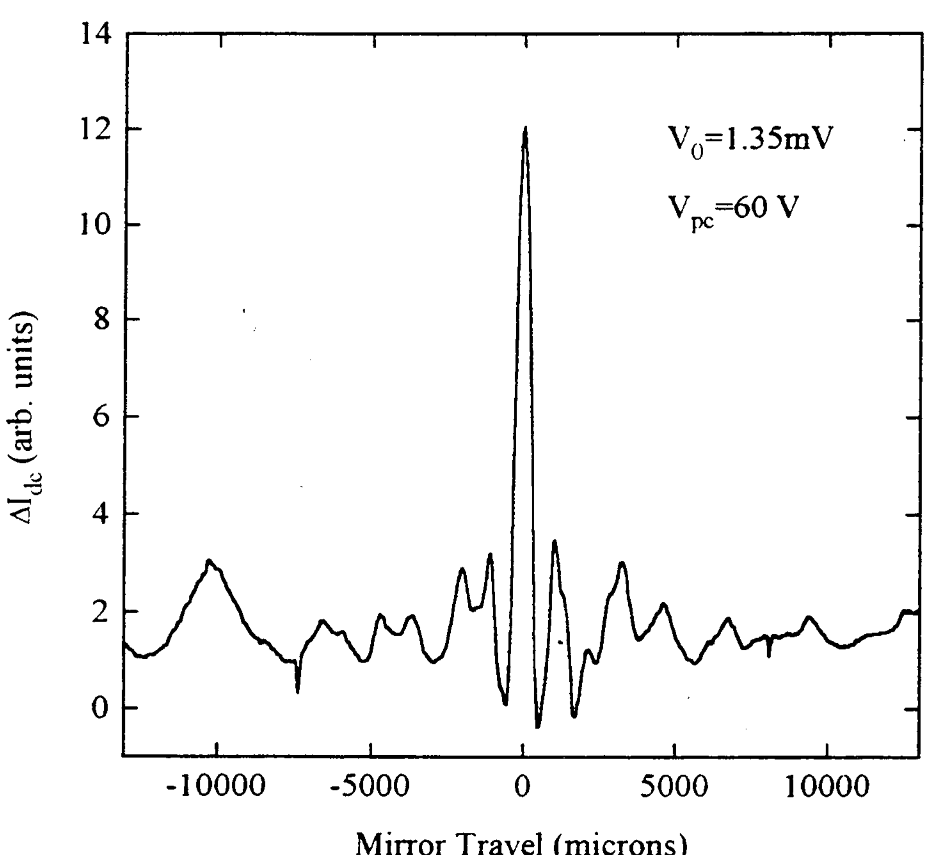


Figure 4.9

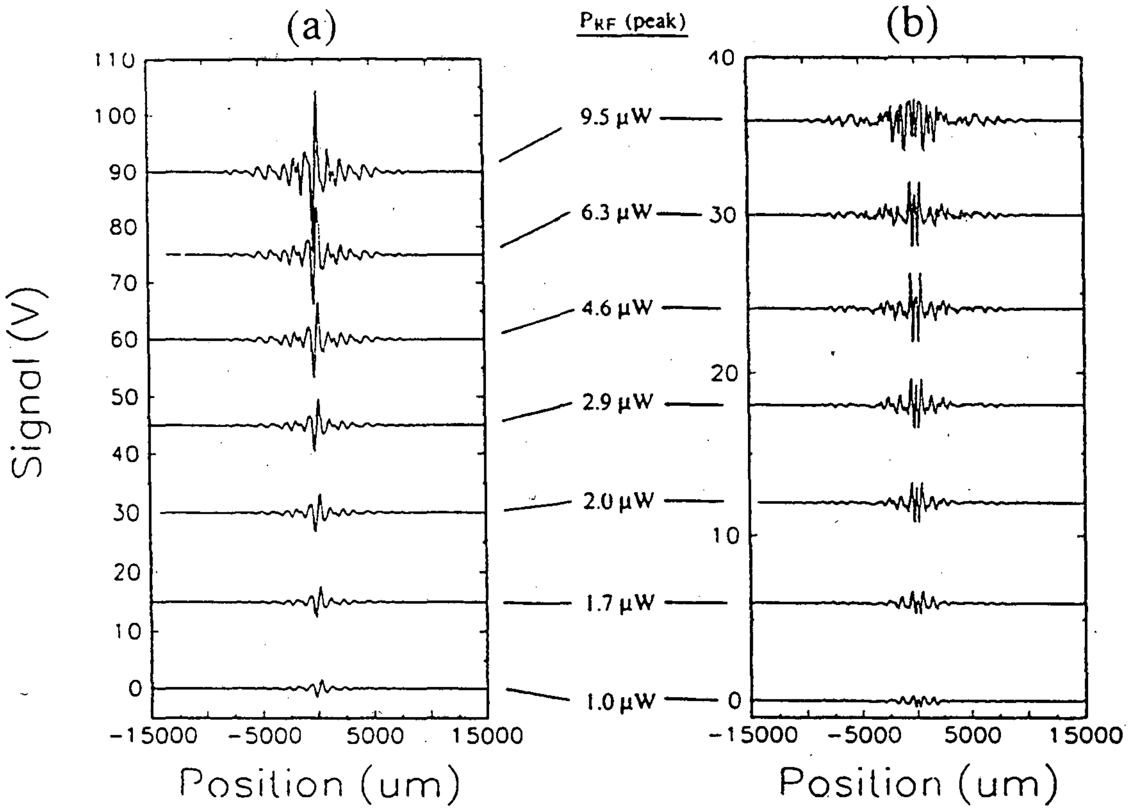


Figure 4.10

# Chapter 5

# The Quantum Point Contact: dc and High Frequency Transport Theory

Investigations of ballistic electronic transport in the quantum regime have led to a number of important as well as surprising discoveries. In particular the study of a short, narrow ballistic constriction or quantum point contact (QPC) has yielded a number of unexpected results. Independent investigations in 1988 by van Wees *et al.* [5.1] and Wharam *et al.* [5.2] led to the discovery that the conductance of a QPC is quantized in units of $2e^2/h$ ($\approx$13 KΩ). In addition, the QPC showed a step like behavior in its conductance as a function of contact width. Following this discovery, there have been numerous investigations of the QPC and related structures such as single and multiple quantum dots. Excellent reviews of the field have been given elsewhere [5.3-5.5]. In sharp contrast to the *dc* transport studies, our understanding of the high-frequency *ac* response is much less well developed because of the comparative lack of experimental results to compare to theory.

In this Chapter we will discuss briefly the *dc* transport properties of a ballistic QPC implemented in a two dimensional electron gas (2DEG). We will then derive the 2-terminal Landauer formula for the quantized conductance and a formula for the nonlinear *dc* $I_{dc} - V_{sd}$ curve. Next we describe two theories for the high frequency response of a QPC. We will only consider the generation of a rectified current signal via photon assisted transport (PAT) as opposed to the linear response, Y(ω), since the former is the more easily accessible experimental quantity. In Chapter 6 we will discuss experimental measurements of PAT in a QPC. The first *ac* transport theory we will discuss was developed by Landauer and Buttiker [5.6]. They discussed how a high speed barrier modulation experiment can be used to measure the barrier traversal time. The second theory we will consider is the application of the Tien-Gordon [5.7] approach to the problem of PAT in a QPC.

## 5.1 *dc* Transport

### 5.1.1 Fabrication of QPC device

The two basic conditions for observing quantized conductance are that the electronic transport must be in the ballistic regime and the constriction width must be of order the Fermi wavelength. The ballistic regime is distinguished by the feature that the mean free path for the electron must be greater that size of the sample. In order to obtain the longest mean free path, devices are typically fabricated in the ultra high mobility 2DEG of a GaAs/AlGaAs heterostructure [5.8]. In such heterostructures, it is now common to obtain electronic mobilities in excess of $10^6$ $cm^2/V$-s which corresponds to an electronic mean free path in excess of 10 μm. For these heterostructures, typical electronic densities range from $1\ to\ 4 \times 10^{11} cm^{-2}$ which corresponds to a Fermi wavelength, $\lambda_F$, of 40 to 80 nm. With electron beam lithography, it is possible to fabricate devices on this length scale.

To understand how the 2DEG is formed and how such high mobilities may be obtained, we can look to the band bending diagram for a modulation doped GaAs-AlGaAs heterostructure [5.9] shown in Figure 5.1(a). These heterostructures are grown with molecular beam epitaxy. The 2DEG is formed at the interface between GaAs and $Al_xGa_{1-x}As$ where the typical mole fraction, x, of aluminum is 0.3. The formation of the well at the GaAs/AlGaAs interface is due to the 0.3 V offset in the conduction bands of the two semiconductors and the attractive electrostatic field produced the ionized donors in the $n$ doped AlGaAs layer. In order to maximize the mobility of the electrons trapped in the well, a thin 20 nm undoped AlGaAs spacer layer is placed between the doped AlGaAs and the GaAs. The physical separation of the donors from the 2DEG greatly reduces the scattering of electrons in the 2DEG. The mobility of the electrons is further enhanced by the fact that AlGaAs and GaAs are almost perfectly latticed matched. Thus crystalline purity may be maintained at the interface. Confinement perpendicular to the interface leads to the formation of two dimensional subbands. The energy spacing of these subbands is typically in the 100mV range. For typical doping levels, only the lowest subband is occupied. Since devices are typically probed with energies less than a few mV's, it is an excellent approximation to treat the electrons as a pure two dimensional electron gas.

Although band bending provides confinement into a two dimensional sheet, we also require confinement in the lateral direction. Figure 5.1(b) shows a top view of a typical split gate QPC device. The hashed region at the center of the bar corresponds to a metallic gate which makes a Schottky contact to the semiconductor below. The metallic gates are defined with electron beam lithography. The lithographically defined width of the constriction is typically between 250 and 500 nm. Application of a negative voltage to the gate, depletes the electron gas below the gate. By varying the voltage on the gate, the width of the constriction may be varied. In addition, ohmic contacts are made to the electron gas on the two sides across the constriction. The ohmic contacts, due to their large size (typically 100x100μm), are defined with standard optical lithography.

### 5.1.2 QPC: Quantized Conductance and Nonlinear $I_{dc}$-$V_{sd}$ Curves- Experiment

The conductance as a function of constriction width is easily measured. First a small (typically less than 10 $\mu$V) *ac* voltage at 1 KHz is applied to the ohmic contacts and then the synchronous current is measured with a lock-in amplifier. In analogy with FET transistor terminology, we refer to the voltage across the ohmic contacts as the source-drain voltage, $V_{sd}$. Next this current is measured as a function of gate voltage or equivalently constriction width. Figure 5.2(a) shows the classic measurements by van Wees *et al.* in 1988 [5.1] of the conductance of such a constriction as a function of gate voltage. These measurements took place at T=0.6 K and at zero magnetic field. The conductance is pinched off at a gate voltage, $V_g$, of -2.2 V. The conductance shows the dramatic appearance of conductance steps quantized in units of $2e^2/h$. As we shall show in the next Section, the conductance quantization can be explained due to the formation of one dimensional subbands within the constriction.

In addition to measuring the conductance as a function of gate voltage, the conductance may also be measured as function of large source-drain voltage. Figure 5.2(b) are measurements by Kouwenhoven et al. [5.10] of the nonlinear $I_{dc} - V_{sd}$ curves at different values of the gate voltage near pinch off. Consider curve 1 at a $V_g$=-2.20 V. As expected from the data in Figure 5.2(a), the current flow is zero for small $V_{sd}$. As $V_{sd}$ is increased, the current remains zero until a threshold of 55 mV. As $V_{sd}$ is raised above 55 mV, the slope remains constant with a differential conductance of 1/80 K$\Omega$. As the gate voltage is reduced, the threshold moves to smaller values of $V_{sd}$, but the differential conductance remains relatively constant. We will discuss one possible model for these experimental results in the next Section.

At this point, it is appropriate to make some preliminary statements comparing the SIS junction to the QPC. Recall, from Fig. 3.2(a), that the *dc* I-V curve of an SIS junction also shows a strong nonlinearity. There is a sharp onset in the current at a voltage of

2.7 mV. The nonlinearity in the SIS junction, however, is much stronger than in the QPC. In the SIS junction, the current makes a discontinuous jump at the threshold voltage, while in the QPC there is only a turn on of the current. Nevertheless, the $I_{dc} - V_{sd}$ curve of a QPC is clearly nonlinear. It is this critical fact, that will allow us to use our terahertz interferometric technique to probe the dynamic response of a QPC. These experiments will be described in detail in Chapter 6. Another critical point of difference between the QPC and SIS junction is that in the QPC we can change the position of the threshold by simply changing the gate voltage. This is would be analogous to changing the bandgap of the superconductor making up the SIS junction.

Since we have not yet discussed the theory for the high frequency response of QPC, we cannot yet say what information may be obtained from our terahertz technique. Nevertheless, the simple analogies given above were sufficient to motivate us to start an effort to probe the high frequency response of a QPC. In Section 5.2 we will discuss two theories for the high frequency response so that we can understand better what microscopic information may be obtained from the high frequency measurements.

### 5.1.3 QPC: Quantized Conductance and Nonlinear $I_{dc}$-$V_{sd}$ Curves-Theory

In order to understand the appearance of steps in the conductance in Fig.5.2(a), we will apply the formalism developed by Landauer and Buttiker to calculate the current that flows through a one-dimensional system. Let us first begin with the Hamiltonian for the constriction in Fig. 5.1(b),

$$H = \frac{p_x^2}{2m^*} + eV(y) + \frac{p_y^2}{2m^*}, \qquad \{5.1\}$$

where x corresponds to the longitudinal direction through the constriction, y corresponds to the transverse direction, and $m^*=0.067m_0$ is the band mass. V(y) is the confinement potential produced by the gate in the transverse direction. We have explicitly left out the variation in the potential along the x direction. If the potential in the x direction, V(x),

varies smoothly on the length scale of $\lambda_F$, then the motion in the x and y directions can be decoupled [5.11]. In this case, the transport through the constriction will be wholly determined by the point along x at which the channel is the narrowest (often referred to in the literature as the bottleneck). It is at this point that we want to solve the Hamiltonian in equation {5.1}. For confinement in the y-direction, we use a parabolic potential, with $V(y) = V_0 + 1/2em^* \omega_y^2 y^2$. $V_0$ is the height of the barrier in the x-direction at the bottle neck as shown in Figure 5.3. $V_0$ is controlled by the gate voltage. We assume a linear dependence of $V_0$ on $V_g$ with $V_0 = -\mu V_g$. The potential variation in the x-direction is also assumed to be parabolic. The use of a parabolic potential has been supported by numerical simulations by Laux *et al* [5.12]. Their results showed that near the turn on of the constriction, the potential variation can be approximated as parabolic. However, as the barrier, $V_0$, is lowered the electrons can screen the potential and drastically change the shape of the barrier.

Equation {5.1} is trivial to solve once a parabolic potential is assumed for V(y). The solution is just a simple harmonic oscillator in the y-direction and a free particle in the x-direction with energies,

$$E_n = eV_0 + \frac{\hbar^2 k_x^2}{2m^*} + (n - 1/2)\hbar\omega_y \qquad n = 1,2,3... , \qquad \{5.2\}$$

where each n denotes a different subband. Each of the subbands is separated by an energy $\hbar\omega_y$. In order to compute the current through the junction, first refer to Fig.5.3, in which a *dc* bias, $V_{sd} = \mu_1 - \mu_2$, is applied across the junction. First we will calculate the zero temperature current that flows from left to right due to the electrons in the left reservoirs, using the Landauer-Buttiker formalism [5.13,5.14],

$$I_{LR} = e\sum_{n=1}^{N} \int_0^{\mu_1} dE \frac{1}{2} \rho_n v_n(E) T_n(E), \qquad \{5.3\}$$

where ρ(E) is the one-dimensional density of states, v(E) is the velocity of electrons, and T(E) is the transmission probability of the tunnel barrier. N is the number of occupied subbands in the left reservoir and is given by the largest integer for which the equation, $E_f > (N - 1/2)\hbar\omega_y$ holds true. The velocity of electrons is given by, $v_n(E) = dE_n / d(\hbar k_x)$ while the density of states including the spin degeneracy is, $\rho_n(E) = (dk_x / dE_n) \cdot 2/\pi$. Using these relations, and similar relations for the right side of the barrier, we obtain an expression for the total current through the junction,

$$I_{dc} = \frac{2e}{h}\sum_{n=1}^{N}\left[\int_0^{\mu_1} dE T_n(E) - \int_0^{\mu_2} dE T_n(E)\right]. \qquad \{5.4\}$$

This result is particularly simple, due to the fortuitous fact that in one dimension, the density of states is inversely proportional to the velocity. This expression can be simplified further by assuming that the Fermi energy which is of order 10meV is large compared to the applied potential, $eV_{sd}$. In this case, we obtain the well known two-terminal Landauer formula for the conductance, $G=I_{dc}/V$ [5.15],

$$G = \frac{2e^2}{h}\sum_{n=1}^{N} T_n(E_f), \qquad \{5.5\}$$

from which it is clear, that the fundamental unit for the conductance of a quantum ballistic wire is $2e^2/h$.

The explanation of the steps in Fig. 5.2(a) is now straight forward. As the gate voltage is reduced to zero, the barrier height, $V_0$, in Fig. 5.3 is lowered. As $V_0$ is lowered, successive subbands turn on, and the conductance steps in units of $2e^2/h$. Fig 5.2(a) then is an experimental measure of the transmission coefficient of the tunnel barrier. Buttiker [5.16], has treated explicitly the case for quantized transmission of a saddle-point constriction, using the results of Conner [5.17] and Fertig and Halperin [5.18], for the transmission probability of a parabolic potential,

$$T_n(E) = \frac{1}{1+\exp\left(-2\pi\frac{E-(V_0+\hbar\omega_y(n+1/2))}{\hbar\omega_x}\right)}. \qquad \{5.6\}$$

This expression resembles the Fermi-Dirac distribution function. $T_n(E)$ for a given subband n will approach unity as the electronic energy, E, exceeds, $V_0 + \hbar\omega_y(n+1/2)$. In addition, the broadening of $T_n(E)$ is the same for each subband, and is given the *effective temperature*, $\hbar\omega_x/2\pi$. This result is valid as long as the true sample temperature is less than the *effective temperature*. This is the case in our experiments since $k_BT$ at 0.5 K is 0.04 meV and the $\hbar\omega_x/2\pi$ is typically in the meV range.

Now, we will consider briefly the effects of an applied magnetic field, B, perpendicular to the plane of the 2DEG on the lowest mode (n=1) of the constriction. Fertrig and Happerin [5.18] have calculated the transmission coefficient for this case,

$$T(E) = \frac{1}{1+\exp\left(-2\pi\frac{E-(V_0+\hbar\Omega_y/2)}{\hbar\Omega_x}\right)}. \qquad \{5.7\}$$

Here the ω's have been replaces by Ω's where,

$$\Omega_x(B) = \left[\left(\frac{\vartheta^4}{4}+\omega_x^2\omega_y^2\right)^{1/2} - \frac{\vartheta^2}{2}\right] \qquad \{5.8a\}$$

$$\Omega_y(B) = \left[\left(\frac{\vartheta^4}{4}+\omega_x^2\omega_y^2\right)^{1/2} + \frac{\vartheta^2}{2}\right] \quad , \qquad \{5.8b\}$$

where $\vartheta^2 = \omega_c^2 + \omega_y^2 - \omega_x^2$ and $\omega_c = eB/m^*$. The experiments in this thesis take place in the low field limit, where $\omega_x$ and $\omega_y >> \omega_c$. Typical values for $\omega_x$ and $\omega_y$ are in the many mV range whereas our cyclotron energies are in the mV range (B <1Telsa). In this limit, the above expressions take a particularly simple form,

$$\Omega_x(B) = \omega_x\left[1-\frac{\omega_c^2}{2(\omega_x^2+\omega_y^2)}\right] \qquad \{5.9a\}$$

$$\Omega_y(B) = \omega_y\left[1+\frac{\omega_c^2}{2(\omega_x^2+\omega_y^2)}\right]. \qquad \{5.9b\}$$

The application of a magnetic field will have two effects on the conductance steps in Fig. 5.2(a). First the steps will become sharper since the *effective temperature*, $\hbar\Omega_x/2\pi$, becomes smaller as the field is increased. Secondly the steps will become longer since the effective confining potential, $1/2m^*\Omega_y^2y^2$, becomes tighter as B increases.

With the theory for the conductance steps in Fig. 5.2(a) on a firm footing, we will now move on to discussing the origin of the nonlinear I-V curves in Fig. 5.2(b). In contrast to the theory for the conductance steps, the exact details as to the microscopic origins of the nonlinear I-V curves is not well understood. Kouwenhoven *et al.* [5.10] has developed a phenomenological model for the origin of the nonlinear conductance. Before going through this model, let us first try to understand the physical origin of the nonlinearity. Referring back to Fig. 5.3, consider the case where the barrier height, $V_0$, is much larger than $E_f$. This corresponds the pinched off regime where a large negative voltage is applied to the gates as for curve 1 in Fig. 5.2(b). Now consider what happens when a *dc* bias, $V_{sd}$, is applied across the junction, where $V_{sd}=\mu_1-\mu_2$. For small $V_{sd}$, the current is nearly zero since the transmission coefficient of the barrier is nearly zero when the electronic energy, E, is much less than $V_0$. However if $V_{sd}$ is made large enough, then the electrons on the left side of the barrier will have enough energy to traverse the barrier, and a measurable current will flow. For curve 1 in Fig. 5.2(b), the threshold for current flow appears at $V_{sd}$=55 mV. This threshold can be moved to lower voltages by lowering $V_0$ which is accomplished by reducing the magnitude of $V_g$.

An attempt to quantify this discussion can be made by appealing to the Landauer-Buttiker formula, equation {5.4}. Before using this equation, we must point out that this equation is only valid in the linear transport regime. We begin by introducing a phenomenological parameter, m, which represents the fraction of voltage, $V_{sd}$, that is

dropped across the side of the barrier which is the source of current flow. Looking once again at Fig. 5.3, for $\mu_1>\mu_2$, the left side of the barrier is the source of current, and $\mu_1$=mV, while $\mu_2$=(1-m)V. For $\mu_2>\mu_1$, the equations would be reversed. For a perfectly symmetric barrier, one would expect m=1/2, that is the voltage is dropped equally across the barrier. For simplicity, let us consider an opaque barrier, where

$$T(E) = 0 \qquad E<V_0 \qquad \{5.10a\}$$

$$T(E)=1 \qquad E>V_0. \qquad \{5.10b\}$$

In this case, with equation {5.4}, it is trivial to show that the differential conductance ,$g=dI_{dc}/dV_{sd}$, is,

$$g=0 \qquad mV_{sd}<(V_0-E_f) \qquad \{5.11a\}$$

$$g=m\cdot 2e^2/h \qquad mV_{sd}>(V_0-E_f). \qquad \{5.11b\}$$

This model can be fit to the data in Fig. 5.2(b) with m=0.2.

Currently, there is no formal justification for the model given above, although it fits the data quite well. Unfortunately, the microscopic origin of m it is not considered a *hot topic* in the mesoscopic community, and as such has not been thoroughly investigated experimentally or theoretically. As we shall show later, PAT is a direct probe of m, and can measure its dependence on $V_{sd}$.

One possible origin of the m factor can be understood by considering Coulomb charging effects [5.19] in the tunnel barrier. This line of reasoning is motivated by the fact that charging effects in quantum dots results in highly nonlinear $I_{dc}-V_{sd}$ curves [5.20]. The argument for the QPC is as follows. When current is not flowing through the junction, m=1/2 as expected for a symmetric barrier. Once current starts to flow, however, electrons will reside in the barrier region. These electrons will impede the flow of other electrons due to Coulomb repulsion, reducing the conductance of the channel. This is equivalent to making m less than 1/2. In this model, m is explicitly a function of $V_{sd}$.

## 5.2 *ac* Transport

In the previous Section, we discussed in detail the fundamental *dc* transport properties of a QPC. The *dc* transport experiments are fairly well understood and experimentalists as well as theorists have moved in other directions. One of those directions is high frequency *ac* transport. Recently several theoretical studies of the nonlinear rectified response [5.21-5.24] and the linear response [5.25-5.27] of mesoscopic devices have appeared, increasing researchers' motivation to conduct more experiments. Another motivation for high frequency measurements is to obtain a direct measure of the traversal time across a tunnel barrier [5.28,5.29]. As we will show below, the traversal time is both within our frequency range and appears explicitly in the rectified photocurrent response for a QPC.

Calculating the *ac* response of a QPC is much more difficult than calculating the *ac* response of an SIS junction. The critical difference between the SIS junction and the tunnel barrier system, is that the height of the tunnel barrier for the QPC is on the order of the Fermi energy, while in the SIS junction the height of the tunnel barrier is effectively infinite. The infinite barrier height for the SIS case implies that *ac* modulation of the barrier height can be neglected. An applied *ac* potential to an SIS junction can only modulate the quasiparticle energies in the leads of the SIS junction. Modulation in the leads can easily be solved using the Tien-Gordon [5.7] approach discussed in Chapter 3. In sharp contrast to the SIS tunnel barrier, the QPC barrier height is finite, and *ac* modulation of the barrier can lead to observable effects. In general an applied *ac* potential to a QPC can modulate the electron energies in the leads *and* in the barrier region. A theoretical solution for the response to an arbitrary spatial *ac* potential applied across the QPC is a difficult problem and there currently does not exist a simple solution.

Given these fundamental difficulties in developing a general theory for the *ac* response of a QPC, we will only discuss two specialized theories. The first is one developed by Buttiker and Landauer [5.28] which treats the case of an oscillating potential

barrier but neglects any oscillations in the leads. The second will be a straight forward application of the Tien-Gordon [5.7] approach to the QPC. This approach implicitly assumes that excitations only take place in the leads of the QPC and not in the tunnel barrier region. Both approaches, though, predict a frequency dependent rectified current spectrum.

### 5.2.1 Buttiker-Landauer Approach: Traversal Time For Tunneling

Buttiker and Landauer [5.28] treat the case of oscillating barrier, where

$$V(x,t) = V(x) + V_1(x)\cos\omega t. \qquad \{5.12\}$$

V(x) is the static potential in Fig. 5.3 and $V_1(x)$ is a small modulation restricted to the barrier region. They assume the electron is free in the other two transverse dimensions. Obviously this does not correspond to the QPC where the electron is confined in two transverse dimensions. Nevertheless, we expect to gain some physical intuition from their free particle approach. As expected from the discussions in Chapter 3, an electron incident on the barrier, interacts with the modulated potential, $V_1(x)\cos\omega t$, and will absorb or emit photons of energy $\hbar\omega$. When the frequency is so low that the period of oscillation is longer than the traversal time across the barrier, $\tau_t$, then the incident electron sees an effectively static barrier. When the frequency is high compared to $1/\tau_t$, the electron sees many periods of the oscillating potential. In this case, the electron can absorb or emit photons as it traverses the barrier. Clearly from Fig. 5.3, an electron that gains energy by absorbing a photon will traverse the barrier more easily. The crossover between these two regimes occurs when $\omega\tau_t \approx 1$. $\tau_t$ is given by,

$$\tau_t = \int_{x_1}^{x_2} \left[ \frac{m^*}{2(eV_0(x) - E)} \right]^{1/2} dx \ , \qquad \{5.13\}$$

where $x_1$ and $x_2$ are the classical turning points for a particle of energy E incident on the barrier. This equation is strictly only valid in the WKB limit at energies well below the barrier top. An equation for $\tau_t$ when $E>>eV_0$ can be found by reversing E and $eV_0(x)$ in equation {5.13} above.

Let us apply equation {5.13} to the case of a parabolic potential, with $V(x) = V_0 - m^* \omega_x^2 x^2 / 2e$. For this form of the potential, the integral in equation {5.13} is elementary, and $\tau_t = \pi/\omega_x = T_x/2$. This result has a simple physical interpretation. $\tau_t$ is just half the round trip time, $T_x$, of a classical harmonic oscillator in the inverted potential, $-V(x)$. In addition, as with a classical oscillator, $\tau_t$ does not depend on the electron energy, E. At this point we should refer back to equation {5.6} for the T(E) for a QPC. Recall that $\omega_x$ shows up explicitly in the *effective temperature*, $\hbar\omega_x/2\pi$. Typical values for this *effective temperature* are in the mV regime which corresponds to frequencies in the hundreds of GHz range. This is exactly in the range of our terahertz interferometric technique which makes it ideal for a *dynamic* measurement of $\tau_t$.

Buttiker and Landauer [5.28] did not treat explicitly the case of a parabolic potential. Instead they treated the case of a rectangular barrier with height $V_0$ and width d, centered at x=0 as shown in Figure 5.4. In addition they assume that $T(E)<<1$ and that $E << V_0$. For this case they have calculated the transmission probability, $T_\pm$, of the two side bands at energies $E \pm \hbar\omega$,

$$T_\pm = \frac{1}{4}\alpha^2 T(E)(e^{\pm\omega\tau} - 1)^2. \qquad \{5.14\}$$

In Fig 5.4(a) we show the low frequency limit of equation {5.14}. In this case, the electrons in the upper and lower side bands still tunnel through the barrier at energy E, because of the appearance of T(E) in the transmission probability,

$$T_\pm(E) = T(E)(eV_1\tau / 2\hbar)^2. \qquad \{5.15\}$$

This result does not depend on frequency. Unlike the SIS case, here the electron absorbs the photon after the barrier. The situation is dramatically different in the high frequency regime as depicted in Fig. 5.4(b). Here ,

$$T_+ = \frac{1}{4}\alpha^2 T(E+\hbar\omega), \qquad \{5.16a\}$$

where $\alpha=eV_1/\hbar\omega$ (as in Chapter 3). This result is similar to the Tien-Gordon result of Chapter 3. The upper sideband corresponds to the following process. The electron incident on the barrier absorbs a photon of energy $\hbar\omega$ and then transmits through the barrier. This sideband is weighted by the usual factor, $\alpha^2/4$. The lower sideband, though, undergoes a different process. This sideband has a strength,

$$T_- = \frac{1}{4}\alpha^2 T(E). \qquad \{5.16b\}$$

The appearance of T(E) implies that this electron does not absorb the photon till after it has passed through the barrier. Nevertheless this sideband is still weighted by the factor, $\alpha^2/4$.

Experimentally one can try to measure the traversal time, $\tau_t$, by measuring the rectified current, $\Delta I_{dc}$. At low frequencies, one would expect a rectified current,

$$\Delta I_{dc}(\omega) = \frac{4e^2}{h} T(E_f)\cdot V_{sd}\cdot[eV_1\tau/2\hbar]^2, \qquad \{5.17a\}$$

in the presence of a small applied bias, $V_{sd}$. This expression is found by using the appropriate equations for $T_\pm$ in equation {5.4}. At low frequencies, the rectified current is frequency independent. When the frequency becomes greater than $1/\tau_t$,

$$\Delta I_{dc}(\omega) = \frac{e^2}{2h}\left[T(E_f+\hbar\omega)+T(E_f)\right]\cdot V_{sd}\cdot\alpha^2 \qquad \{5.17b\}$$

will become frequency dependent. A knee will appear in the rectified current spectrum when $\omega\tau_t \approx 1$. The beauty of this experiment is that no fitting parameters are needed in extracting $\tau_t$ from the spectrum of $\Delta I_{dc}$. In contrast, extracting $\tau_t$ from *dc* transport experiments of the conductance requires a knowledge of a number of model dependent

parameters. For example if we assume that the potential is parabolic (not valid well away from the turn on), then we need to know $\omega_x$, $\omega_y$, and $\alpha$ (see Section 5.1.2) before we can calculate $\tau_t$. Although the *ac* transport measurements are more direct, the experiments are much more difficult. The difficulty lies in the fact that T(E) must be small for the above expressions to remain valid. In this case $\Delta I_{dc}$ will be small and hard to measure.

To conclude this Section, we would like to repeat that this is not a rigorous theory for the high frequency response of a one-dimensional oscillating tunnel barrier. We have essentially grafted the Buttiker-Landauer result which applies to a large area rectangular tunnel barrier onto the one-dimensional arbitrary tunnel barrier problem. Nevertheless, this is a start at trying to understand the microscopic origin of the high frequency response of a one-dimensional tunnel barrier.

### 5.2.2 Tien-Gordon Approach

We will now apply the Tien-Gordon method to the problem of photon assisted transport in a QPC. This method was applied successfully in Chapter 3 to calculate the amount of photocurrent induced in a SIS junction in the presence of a microwave signal. We begin with a beam at energy, E, incident on a barrier from the left as in Figure 5.5. We assume that a microwave signal of the form,

$$V_L = mV_{sd} + V_{L1}\cos\omega t, \qquad \{5.18\}$$

is coupled to the left side of the barrier. Since this is a three terminal device (gate, source, and drain), it is possible to apply different voltage signals to the two sides of the barrier. As we will discuss in Chapter 6, we find a large difference between the amount of microwave signal coupled to the two sides of the barrier. In contrast to the QPC, the SIS junction is only a two terminal device, so only one voltage appears in all the calculations. One terminal of the SIS junction is at the applied voltage while the other terminal is kept at *ground*. For the QPC, we take the point at the center of the tunnel barrier as ground. In

addition, in equation {5.18}, we have included the m factor, which was introduced in Section 5.1.2 to explain the nonlinear $I_{dc} - V_{sd}$ curves.

Since we assume that the signal in equation {5.18} only modulates the left lead and not the barrier, the incident electronic wave function is modified as in equation {3.16}. For the case of low microwave power levels, the incident wave function is split into three waves,

$$\Psi(x,t) = \Psi(x)e^{-j(E+eV)t/\hbar}\left[\left(1-\frac{\alpha_L^2}{4}\right)+\frac{\alpha_L}{2}e^{-j\omega t}-\frac{\alpha_L}{2}e^{j\omega t}\right], \quad \{5.19\}$$

as shown in Fig. 5.5. Here $\alpha_L = eV_{L1}/\hbar\omega$. The new wave function will modify the density of states on the left side of the barrier. This new density of states, which is proportional to $\Psi^*\Psi$, will lead to a change in the dc current flowing from left to right,

$$\Delta I_{dc}^{LR} = \frac{e\alpha_L^2}{2h}\int_0^{E_f} T(E+\hbar\omega+emV_{sd})+ T(E-\hbar\omega+emV_{sd})-2T(E+emV_{sd})dE \quad \{5.20\}$$

where we have used equation {5.3} with the modified density of states. Notice that the rectified current is proportional to the power in the left lead through the quantity $\alpha_L^2$. This means that we can apply our terahertz interferometric technique to measure the spectrum of the rectified current. We have assumed in deriving equation {5.20} that the cancellation between the density of states and the velocity still occurs, even though they must be evaluated at different energies in the integral of equation {5.3}. A similar equation to {5.20} is found for the right side of the barrier in the presence of a signal of the form,

$$V_R = -(1-m)V_{sd} + V_{L1}\cos\omega t \quad \{5.21\}$$

The total induced current is then given by,

$$\Delta I_{dc} = \frac{e(\alpha_L^2 + \alpha_R^2)}{2h} \int_0^{E_f} T(E + \hbar\omega + emV_{sd}) - T(E + \hbar\omega - e(1-m)V_{sd})$$
$$+T(E - \hbar\omega + emV_{sd}) - T(E - \hbar\omega - e(1-m)V_{sd})$$
$$-2T(E + emV_{sd}) + 2T(E - e(1-m)V_{sd}) \ dE \ . \qquad \{5.22\}$$

To better understand equation {5.22}, we will treat the special case when all terms above are negligible compared to the first term. The first term corresponds to photon absorption on the left side of the barrier. This will be the dominant term for a large barrier, $V_{sd}$, and photon energy. In this case the rectified current is given simply by,

$$\Delta I_{dc} = \frac{e(\alpha_L^2 + \alpha_R^2)}{2h} \int_0^{E_f} T(E + \hbar\omega + emV_{sd}) dE. \qquad \{5.23\}$$

By measuring the $\Delta I_{dc}$ as a function of frequency, we get a direct measure of the integral of the transmission coefficient, T(E). For the barrier in Fig. 5.3, the spectrum will have a knee at a frequency, $\omega_c = (eV_0 - E_f - emV_{sd})/\hbar$ . If $V_0$ is raised or $V_{sd}$ lowered this knee will move to higher frequencies. This knee will not be perfectly sharp. It will be broadened by the same mechanism that broadens T(E).

We now try to answer the critical question: What can be learned from measuring $\Delta I_{dc}$ at high frequencies? A critic would say that the all the necessary microscopic information about the tunnel barrier can be found from *dc* transport measurements. For example, from equation {5.5}, it is clear that the conductance steps in Fig. 5.2(a) are directly related to T(E). By measuring the broadening of T(E), one can obtain a measure of the traversal time across the barrier. These statements are true. Unfortunately, though, in order to obtain T(E) from the *dc* transport data, one first has to know the relationship between $V_g$ and the barrier height $V_0$. Previously we made the approximation that $V_0 = -\mu V_g$. If this relationship holds, then $\mu = -E_f / eV_{gp}$, where $V_{gp}$ is the pinch off voltage (-2.2 V) in Fig. 5.2(a). In general, though a linear relationship between $V_0$ and $V_g$ need not hold. In this case, $\mu$ cannot be found from *dc* transport measurements. Without $\mu$, the

traversal time $\tau_t$ cannot calculated. Similarly, nonlinear $I_{dc} - V_{sd}$ curve measurements cannot determine the m factor directly when m depends on the source-drain voltage, $V_{sd}$.

In contrast to the *dc* transport measurements, broadband *ac* measurements of $\Delta I_{dc}(\omega)$ can provide a direct measure of $\mu, \tau_t$, and m. To find $\mu$, we first measure $\Delta I_{dc}(\omega)$ as different gate voltages and monitor the changes in the knee at $\omega_c$. From these measurements we can find $\mu$ as an arbitrary function of $V_g$,

$$\mu(V_g) = -\Delta(\hbar\omega_c) / \Delta(eV_g). \qquad \{5.24\}$$

$\tau_t$ is found directly from the broadening of the knee at $\omega_c$ in $\Delta I_{dc}(\omega)$. The broadening may be more easily found by taking the derivative of $\Delta I_{dc}(\omega)$. The m factor can be found by measuring $\Delta I_{dc}(\omega)$ at different source-drain voltages, $V_{sd}$, and once again monitor changes in the knee at $\omega_c$. From these measurements,

$$m(V_{sd}) = \Delta(\hbar\omega_c) / \Delta(eV_{sd}). \qquad \{5.25\}$$

Thus we see that the *ac* transport measurements give us direct microscopic information about the tunnel barrier. From equation {5.23} we see that, $\Delta I_{dc}(\omega)$ is a direct measure of T(E) and its dependence on $V_g$ and $V_{sd}$. Although it is fairly well accepted that the potential looks parabolic near the turn on, it is not known exactly how the shape changes after turn on. In fact numerical calculations show that the shape of the barrier changes dramatically due to charging effects when current flows through the barrier [5.12]. We can study these changes directly by making measurements of $\Delta I_{dc}(\omega, V_g, V_{sd})$.

There is another subtle, but important difference between the *ac* transport measurements and the *dc* transport experiments. In the *ac* transport experiments, we use photoexcited electrons to probe the tunnel barrier at different energies. By changing the intensity of the incident photon flux, we can adjust the number of electrons which are in the barrier region. In this way, we can directly learn how the barrier shape depends on charging effects. In contrast, in the *dc* transport experiments, the number of carriers in the

barrier region are not under direct experimental control. For example, if we want to measure T(E) with *dc* transport methods, we measure the current through the tunnel barrier as a function of gate voltage. Unfortunately the shape of the barrier will change in an uncontrolled fashion once the channel turns on. However, with the *ac* technique, we can keep the gate voltage fixed, and just vary the photon energy to measure T(E). If we want to see how T(E) depends on the number carrier in the barrier region, we can change the intensity of the photon flux.

## 5.3 Conclusions

In this Chapter we have discussed the classic *dc* transport experiments on a quantum point contact. In particular, the most dramatic finding was that the conductance of a one-dimensional channel is quantized in units of $2e^2/h$ (13 KΩ). We have also discussed two possible theories for the high frequency response of a QPC, and in particular their predictions for the rectified photocurrent spectrum. Both theories predict that $\Delta I_{dc}(\omega)$ will become frequency dependent at sufficiently high frequencies. From the Landauer-Buttiker point of view (barrier modulation), high frequency is set by the condition that $\omega>1/\tau_t$. In the Tien-Gordon approach (lead modulation), $\Delta I_{dc}(\omega)$ becomes frequency dependent when $\omega>(eV_0\text{-}E_f\text{-}emV_{sd})/\hbar$. From an experimentalists point of view, both theories predict a frequency dependent $\Delta I_{dc}(\omega)$, so our first step is to look for a frequency dependent $\Delta I_{dc}(\omega)$. This will be the main subject of the next Chapter.

## 5.4 References


[5.1] B.J. van Wees, H. van Houten, C.W.J. Beenakker, J.G. Williamson, L.P. Kouwenhoven, D. van der Marel, and C.T. Foxon, *Phys. Rev. Lett.* 60, 848 (1988).

[5.2] D.A. Wharam, T.J. Thornton, R. Newbury, M. Pepper, H. Ahmed, J.E.F. Frost, D.G. Hasko, D.C. Peacock, D.A. Ritchie, and G.A.C. Jones, *J. Phys. C* 21, L209 (1988).

[5.3] H. Ehrenreich, and D. Turnbull eds., *Solid State Physics-Semiconductor Heterostructures and Nanostructures* (Academic Press, New York, 1991).

[5.4] M. Reed ed., *Semiconductors and Semimetals* (Academic Press, New York, 1990).

[5.5] H. Grabert and M.H. Devoret eds., *Single Charge Tunneling* (Plenum Press, New York, 1991).

[5.6] M. Buttiker and R. Landauer, *Phys. Rev. Lett.* **49**, 1739 (1982).

[5.7] P.K. Tien and J.R. Gordon, *Phys. Rev.* **129**, 647 (1963).

[5.8] C.T. Foxon, in: Interfaces, Quantum Wells and Superlattices, edited by C. Richard Leavens and Roger Taylor (Plenum Publishing Corporation, 1988).

[5.9] R. Dingle, H.L. Stormer, A.C. Gossard, and W. Wiegman, *Appl. Phys. Lett.* 7, 665 (1978).

[5.10] L.P. Kouwenhoven, B.J. van Wees, C.J.P.M. Harmans, J.G. Williamson, H. van Houten, C.W.J. Beenakker, C.T. Foxon, and J.J. Harris, *Phys. Rev.* **B** 39, 8040 (1989).

[5.11] L.I. Glazman, G.B. Lesovik, D.E. Khmel'nitskii, and R.I. Shekter, *JETP Lett.* 48, 238 (1988).

[5.12] S.E. Laux, D.J. Frank, and F. Strern, *Surf. Sci.* 196, 101 (1988).

[5.13] R. Landauer, *IBM J. Res. Dev.* 32, 306 (1988).

[5.14] M. Buttiker, *Phys. Rev. Lett.* 57, 1761 (1986).

[5.15] R. Landauer, *IBM J. Res. Dev.* 1, 223 (1957); *Phys. Lett.* 85A, 91 (1981); *J. Phys.: Condens. Matter* 1, 8099 (1989).

[5.16] M. Buttiker, *Phys. Rev. B* 41, 7906 (1990).

[5.17] J. N. L. *Connor, Mol. Phys.* 15, 37 (1968).

[5.18] H. A. Fertig and B. I. Halperin, *Phys. Rev. B* 36, 7969 (1987).

[5.19] Private communications with Professor Paul McEuen (UC Berkeley Physics Department.).

[5.20] U. Meirav, M.A. Kastner, and S.J. Wind, *Phys. Rev. Lett.* 65, 771 (1990).

[5.21] Q. Hu, *Appl. Phys. Lett.* 62, 837 (1993); S. Feng and Q. Hu, *Phys. Rev. B* 48, 5354 (1993).

[5.22] N. S. Wingreen, A.P. Jauho, and Y. Meir, *Phys. Rev. B* 48, 8487 (1993).

[5.23] S. Datta and M. P. Anatram, *Phys. Rev. B* 45, 13761 (1992).

[5.24] F. Hekking and Y. V. Nazarov, *Phys. Rev. B* 44, 11506 (1991).

[5.25] T. Brandes, W. Hausler, K. Jauregui, B. Kramer, and D. Weinmann, *Physica B* 189, 16 (1993).

[5.26] M. Buttiker, A. Pretre, and H. Thomas, *Phys. Rev. Lett.* 70, 4114 (1993).

[5.27] Y. Fu and S.C. Dudley, *Phys. Rev. Lett.* 70, 65 (1993).

[5.28] M. Buttiker and R. Landauer, *Phys. Rev. Lett.* 49, 1739 (1982).

[5.29] E. H. Hauge and J.A. Stovneng, *Rev. Mod. Phys.* **61**, 917 (1989).

## 5.5 Figure Captions

Figure 5.1: (a) Band-bending diagram for GaAs-AlGaAs heterostructure. A high mobility of 2DEG appears at the interface between GaAs and the thin undoped AlGaAs layer (Figure taken from ref. [5.3]). (b) Top view of a typical QPC device. The white region corresponds to 2DEG. A voltage, $V_{sd}$, is applied to the ends and the current is measured through the constriction. A negative voltage is applied to the hashed gates in the center. This depletes electrons near the gate and confines them in the transverse dimension.

Figure 5.2: (a) Conductance vs. gate voltage of a QPC at 0.6 K. Steps are quantized in units of $2e^2/h$ (Fig. from ref. [5.1]). (b) Nonlinear $I_{dc}$-$V_{sd}$ curves of a QPC at 0.6 K taken at different gate voltages near pinch off (Fig. from ref. [5.10]).

Figure 5.3: Potential variation in the longitudinal direction, x, in a QPC. A voltage, $V_{sd} = \mu_1 - \mu_2$ is applied across the junction. $V_0$ is the barrier height and $E_f$ is the Fermi energy.

Figure 5.4: (a) Buttiker-Landauer barrier modulation experiment at low frequency. The barrier height, $V_0$, is modulated at a frequency $\omega$ and amplitude $V_1$. An electron incident at energy, E, is split into three bands separated by $\hbar\omega$. The photon is not absorbed or emitted till after the barrier. (b) Barrier modulation experiment at high frequency. The barrier height, $V_0$, is modulated at a frequency $\omega$ and amplitude $V_1$. An electron incident at energy, E, is split into three bands separated by $\hbar\omega$. For the upper band, the photon is absorbed before the barrier, and for the lower band the photon is emitted after the barrier.

Figure 5.5: Tien-Gordon picture for photoexcitation in the left lead. The left lead is modulated at a frequency $\omega$ and amplitude $V_{L1}$. An electron incident at energy, E, is split into three bands separated by $\hbar\omega$. Photon absorption and emission takes place in the left lead.

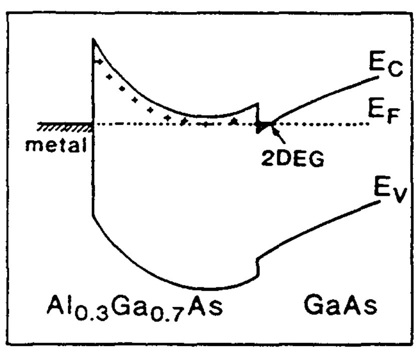


Figure 5.1(a)

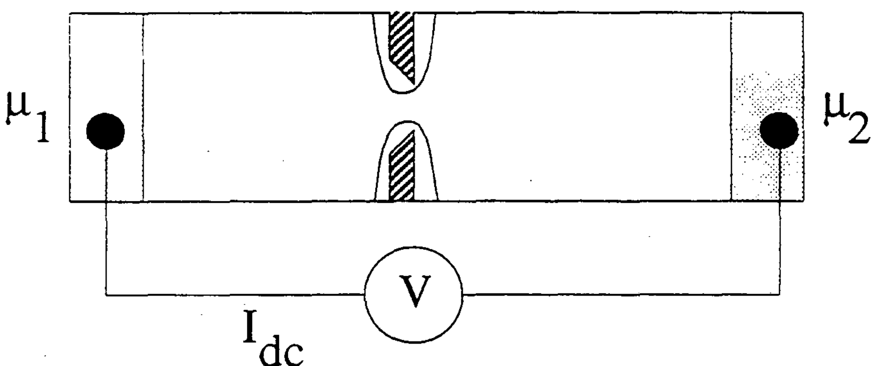


Figure 5.1(b)

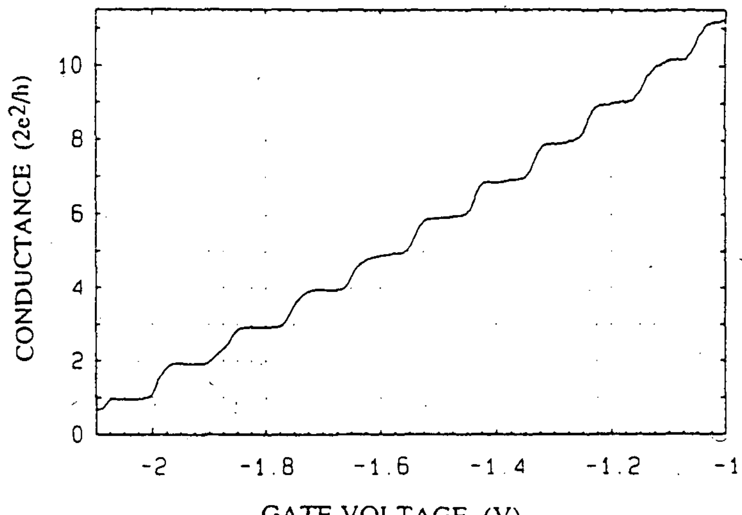


Figure 5.2(a)

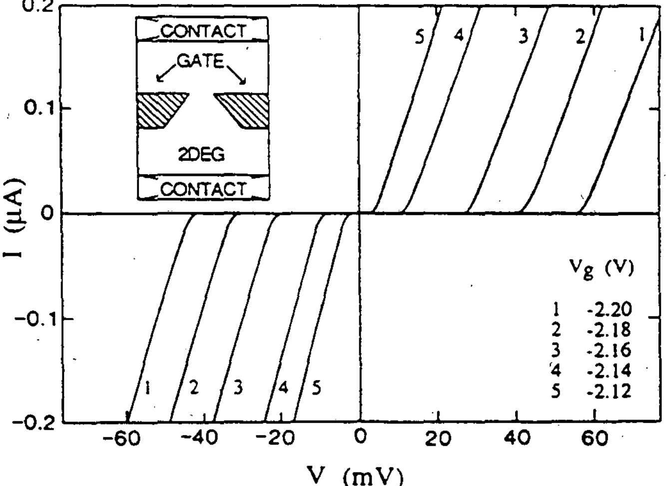


Figure 5.2(b)

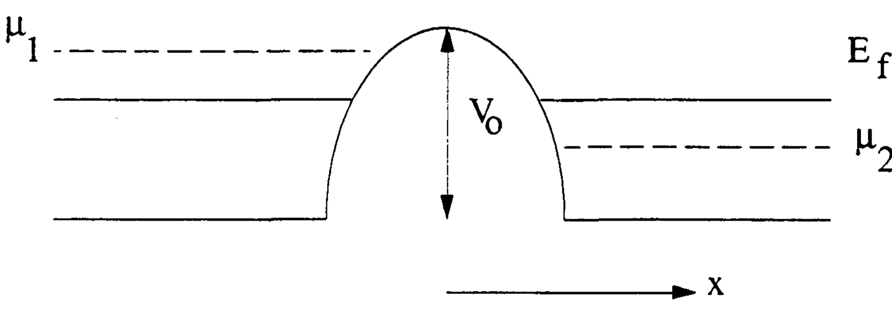


Figure 5.3

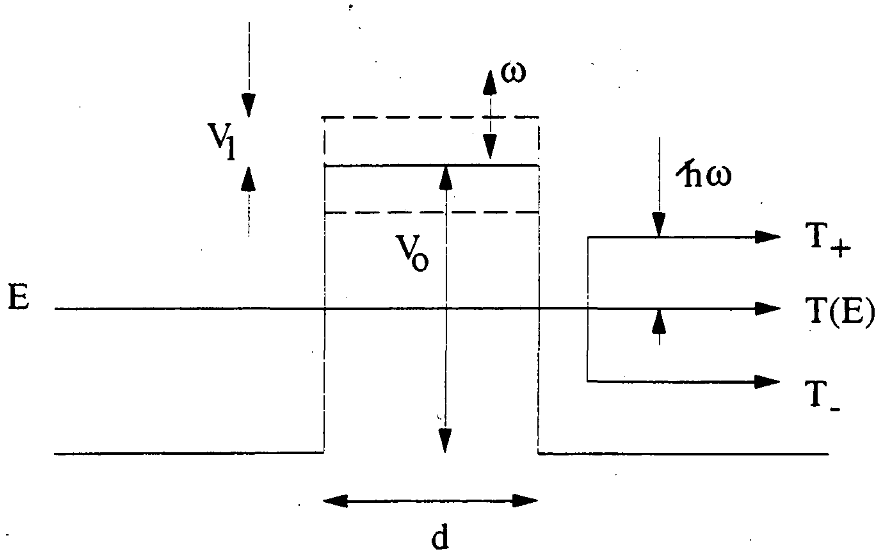


Figure 5.4(a)

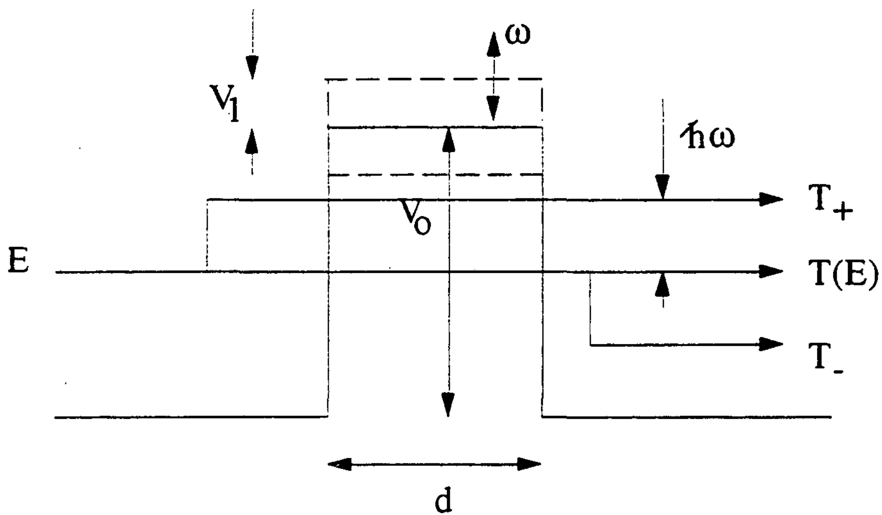


Figure 5.4(b)

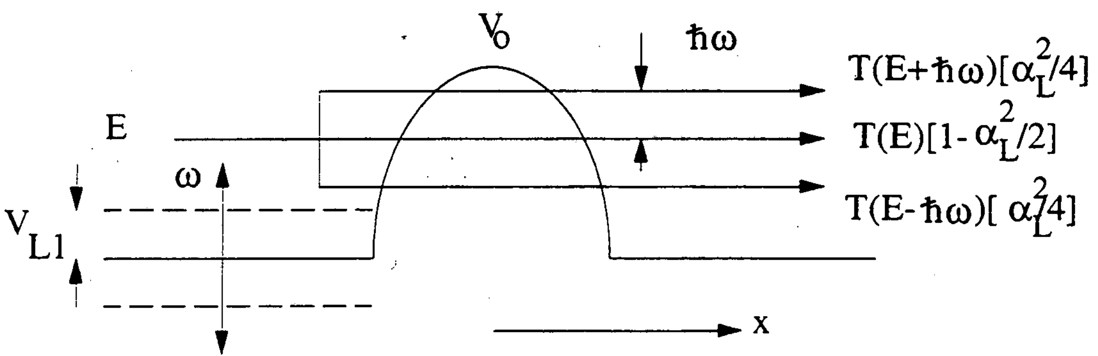


Figure 5.5

# *Chapter 6*

# *The Quantum Point Contact:*

# *High Frequency Transport Experiments*

## 6.1 Introduction

Extensive studies of electronic transport in the quantum regime have led to a deep understanding of the near-zero frequency conductance of mesoscopic structures. The Landauer formula [6.1], relating the conductance to the electron scattering matrix provides a unifying viewpoint for understanding such seemingly diverse phenomena as conductance plateau in the quantum Hall effect [6.2] and transport through narrow constrictions [6.3]. In contrast, we are only beginning to understand the frequency dependent response functions of such structures. Current controversial issues include the tunneling time through a barrier [6.4], and the complex admittance [6.5-6.7] of mesoscopic systems. At sufficiently low frequency, the admittance is real and approximately equal to the zero frequency conductance. The admittance is predicted to become frequency dependent for

photon energies, $\hbar\omega \approx \left|d\ln[t(E)]/dE\right|^{-1}$ where $t(E)$ is the energy-dependent transmission amplitude.

An appealing system for studying the phenomena discussed above are GaAs/AlGaAs heterostructures containing a two-dimensional electron gas (2DEG) beneath the surface. As discussed in Chapter 5, gates on the surface of the heterostructure can be used to create tunnel barriers whose properties can be adjusted by tuning the gate voltage. The conductance of these tunnel barriers, or more commonly known as quantum point contacts (QPCs), is quantized in units of $2e^2/h$ (13 KΩ). *dc* transport measurements of these devices indicate that $|t(E)|^2$ for these barriers varies from exponentially small to near unity on the *meV* scale [6.8]. The crossover to the high-frequency regime is therefore expected to occur at terahertz frequencies.

Although direct measurements of the terahertz admittance are extremely difficult, measurements of the change in *dc* current due to terahertz excitation are relatively straightforward. Such measurements can also reveal the predicted crossover. At low frequencies the induced *dc* current is well described by classical rectification, as in a square-law diode detector, which is *frequency-independent*. Above the crossover frequency the induced current (or "photocurrent") is predicted to be *frequency-dependent*, with high frequencies producing a greater photocurrent than low frequencies. This regime is conventionally termed photon-assisted transport (PAT) [6.9]. PAT processes have been studied extensively in superconducting-insulating-superconducting tunnel junctions [6.9].

In this Chapter we will begin with a brief review of *all* the experiments to our knowledge that attempt to probe the high frequency response of mesoscopic devices. The fact that we can still discuss *all* the experiments in a few short paragraphs emphasizes that this field is still in its infancy. After this discussion we will describe our results using THz-TDI to probe the high frequency response of a single QPC device. These experiments owe their success to a fruitful collaboration between Professor Orenstein's and Professor McEuen's group at UC Berkeley, and Professor Sakaki's group at the University of

Tokyo. In Section 6.2, we will describe a series of preliminary experiments on a QPC. We measured the induced current response, $\Delta I_{dc}(\omega)$, as a continuous function of frequency, source-drain voltage, and magnetic field. The measured spectra were the first to show evidence for PAT in a QPC [6.10]. In addition, the experience that we gained in carrying out these experiments provided us with a number of ideas to improve our experimental technique. In Section 6.3, we will describe a series of highly refined experiments in which we concentrate on measuring the induced current response as a function of frequency, barrier height, and magnetic field [6.11-14]. As with the source-drain experiment, these new measurements also provide strong evidence for PAT.

We now begin with a historical review of the measurements to date of the high frequency response of a single low dimensional tunnel barrier. In 1992, we began an experimental program to measure $\Delta I_{dc}(\omega)$ in a QPC with terahertz pulses. Unknown to us at the time, there had been a group a few years earlier in 1990 at Cambridge [6.15] that had also tried to measure $\Delta I_{dc}$ in a QPC. They quasioptically coupled radiation from a FIR laser at frequencies between 200GHz to 4.2 THz to the device. They concluded that their measured $\Delta I_{dc}$ was due to heating. Concurrent with our work at Berkeley, Hu's group at MIT [6.16] had also begun a program to look for PAT in a QPC. They quasioptically coupled 1 mW of 300 GHz radiation from a Gunn oscillator to a QPC and measured $\Delta I_{dc}$ as a function of barrier height or equivalently gate voltage. Although they were hoping to see PAT, later in 1993 they concluded that the measured $\Delta I_{dc}$ was simply due to heating [6.17] of the 2DEG. By early 1993, we had successfully made the first measurements of $\Delta I_{dc}$ as a continuous function of frequency and source-drain voltage using our terahertz interferometric technique [6.10]. These results were consistent with PAT and will be described in detail in Section 6.2. During this same year, Chemla's group at Berkeley had made the first measurements of the response of the tunneling gap in a scanning tunneling microscope to excitation by subpicosecond electrical pulses [6.18]. They recently showed that the response of the tunneling gap to excitation by a subpicosecond electrical pulse has

a capacitive component, the origin of which is quantum mechanical [6.18]. In 1994 Janssen *et al.* [6.19] presented evidence for classical rectification in a QPC subjected to THz radiation from a far infrared laser. By this time our group at Berkeley had refined our terahertz interferometric technique, and were able to measure $\Delta I_{dc}$ in a QPC as a function of frequency, barrier height, and magnetic field [6.11-14]. These results, like our previous measurements were also consistent with PAT and will be described in Section 6.3.

Concurrent with the search for PAT in quantum point contacts, groups were also looking for PAT in multiple tunnel barrier systems. Kouwenhoven *et al.* in 1994 while at Berkeley began a program to measure the response of a quantum dot [6.20] to microwave signals up to 40 GHz. Their measurements were the first to demonstrate photon-assisted tunneling in a quantum dot [6.21]. Hu's group at MIT has also recently begun to study lateral dual-gate devices. They also report observations of PAT through quantized energy states that result from lateral confinement in a mesoscopic device [6.22]. In addition, van der Weide *et al.* at the Max-Planck-Institute has begun to probe the picosecond response of a quantum dot using an interferometric technique similar to ours [6.23].

As can be seen from the brief review above, the interest in measuring the high frequency response of mesoscopic devices has steadily increased and there appears to be no abatement of interest. As PAT becomes firmly established in mesoscopic devices, we expect experiments to shift their focus from attempting to observe PAT to using PAT as a probe of mesoscopic devices. As we discussed in the Section 5.3, PAT is a more powerful probe of a tunnel barrier than is *dc* transport. In addition, one can use PAT as a probe of the frequency dependent complex admittance of mesoscopic systems in analogy with the experiments on SIS junctions discussed in Chapter 3. Beyond measuring the linear response, interesting nonlinear effects are also expected in quantum dot structures. Wingreen *et al.*[6.24] has predicted the appearance of Rabi oscillations in a quantum dot probed by large amplitude pulses on the picosecond time scale.

## 6.2 The First Terahertz Interferometric Measurements of a QPC

### 6.2.1 QPC Device Fabrication

The QPC device used in this Section was fabricated by Keith Wald at UC Berkeley [6.25]. The device is similar to that depicted in Figure 5.1(b). The structure is implemented in 2DEG confined to a AlGaAs/GaAs heterojunction using techniques similar to those described in Section 5.1.1. The 2DEG had a typical carrier concentration of 2-3x$10^{11}$ $cm^{-2}$ and mobility of 500,000 $cm^2/V$-s at 0.5K. We use a standard Hall bar geometry, with a series of ohmic contacts around the edge which may be used as current injectors or voltage probes. The ohmic contacts were made by annealing an alloy of Au/Ni/Ge to the 2DEG. The Hall bar has a length of 1mm and a width of 100 $\mu$m. The metallic gates are formed with a 500 Å layer of Au on top of a 100 Å Cr layer. The lithographically defined gate separation is 0.3 $\mu$m. All unused gates on the device were grounded to the 2DEG. As a side note, this same device has be used by Professor McEuen's group for NMR studies in a QPC [6.25].

The device is placed inside an optical access, one shot $^3$He, 7 Telsa magnet cryostat from Oxford Instruments. $^3$He gas is condensed in the sample space so that the sample is bathed in liquid $^3$He. A charcoal sorb pumps on the liquid $^3$He, reducing the temperature of the liquid and the sample to 0.5 K The $^3$He hold time for a single run is 12 hours. After 12 hours the sample will warm to 4.2 K and the $^3$He liquid will turn into a gas. The gas must be recondensed to return the sample to 0.5 K. The single shot hold time of 12 hours is sufficient for our terahertz interferometric measurements.

Figures 6.1 and 6.2 show a trace of the conductance of our device at T=0.9 K as a function of gate voltage. The conductance steps appear at multiples of the conductance quantum, $2e^2/h$. The slight deviations from ideal steps is most likely due to scattering at impurities in the vicinity of the QPC or abruptness of the constriction [6.26]. The conductance was found by measuring the source-drain current with a low noise 1211

Ithaco current amplifier in the presence of a 50 μV source-drain voltage. While sweeping the voltage on the gates, the current through the device was measured and the conductance calculated. In Fig. 6.1, the sharp drop off in the conductance for $V_g < 0.6$ V is due to depletion of the 2DEG below the metallic gates. In Fig. 6.2, the series resistance of the 2DEG has been removed by subtracting the conductance at $V_g=0$.

### 6.2.2 Terahertz Detection

Before we could begin our spectroscopic measurements, we first had to prove that we could detect a terahertz induced current, $\Delta I_{dc}$, in our device. At this point in our experimental program, we knew of only one other group that had measured a rectified current signal in a QPC. The MIT group [6.16], had measured a detectable signal in the presence of 300GHz radiation from a Gunn oscillator at a microwave power level of 1 mW. In addition, to improve the coupling of microwave radiation to the QPC, they fabricated the gates into a log periodic antenna ( see Section 4.4). In contrast to a Gunn oscillator, our terahertz pulses are relatively weak with maximum power levels in the range of tens of microwatts. In addition, we did not have a special antenna structure to maximize the amount of microwave power coupled to the QPC. Thus, *a priori*, we had no idea if terahertz interferometric measurements were possible.

For the first experiment, we simply butted a single terahertz antenna/lens source directly in front of the outer window of the optical access cryostat. No parabolas were used to focus the radiation onto the sample. The hope was that the weak collimating properties of the lens would be sufficient to couple radiation onto the sample. The distance between the antenna and the sample was four inches. The beam first passes through a 25 μm Mylar room temperature window followed by two cold quartz windows one at 77 K and the other at 4.2 K. These windows, of thickness 6 and 9 mm, respectively, are required for blocking thermal radiation and allow the sample to reach the requisite temperature of 0.5 K. The beam finally enters the $^3$He sample cell through a 125 μm

Mylar window. The use of windows that are either much thinner or much thicker that the pulse length eliminates reflections that might otherwise contaminate future terahertz interferometric measurements. As described previously, the sample rests immersed in superfluid $^3$He. The superfluid is quiescent, eliminating the possibility of bubbles causing instabilities in the device and in beam propagation. We expected radiation to be coupled to the QPC by the metallic gate electrodes. To maximize the coupling to the gate electrodes, we made sure that the terahertz radiation was polarized along the gates.

Fortunately, the crude coupling scheme described above was sufficient to generate a measurable $\Delta I_{dc}$. Figure 6.3 show the first measurements to our knowledge of terahertz pulse detection using a QPC (9/10/92) . The step like curve is a measure of the *dc* current through the QPC as a function of gate voltage in the presence of 1 mV source-drain bias voltage. The bipolar signal is $\Delta I_{dc}$. The multiple curves correspond to different terahertz power levels. This signal was multiplied by a factor of 1000 so that it can be put on the same scale with $I_{dc}$. We measure $\Delta I_{dc}$ with the following procedure. First the laser beam which is injected into the terahertz source is mechanically chopped at 1 KHz. Next the component of the *dc* current in the QPC which is synchronous at 1 KHz is detected with a PAR 124A lock-in. $\Delta I_{dc}$ is then measured as a function of gate voltage. The most important features of $\Delta I_{dc}$ is that the signal is bipolar and concentrated near the onset of the conductance steps. These data have features similar to what we found for the SIS tunnel junction in Fig. 4.5. We know from Chapter 5 that the conductance steps appear at those gate voltages when the barrier height in the channel is near the Fermi energy. From the PAT picture, one would expect the largest photocurrent signal when the barrier is within a photon energy of the Fermi level. We will show in Section 6.3.5 that $\Delta I_{dc}$ should look bipolar for gate voltage modulation.

### 6.2.3 Terahertz Spectroscopy-Source/Drain Experiment-Zero Magnetic Field

At this point, we cannot draw any conclusions as to the origin of the measured induced current signal. The difficulty is that there are a number of ways a rectified current can be induced in a nonlinear device in the presence of terahertz radiation. One way to obtain a rectified current is classical rectification [6.19]. It is also possible to obtain a bolometric signal which looks like Fig. 6.3 [6.17]. How one can distinguish between these different phenomena, classical rectification, heating, and PAT? The answer is to *measure $\Delta I_{dc}$ as a function of frequency.*

In Chapter 5, we have discussed various theories of PAT that predict that $\Delta I_{dc}$ will become frequency dependent at sufficiently high frequencies. In addition, the Tien-Gordon approach specifically predicts a threshold for photon absorption, $\omega_c = (E_0 - E_f - emV_{sd})/\hbar$, where $E_0 = eV_0$ is the $V_g$ dependent barrier height and $V_{sd}$ is the applied source-drain bias. Thus one possible experimental program to search for PAT is to measure the rectified current as a function of frequency and then look for a threshold that varies in the proper way as a function of $V_{sd}$ and $V_g$. For example, when $E_0 > E_f$, the threshold for absorption should decrease as $V_{sd}$ is increased. On the other hand, classical rectification and heating is not expected to have the same $\omega$, $V_{sd}$, and $V_g$ dependence as PAT. We will discuss the issue of heating further at the end of this Section.

To measure the frequency dependence of $\Delta I_{dc}$ we use the terahertz interferometric technique described in Chapter 2. The interferometer we use is similar in concept to the interferometer in Fig. 2.9. The only difference is that we have used a single antenna (#1) as a source as opposed to two separate antenna sources. We have taken laser beam #2 and diverted it into antenna #1. Thus antenna #1 is pulsed by two separate laser beams. To eliminate any interference at the photoconductive switch, the polarization of the first laser beam is rotated by 90 degrees with respect to the second laser beam. Each pulse will generate its own separate terahertz pulse. The time delay between these terahertz pulses can be varied by changing the time delay, $\tau$, between the two laser pulses. There are a number of obvious advantages of this interferometer over the earlier version in Fig. 2.9. The first

is that no beam splitter is needed since the terahertz pulses comes from the same source. This means that we need not be concerned with the frequency dependence of the Mylar beam splitter and its associated losses. In addition, our interferograms will be perfectly symmetric since the two terahertz pulses will be identical. A second advantage of this technique is that spectrometer is *automatically aligned.* Since the pulses come from the same source, they will travel the identical beam path and will interfere perfectly on the QPC.

The only disadvantage of pulsing the same antenna twice is that it is possible to saturate the photoconductive Auston switch with the two laser pulses when the pulse intensity is too high. Ideally, without saturation, the average power in the terahertz beam should be twice as large at zero time delay relative to large time delays. However, with saturation the average power at zero time delay will be less than twice the average power at large time delays. To minimize saturation effects we kept the laser power low at 20 mW in each beam. In addition, we can measure the degree of saturation by monitoring the photocurrent in the photoconductive switch as a function of time delay, $\tau$. Saturation effects will appear as a depression in the photocurrent near $\tau=0$. We verified that the photocurrent near $\tau=0$ dropped by less than 10% relative to photocurrent at large $\tau$.

We decided to probe the rectified current in the QPC as a function of source-drain voltage, $V_{sd}$, in analogy with the earlier SIS experiments described in Chapter 4. The inset in Figure 6.4 shows the $I_{dc} - V_{sd}$ curve for the point contact in the presence of a large negative gate voltage ($V_g$=-1.936V) such that very little current flowed for $V_{sd}$<1mV. This corresponds to the regime where $V_0 >> E_f$. The $I_{dc} - V_{sd}$ characteristic shows a pronounced nonlinearity in this range of bias voltages from 2 to 5 mV. The physical origin of this nonlinearity was discussed in Chapter 5. Refer once again to Figure 5.3. At small $V_{sd}$ ($V_{sd}=\mu_1-\mu_2$), the device is pinched off and no current can flow. As $V_{sd}$ is increased, eventually electrons in the left lead will have sufficient energy to surmount the barrier and there will be a large onset in the current flow.

Like the *dc* current, the rectified current in the QPC also depends strongly on $V_{sd}$. From classical mixing theory (see Section 2.6.3), one would expect the rectified current to be a maximum near the nonlinear portion of the $I_{dc} - V_{sd}$ curve. Indeed, we do find that the rectified current is a maximum at the kink in the $I_{dc} - V_{sd}$ curve at $V_{sd}$=4.6 mV. The rectified current drops off sharply as the bias is moved away from 4.6 mV. The rectified current in the QPC due to a single antenna source had a maximum value of 30 pA and a noise level of 200 fA in a 1 Hz bandwidth at a chopping frequency of 1 KHz.

The main part of Fig. 6.4 shows typical curves of $\Delta I_{dc}$ vs. $\tau$ for two values of $V_{sd}$ labeled **(a)** and **(b)** in the inset. Notice that the interferograms are perfectly symmetric as expected. The difference in the two interferograms illustrates that the dynamic response of the QPC depends dramatically on $V_{sd}$ in this regime. To analyze the interferograms, we Fourier transform $\Delta I_{dc}(\tau)$ to obtain $\Delta I_{dc}(\omega)$. In addition, we remove the influence of the power spectrum of the incident pulses by normalizing each Fourier transform to the spectrum at a single value of $V_{sd}$. Figure 6.5 shows the spectra which result form this normalization procedure. Again, the inset shows the nonlinear $I_{dc} - V_{sd}$ curve and indicates the values of $V_{sd}$ (2.7, 3.5, 4.0, and 4.6 mV) at which the spectra were acquired. Each transform was normalized to the spectrum at $V_{sd}$=5.0 mV (shown as the open circle in the inset).

The change in the spectra as a function of $V_{sd}$ provide strong evidence that the rectified current is photonic rather than bolometric in origin. As $V_{sd}$ decreases and the difference between the Fermi level in the left lead and the barrier height increases and the onset in the rectified current shifts systematically to higher frequency as expected for photon assisted transport. These data are the first to our knowledge to show evidence for PAT in a QPC (2/28/93). The bolometric current, which is proportional to the power dissipated in the 2DEG is not expected to depend strongly on the height of the barrier.

The arrows in Fig. 6.5 indicate the approximate onset frequency, $\omega_c$, for each $V_{sd}$. As $eV_{sd}$ is raised from 2.7 to 4.6 meV, $\omega_c$ shifts by about 100 GHz. This may seem

surprising at first since in analogy with the SIS junction one would expect a frequency shift of $\Delta(eV_{sd})/h$. This corresponds to a expected shift in the threshold frequency of 460 GHz. To understand our results we must recall from our discussions in Chapter 5 that $\Delta(\hbar\omega_c)=m\Delta(eV_{sd})$ (see equation {5.25}), where m=1/2 for a symmetric barrier. From our *ac* transport data, we find that m=0.22. We can compare this to an estimate for m from the *dc* transport data in the inset of Fig. 6.4. The differential conductance for $V_{sd}$>7mV is 1/60 Kohms. From equation {5.11b}, the m factor is equal to differential conductance divided by the $2e^2/h$ (13 Khoms). Thus from the *dc* transport, we find m=0.22. This is in excellent agreement with the *ac* transport results.

One might be tempted to extract a traversal time from the data in Fig. 6.5. We know that if we are modulating the electron energy in the leads as in Tien-Gordon picture, then the onset in the $\Delta I_{dc}(\omega)$ will be broadened by $1/\tau_t$ where $\tau_t$ is the traversal time. Unfortunately it is not possible from this data to know if we are modulating the electron energy in the leads or modulating the barrier as in the Buttiker-Landauer picture. In all likelihood, we are probably modulating both the barrier and the leads. In which case, there is no theory for what the $\Delta I_{dc}(\omega)$ should look like.

Now we will discuss the possibility that the photocurrent spectra is due to either heating or classical rectification and not to PAT. For any square law or power detector, we can write in general that the induced current,

$$\Delta I_{dc}(\omega)=A(\omega)P_A(\omega), \qquad \{6.1\}$$

where $P_A(\omega)$ is the power absorbed in the detector and $A(\omega)$ is a frequency dependent absorptivity. The power absorbed in the device is not necessarily the power incident on the detector. In general, $P_A(\omega)=C(\omega)P_i(\omega)$, where $C(\omega)$ is a coupling coefficient and $P_i(\omega)$ is the incident power. $C(\omega)$ will depend on the admittance of the detector and the network the detector is imbedded in. We discussed such a situation in Section 2.6.3. Thus in terms of the incident power,

$$\Delta I_{dc}(\omega)=A(\omega)C(\omega)P_i(\omega). \qquad \{6.2\}$$

For either heating or classical rectification, $A(\omega)$ is not expected to be frequency dependent. Thus to explain the observed spectral shifts in the spectra of Fig. 6.5, one would need to assume that $C(\omega)$ changes in just the right way with $V_{sd}$ to mimic the observed spectral shifts. This is highly unlikely. Obviously this is not a proof that the observed spectral shifts are due to PAT.

To prove that $\Delta I_{dc}$ is absolutely due to PAT, one would need to know exactly the admittance of detector and imbedding matrix. This is nearly impossible to do since there are a large number of parasitic reactances. In addition, our coupling to the device is not well defined since we are applying the terahertz radiation to the entire sample, not just to the QPC region. Furthermore, we also need to know how the reactances depend on $V_{sd}$. This is a non-trivial problem. For example we know that the capacitance across the QPC junction will depend on $V_{sd}$ [6.27] in a nontrivial way. In addition, in a analogy with the SIS junction we would also expect the intrinsic quantum admittance of the QPC to depend on $V_{sd}$. Unfortunately we do not have a theory for the quantum admittance of a QPC. Given all these difficulties, it is clear that attempting to compute $C(\omega,V_{sd})$ is not practical at this stage.

A more pragmatic approach than trying to compute $C(\omega,V_{sd})$ is to accept the fact that our technique can only give evidence for PAT. This evidence can be made stronger if the correct spectral shifts are seen in a number of different experiments. In this experiment, we have seen the correct shift as a function of $V_{sd}$. In Section 6.3 we will discuss another experiment on a completely different device. On that device we study changes in the spectral response as a function $V_g$ over a large range of barrier heights. In addition, that device was studied in a magnetic field. In all cases we see spectral shifts that correlate well with what is expected from the *dc* transport data. All these data taken as a whole present strong evidence for PAT in these QPC structures.

### 6.2.4 Terahertz Spectroscopy-Magnetic Field Dependence

The experiments in the previous Section all took place at zero magnetic field. We decided to make some preliminary measurements of the spectra as a function of field. The first step was to choose an operating point for $V_{sd}$. We chose $V_{sd}$=4.6 mV since that is the bias voltage that gave us the maximum rectified current. Figure 6.6 shows interferograms for B=0 T and 0.2 T. As is clear from these traces, there is large change in the response for very small changes in field. In order to investigate these change further we made measurements at a number of magnetic field points up to 0.7 T. To analyze these data, we took the Fourier transforms of the interferograms at different magnetic fields. From these Fourier transforms, we can plot $\Delta I_{dc}$ as a function of magnetic fields for different frequencies. These data are plotted explicitly in Figure 6.7 for the frequencies, 110, 150, and 170 GHz. $\Delta I_{dc}$ peaks at a definite magnetic field for each of the different frequencies. In addition, the peak moves to higher field as the frequency is raised.

In the inset we plot the peak frequency as a function of magnetic field. From this dispersion relation, it was clear to us that we were seeing the bulk magnetoplasmon excitation of the 2DEG. The magnetoplasmon dispersion relation for a GaAs 2DEG is expected to be, $\omega_p^2 = \omega_{p0}^2 + \omega_c^2$, where $\omega_{p0}$ and $\omega_c$ are the 2D plasmon and cyclotron frequency respectively [6.28]. The dashed curve in the inset of Fig. 6.7 is a fit to this relation. The frequency $\omega_{p0}$ for a 2D plasmon in an infinitely large 2DEG is given by [6.29],

$$\omega_{p0}^2 = \frac{N_s e^2}{2\varepsilon_{eff}\varepsilon_0 m^*} k \ , \qquad \{6.3\}$$

where $\varepsilon_{eff}$ is the effective dielectric constant, k is the wave vector for the plasmon, and $N_s$ is the 2D electron density. $\varepsilon_{eff}$ can be well approximated by $\varepsilon_{eff} = (\varepsilon_{GaAs} + \varepsilon_{vac})/2$. This approximation is valid when 1/k is large compared to the AlGaAs and the GaAs cap layer which is true for our devices. For $\varepsilon_{GaAs}$=12.8 we find that $\varepsilon_{eff}$=6.9. To measure the carrier

density, $N_s$, we use the Shubnikov-De Hass technique [6.1]. We find that our 2DEG had a typical $N_s$ of $2-3\times10^{11}cm^{-2}$. $N_s$ is stable at low temperatures, but can be changed by illumination with optical radiation [6.30] or by thermally cycling the device. Unfortunately for this experiment, we did not measure the carrier density soon after the experiment so we can only estimate that $N_s \approx 2.5\times10^{11}cm^{-2}$. Next we have to choose the proper k for the plasmons in our Hall bar. Since we do not have an infinite 2DEG, we assume that the edges of the Hall bar will determine the appropriate k vectors for plasmon excitations. Since our terahertz radiation is polarized along the short direction of the Hall bar, we assume that we are exciting plasmons along that same direction. The lowest plasmon mode will have a k vector such that half a wavelength will fit into the width, w, of the Hall bar. In this case, $k=\pi/w$. From the inset in Fig. 6.7 we see that the experimentally measured plasmon frequency is 75 GHz. From this value for the plasmon frequency and the above relations we find that w=115 μm. This number is in close agreement with the 100 μm etched width of the Hall bar. The small discrepancy may be attributed to fact that we do not have an exact measure for the carrier density in this experiment.

### 6.2.5 Conclusions

Obviously, we would have liked to do many more experiments on this device to support our hypothesis that we have seen PAT. Unfortunately, we blew out the device shortly after completing the experiments described above. One of the most important experiments would have been to measure the gate voltage dependence of the interferograms and see if they correlated with the PAT model. A second important experiment would have been to repeat the measurements of the interferograms as a function of source-drain voltage in a 1 T magnetic field. At this field, the magnetoplasmon would be outside of our frequency range. If we still had seen similar spectral shifts as in Fig. 6.6, we could rule out the possibility that the spectral shifts are caused by a source-drain voltage dependent magnetoplasmon frequency. In the next Section, we will describe a second series of highly

refined experiments on a new type of device where we do perform the experiments described above.

## 6.3 Terahertz Interferometric Measurements of a Mesoscopic Tunnel Barrier

The experiments of the previous Section are important for a number of reasons. First those experiments proved that the terahertz interferometric is a viable method to measure the dynamic response of a QPC. In addition, we found nontrivial effects in the induced current response, that is evidence for PAT. Nevertheless, those measurements were preliminary, and left much to be desired in terms of experimental finesse. The modifications we will describe in this Section have allowed us to make high quality measurements which give even stronger support that the induced current response is due to PAT [6.11-6.14]. We will first describe the new version of the terahertz spectrometer which employs a wire grid beam splitter which has a number of advantages over the Mylar beam splitter technique. Next we will cover a novel antenna-transmission line scheme to couple to the device. This technique insures that *ac* potentials are applied to the tunnel barrier in a controlled manner. Lastly we will describe our new device. This device is slightly different than the standard QPC, and thus we will refer to it as a mesoscopic tunnel barrier or tunnel barrier for short. The advantages of this device is that *ac* potentials can be applied solely to the barrier region and not to the entire 2DEG. After discussing these important modifications in the experimental method, we will describe the new series of experiments. We will begin by taking a look at the rectified current generated by a single voltage pulse. Next we will apply the terahertz interferometric technique to measure $\Delta I_{dc}$ as a function of frequency, barrier height, and magnetic field.

### 6.3.1 Improved Terahertz Spectrometer

In contrast to the experiments described in the previous Section, we have decided to return to an interferometer configuration similar to the SIS interferometer in Fig. 2.9, rather than pulse a single antenna twice. Although pulsing a single antenna twice has a number of advantages in terms of alignment, it has one major disadvantage in that the laser power must be kept low on the photoconductive switches to minimize saturation effects. This limits the maximum power available from the antennas and reduces the over all dynamic range of the system.

A diagram of the new spectrometer is shown in Figure 6.8. The pulsed source is the same photoconductive Auston switch [6.31] coupled to a 300 μm dipole antenna [6.32], described in Chapter 2. The antenna source radiates when excited with a mode-locked Ti:sapphire laser. The emitted pulse is a nearly single cycle of electric field with an approximate period of 5 ps. The power spectrum of the pulse has a center frequency of 180 GHz and a 3 dB bandwidth of 80 GHz. To study $\Delta I_{dc}$ *vs.* $\omega$ we measure the *dc* current induced by two pulse trains as a function of their relative arrival time $\tau$. As depicted schematically in Fig. 6.8, the two-pulse beam is formed by combining the radiation from a pair of antennas using a wire grid beamsplitter.

The wire grid has a number of advantages over the earlier version of the SIS spectrometer which employed a Mylar beam splitter. The most significant advantage is less frequency dependence of the reflection and transmission coefficients, which is important for broadband measurements. In addition, the ideal throughput of the interferometer increases from 50% for a reflection beamsplitter to 100% for the polarizing beamsplitter. The configuration of the polarizers to achieve optimum coupling is as follows: the two antennas are aligned at 45° with respect to the horizontal. The axis of the beamsplitter is adjusted to transmit the pulse from (A) and reflect the pulse from (B). The combined beam contains two pulse trains with orthogonal polarizations. An additional polarizer (P) between the beamsplitter and the sample selects either horizontal or vertical polarizations for excitation of the device. A final f/3 parabolic mirror focuses the combined beam onto the

sample through a number of windows in a $^3$He, 7 Tesla magnet cryostat. The configuration of the cryostat is the same as described above in Section 6.2.1. As before, the sample rests immersed in superfluid $^3$He at 0.5 K.

### 6.3.2 Antenna-Transmission Line Coupling

One of the weakest features of the experimental method described in Section 6.2 is that the coupling of the voltage pulses to the gates of the device is uncontrolled. In the earlier experiments, radiation incident on the sample can excite both the gate electrodes and the 2DEG. Strong excitation of the 2DEG can lead to heating which is undesirable. We would rather have a method which can selectively excite the gates only. In addition, we want a method of coupling that will work in general with multiterminal devices such as quantum dots or coupled dots [6.20]. It would be highly undesirable to excite all the electrodes of such a structure in a random manner. Such an experiment would be too difficult to analyze.

To avoid these difficulties we have devised a technique that ensures that the *ac* potentials are applied to the tunnel barrier in a controlled manner. Figure 6.9 shows our scheme for coupling terahertz radiation to a single tunnel barrier. Our device actually consists of four tunnel barriers which can be used to form a quantum dot [6.33]. We will describe this device further in the next Section. For now, though, our goal is to excite only one of the tunnel barriers. The antenna/transmission line chip and tunnel barrier chip are both mounted in a standard 16 pin carrier (not shown). The chip carrier is secured to a brass holder which prevents terahertz radiation from directly falling on the device and exciting the device in an uncontrolled manner. To reach the tunnel barrier incident radiation must first pass through a small hole in the brass holder fitted with a 4 mm diameter hyperhemispherical silicon lens. The silicon lens focuses the beam onto a 600 μm dipole antenna designed to resonate at approximately 90 GHz. Due to the wide bandwidth of dipole antennas, substantial overlap remains between the picosecond pulses centered at

180 GHz and the receiving antenna centered at 90 GHz. The advantage of this design is that the power coupled to the antenna will be relatively evenly distributed from 90 to 180 GHz.

From the antenna, the pulses are coupled to a coplanar transmission line (CTL). Both the antenna and transmission line consist of 0.8 μm thick aluminum evaporated onto a single 0.5 mm thick sapphire substrate as described in Section 2.2. The antenna and the transmission line dimensions were chosen to maximize the coupling from the antenna to the transmission line. Kominami *et al.* [6.34] has calculated the resonant resistance of a dipole antenna on a semi-infinite substrate as function of substrate permittivity. The antenna and the transmission line are oriented on the sapphire chip such that only the ordinary ray in sapphire is excited. The ordinary ray has a permittivity of 9.4 in this frequency range. For this permittivity, the resonant resistance of the antenna is only 40 Ω. It is difficult to design a CTL with this low an impedance. If W is the width of a one of the transmission lines and s is the spacing between the lines, then according to calculations by Wen [6.35] , if s=W then the impedance of the line is 90 Ω which is much larger than our antenna resistance. To lower the impedance of the line, we must reduce the ratio,

$$s/(s+2W). \qquad \{6.4\}$$

Obviously making s small will reduce this ratio. Although it is possible to make s smaller than a 1 μm with optical lithography, we decided not to push the limits of optical lithography and set s=4 μm. The ratio in equation {6.4} can also be made small by making W large. We do not want to make W too large because this would lead to large radiation losses as the pulse propagates down the transmission line. According to Frankel *et al.* [6.36] the wavelength dependent attenuation, A(λ), on a CTL in a distance λ is proportional to,

$$A(\lambda) \propto \left( \frac{s+2W}{\lambda_0 / n_{eff}} \right)^2, \qquad \{6.5\}$$

where $\lambda_0$ is the free space index and $n_{eff}$ is the effective index of refraction. $n_{eff}$ is defined to be the square root of the average dielectric constant of air and sapphire. As expected, the attenuation is greatest at short wavelengths and on wide transmission lines. Intuitively, once the wavelength approaches the dimensions of the transmission line, the line ceases to guide the wave and the CTL begins to look like an antenna which can radiate. If we assume that the highest frequency of interest is 200GHz, then the effective wavelength, $\lambda_0/n_{eff}$=650 μm. To minimize the radiation losses, we choose W=60 μm which is small compared to $\lambda_0/n_{eff}$. For these dimension, the CTL has a impedance of 50 Ω [6.35] which is well matched to the antenna impedance on resonance. Once the pulse is coupled onto the line, it propagates 5 mm to the end of the transmission line on the antenna chip. At this point it hops onto the QPC chip *via* 100 μm long gold wire bonds and excites a *single* gate.

### 6.3.3 Device Under Study

The tunnel barrier we have studied differs somewhat from the split gate QPC. Figure 6.10 shows a scanning electron micrograph of the device [6.37] used in our experiments. In the region of interest, two narrow channels defined by wet shallow etching [6.38], on a selectively doped n-$Al_{0.3}Ga_{0.7}As$/GaAs heterojunction of width 460 nm, intersect to form a cross. The thickness of the undoped AlGaAs spacer, the n-AlGaAs doped layer, and the undoped GaAs cap layer are 30, 70, and 10 nm respectively. Due to depletion of electrons at the edges, the effective channel width is reduced to nearly 60 nm. The narrow channel grows into a narrow wire 10 μm in length, beyond which it widens into large millimeter scale 2DEG regions. The full length of the large cross is 1.3 mm. The 2DEG is characterized by a mobility of 800,000 $cm^2/V$-s at 4.2 K and density 1.6 x $10^{11}$ $cm^{-2}$. The density was found from measurements of the Shubnikov-De Hass oscillations in $\rho_{xx}$. These measurements were done right after the terahertz

interferometric experiments. Ohmic contacts were made to the large 2DEG regions by alloying In-Sn in an argon atmosphere at 400°C for a few minutes.

In contrast to the split gate QPC, each channel of our device has a gate which overlaps its entire width. The gates of width 230 nm were fabricated by depositing locally a NiCr(5 nm)/Au(50 nm) film with lift-off techniques. Application of a negative voltage to a gate generates a barrier for electron propagation. With four gates, the structure may be configured for a wide variety of experiments including demonstration of Coulomb blockade oscillations and turnstile operation [6.37]. To date, we have studied the high-frequency response of the device with only one gate active, forming a single tunnel barrier. The other three gates were held at ground. In the future, activating all four gates will allow us to study the high-frequency response of a quantum dot.

The main advantage of the new device over the standard QPC device depicted in Fig. 5.1(b) is that the gate only overlaps the 2DEG where it is needed to form the tunnel barrier. Thus when an *ac* voltage is applied to the gate, the *ac* voltage only couples to the 2DEG in the region of the tunnel barrier. This *ac* voltage can lead to PAT. In sharp contrast, the gates in Fig. 5.1(b) overlap the 2DEG over a large region far away from the tunnel barrier that actually forms the QPC. Thus when an *ac* voltage is coupled to the gate, the 2DEG will be excited at a distance far from the QPC . These excitations will only lead to heating of the 2DEG. Only the small fraction of the full *ac* signal that is coupled to the QPC region will be available for PAT.

### 6.3.4 *dc* Transport

As shown in Fig. 6.9, the high-frequency voltage is applied across the QPC *via* gate (A) and ohmic contact (1) to the electron gas. In addition to the *ac* input, the QPC is biased at 100 μV through "source" and "drain" ohmic contacts (1) and (2). A negative voltage applied to the gate creates a tunable barrier, $E_0$.

The solid curve in Figure 6.11(a) shows a typical trace of the *dc* current flowing from source to drain $I_{dc}$, as a function of gate voltage $V_g$, for an applied bias $V_{sd}$ of 100 μV. There is a sharp increase in conductance when $-V_g$ drops below approximately 750 mV. The curves of $I_{dc}$ *vs.* $V_g$ near the onset of conductance differ from device to device, and the same device will have different behavior depending on history of temperature cycling and visible light exposure. In general these devices do not exhibit the quantized conductance steps of size $2e^2/h$ seen in QPC's formed by split gates [6.3]. We attribute the absence of conductance steps to electron back scattering in the channel leading to a breakdown of the conductance quantization.

### 6.3.5 Single Pulse Experiment

Before considering the interferometric response, we first discuss the rectified current created by individual voltage pulses. We define the "induced current," $\Delta I_{dc}$, as the additional *dc* current flowing from source to drain when the device is irradiated with a train of pulses. To measure $\Delta I_{dc}$, the laser beam which generates the terahertz pulses is mechanically chopped at 100 Hz and the synchronous source to drain current is detected with a current and lock-in amplifier.

The dashed curve in Fig. 6.11 shows $\Delta I_{dc}$ *vs.* $V_g$ under the same experimental conditions as the solid curve of $I_{dc}$ *vs.* $V_g$. There is a sharp increase in the induced current near the value of $V_g$ at which the channel becomes conducting. The induced current is localized to the region near the onset of conductance with little induced current at zero gate voltage. In addition there is an induced current signal at $V_g = -300$ mV. This signal is also due to a change in the channel conductance. A close inspection of $I_{dc}$ *vs.* $V_g$ reveals that there is indeed a small step in the conductance at $V_g \approx -300$ mV. For the purposes of this paper we will confine our discussion to the induced current peak at $V_g \approx -700$ mV.

An initially unexpected feature is that the induced current is unipolar and it does not depend on $V_{sd}$ for $|V_{sd}|<100$ μV. Assuming that the gate voltage oscillates symmetrically

about its *dc* value, both the quasistatic and quantum models [6.39] predict that the induced current is bipolar in the neighborhood of the conductance onset. This is exactly what was seen in the first series of experiments on the QPC device in Fig. 6.3. To see explicitly how classical modulation of the gate leads to a bipolar signal, we need the Landauer formula (equation {5.5}),

$$I_{dc} = \frac{2e^2}{h} T(V_g) V_{sd}, \qquad \{6.6\}$$

for the current through the lowest mode of the constriction. $T(V_g)$ is given by equation {5.6} with n=1 and $E=E_f$. In the presence of an oscillating gate voltage, $V_g = V_{g0} + V_{g\omega}\cos(\omega t)$, the rectified current is given by,

$$\Delta I_{dc} = \frac{e^2}{2h} V_{sd} \frac{\partial^2 T(V_g)}{\partial V_g^2} \left|V_{g\omega}\right|^2 \ . \qquad \{6.7\}$$

This is entirely analogous to equation {2.7} found in Section 2.6.3 for diode rectification. Since the $T(V_g)$ is similar to the Fermi function (broadened step), the second derivative will look bipolar as in the data of Fig. 6.3. The fact that our data is unipolar implies that the rectified current cannot be due to an oscillating gate voltage and must come from a source-drain modulation.

One important clue as to the origin of the rectified current, is the fact that we obtain the same rectified current signal, even when zero bias is placed across the junction. There are only two possible ways to obtain a rectified current for the zero bias case. One possibility is that the barrier potential, V(x), must break inversion symmetry. In this case an *ac* voltage applied across the source drain contacts will lead to a rectified current [6.40]. This is entirely analogous to a P-N junction diode which can also rectify an *ac* signal due to a built in electric field at the junction between the P-type and N-type semiconductor [6.40]. The other possibility is that the *ac* signal which is applied to the gate couples differently to the two sides of the tunnel barrier. Recall in Chapter 5, equation {5.22}, we derived an expression for the photon induced rectified current in the presence of a source drain

modulation. As expected, the rectified current goes to zero in the zero bias case. But if the *ac* signal only couples to left side of the barrier, we can use equation {5.20},

$$\Delta I_{dc} = \frac{e\alpha^2}{2h}\int_0^{E_f} T(E+\hbar\omega)+T(E-\hbar\omega)-2T(E)dE, \qquad \{6.8\}$$

for the rectified current at zero source-drain bias. Here $\alpha=eV_\omega/\hbar\omega$, where $V_\omega$ is the strength of the *ac* signal that is coupled to the left side of the barrier from the gate electrode. The term in the integral is just the finite second difference of T(E). Since T(E) looks like a broadened step, the finite second difference will look bipolar. The integral of a bipolar function will be unipolar, thus $\Delta I_{dc}$ will be unipolar which is exactly what is observed in Fig. 6.11. We can show this explicitly by considering the case where $\hbar\omega$ is small compared to the energy scale for the nonlinearity in T(E). In this case the rectified current is given by,

$$\Delta I_{dc} = \frac{e^2}{2h}\frac{e\partial T}{\partial E}\bigg|_{E_f} V_\omega^2 \quad . \qquad \{6.9\}$$

Since $\Delta I_{dc}$ is proportional to first derivative of T(E), it will look unipolar as seen in the data.

*dc* transport measurements of the $I_{dc}$-$V_{sd}$ curves of our device indicate the tunnel barrier is relatively symmetric, that is $I_{dc}(+V_{sd})=I_{dc}(-V_{sd})$. Thus our rectified signal is most likely due to an asymmetry in the coupling of the *ac* voltage to the leads. This means that we can fit our spectral data with the Tien-Gordon theory for PAT as in equation {6.8}. At this point we can only postulate an explanation for the asymmetry in the coupling to the two sides of the tunnel barrier. From Fig. 6.10 we see that the gate electrode is near the cross region of the 2DEG. Since the shape of the 2DEG is different on the two sides of the barrier, the coupling from the gate to the 2DEG might be expected to be different.

### 6.3.6 Terahertz Interferometry-Gate Voltage Experiment-Zero Magnetic Field

Excitation of the tunnel barrier with a single pulse yields a *dc* current whose magnitude is an average of the response over the spectral range spanned by the pulse. As mentioned previously, the spectrum of $\Delta I_{dc}$ vs. $\omega$ can be measured by time-domain interferometry. To determine $\Delta I_{dc}$ we measure the current, $\Delta I_{dc}(\tau)$, generated by a pair of pulses as a function of the time delay, $\tau$, between them. $\Delta I_{dc}(\omega)$ is then simply obtained from the Fourier transform of $\Delta I_{dc}(\tau)$. We have verified that the induced current scales linearly with pulse power, thus it is valid to Fourier transform $\Delta I_{dc}(\tau)$ to obtain $\Delta I_{dc}(\omega)$. In our interferometer the two pulses are nearly identical, so that to an excellent approximation $\Delta I_{dc}(\tau)$ is symmetric about $\tau$=0 and $\Delta I_{dc}(\omega)$ is real.

We now consider the dependence of $\Delta I_{dc}(\omega)$ on barrier height $E_0$, depicted in Figures 6.12(a) and (b). The main part of panels (a) and (b) compare spectra recorded at the operating points labeled in the inset of Fig. 6.12(a) by primed and unprimed letters, respectively. The spectrum, has two main features: a peak at ≈ 25 GHz and a broadband response from ≈ 100-200 GHz whose shape is largely determined by the spectral density of the excitation pulse. The positions of the resonances within the broadband response are field independent and thus are most likely due to reflections from the wire bonds between the transmission line and the tunnel barrier device. The peak at ≈ 25 GHz and the broadband response differ dramatically in their dependence on B. With increasing B the peak shifts to higher frequency while the broad component of the spectrum remains relatively unchanged for fields up to 1 T. We will show in the next Section that the peak at ≈ 25 GHz is due to bulk plasmon excitation of the 2DEG.

For now, we will concentrate on the dependence of $\Delta I_{dc}(\omega)$ on barrier height $E_0$. Both panels in Figs. 6.12(a) and (b) include the spectrum at the point "O" where $E_0 \approx E_f$ and the magnitude of the induced current is greatest. For $E_0 < E_f$ (Fig. 6.12(b)) the low-frequency response is strongly suppressed with increasing $|E_0 - E_f|$. For example, at 100GHz the magnitude changes by a factor of ten over the full range of $V_g$, while the response at 200 GHz changes by a factor of two. The suppression of low-frequency

response is emphasized in the inset of Fig. 6.12(b), in which the curves are normalized to the spectrum recorded at point "O". The periodic oscillations in the ratios result from the reflections from the wire bonds referred to above. In addition, as $E_0$ is varied, the plasmon shows complex behavior which is presently not understood. In addition to becoming negative, the plasmon also acquires an imaginary part. For $E_0>E_f$ (Fig. 6.12(a)) the change in response is qualitatively similar, but the magnitude of the effect is much weaker. For example, at 125 GHz the magnitude drops to 25% as the response at 200 GHz changes by only 36%.

The observation of a frequency dependent photoresponse, which depends on barrier height, is strong evidence that the terahertz radiation couples directly to the barrier region. In addition, the suppression of the low frequency response for $E_0>E_f$ is consistent with an intuitive picture of PAT: a high frequency photon can provide an electron with enough energy to surmount a potential barrier while a low frequency photon cannot. It may appear surprising, however, that suppression of low frequencies is observed for $E_0<E_f$ as well, and that the suppression is far stronger in this regime. Understanding this behavior requires a more realistic model of photon-assisted transport, which includes both Fermi statistics and the physics of barrier formation in a 2DEG.

Figure 6.13 shows a sketch which helps to illustrate the frequency dependence expected for PAT in a degenerate Fermi system. In the presence of an harmonically varying potential, $V_\omega$, an electron incident from the left-hand side will undergo inelastic in addition to elastic scattering. To first order in $V_\omega$ the inelastic processes are transmission with the absorption or emission of a single photon. As Fig. 6.13(a) illustrates, when $E_0>E_f$ overcoming the barrier requires that $\hbar\omega \geq E_0 - E_f$. For $E_0<E_f$ (Fig. 6.13(b)), $\hbar\omega \geq E_f - E_0$ is required in order to reach states above the Fermi level for which there is no counter flow of electrons from right to left. Therefore spectra for $E_f$ above *and* below the barrier are expected to show a threshold when $\hbar\omega \approx |E_f - E_0|$.

This explains why $\Delta I_{dc}(\omega)$ may be suppressed at low frequency for both $E_0$ above and below $E_f$. However, the fact that the low frequency suppression is much stronger for $E_0<E_f$ than for $E_0>E_f$ remains unexplained. In the following we suggest that the trends in $\Delta I_{dc}(\omega)$ reflect dramatic changes in the shape of the barrier in the insulating ($E_0>E_f$) *vs.* conducting ($E_0<E_f$) regimes. To test this hypothesis we apply the Tien-Gordon model for PAT discussed in Section 5.2.2. This model relates $\Delta I_{dc}(\omega)$ to the barrier potential.

Equation {6.8} is an expression for the change in current flowing from left to right, evaluated at zero temperature. As input to this calculation we need only the elastic transmission probability. We use equation {5.6} for the transmission probability of a parabolic potential which depends explicitly on $E_0$ and $\hbar\omega_x$. To simplify the notation, we set $\hbar\omega_x/2\pi=\Gamma$. The $\hbar\omega_y$ dependence of T(E) can be included in $E_0$. An oscillating electric field on the right side will lead to an equation similar to equation {6.8} for the current from right to left. As discussed previously, if the oscillating electric field couples symmetrically to both sides, an equal change is generated in both directions and the net current is zero. To model $\Delta I_{dc}(\omega)$ in our experiment we require an *ac* potential drop which is not symmetric. We assume that the degree of asymmetry is independent of excitation frequency and can be represented by an overall scale factor $\eta$, where $|\eta|<1$.

The parameters of the model are the effective spectral density of the excitation pulse $\eta\alpha^2$, $E_0$, and $\Gamma$. Next we use the spectrum at the peak of the response, labeled "O", to fix $\eta\alpha^2$, which we assume to be independent of gate voltage. This is equivalent to assuming that the power coupling coefficient, $C(\omega)$, defined in equation {6.2} is gate voltage independent. This assumption will be discussed later. We next adjust $\Gamma$, which determines the strength of the low-frequency suppression. A small $\Gamma$ corresponds to a sharp threshold in T(E) and a large reduction in low-frequency response with increasing $|E_f - E_0|$. In order to account for the dramatic difference between Figs. 6.12(a) and6.12 (b) we allow $\Gamma$ to take on two values, one for $E_0$ above and below $E_f$. The amplitude and frequency dependence of the spectra for all other values of $V_g$ are then fit by varying only $E_0$.

The dotted lines in Figs. 6.12(a) and 6.12(b) are fits to the data obtained with the procedure described above. We are able to fit the spectra quite well over the frequency range above the 2D plasmon feature at 25 GHz. From the fit, we find that $E_0$ varies linearly with $V_g$ both above and below $E_f$ as shown in Figure 6.14. However, both $\mu(V_g) = |dE_0 / d(eV_g)|$ and $\Gamma$ change dramatically as the device is swept through the onset of conduction. In the insulating regime, we obtain $\Gamma/h$= 100 GHz and $\mu(V_g)$=0.017, while in the conducting regime, $\Gamma/h$ is much smaller, 20 GHz, and $\mu(V_g)$=0.006.

The fit is significant because the parameters which emerge are consistent with theoretical predictions and with independent *dc* measurements. Numerical modeling of the barrier potential formed by a split-gate electrode predicts the trends described above. Laux *et al.* [6.42] find a sudden increase in $\mu(V_g)$ as $E_0$ is raised above $E_f$ and the screening below the gate electrode changes from metallic to dielectric. Furthermore, the short screening length in the metallic regime leads to a barrier with sharper edges and a flatter top, corresponding to a smaller $\Gamma$ than in the insulating regime.

The value of $\mu(V_g)$ in the conducting regime agrees with an independent determination based on *dc* transport data. The onset of *dc* current across the barrier occurs at a gate voltage $V_{gp}$ which corresponds to the condition $E_0 \approx E_f$. If $E_0$ varies linearly with $V_g$, as expected from numerical modeling [6.42], then $\mu(V_g)$ should equal the ratio $|E_f / V_{go}|$. With $V_{gp}$ =685 meV (see Fig. 6.12(a)) and $E_f$=5.6 meV inferred from the electron density, we find $\mu(V_g)$=0.008, which is in reasonable agreement with the *ac* experimental result $\mu(V_g)$=0.006.

Let us now consider changes in $\Gamma$. In contrast to the our first experiments on a QPC described in 6.2, in this experiment we are fairly certain that we are modulating the electron energy in the leads, thus a Tien-Gordon approach should be valid. In addition, if we assume that power coupling coefficient is gate voltage independent, $\Gamma$ can be related directly to the barrier traversal time. From the discussion in Section 5.2.1, $\Gamma=\hbar/2\tau_t$. In the insulating regime, we obtain $\tau_t$=0.8 ps, while in the conducting regime, $\tau_t$ is much larger,

4ps. The longer traversal time is consistent with the expectation that the barrier will become longer in the conducting regime due to increased screening.

Finally, we consider other possible mechanisms for the observed photocurrent: differential heating due to absorption in the ohmic contacts or wire bonds and/or classical rectification. Both appear to be ruled out immediately because the photocurrent spectra are sensitive to the properties of the device, *i.e.*, they depend on gate voltage. However, it may be argued that the spectral shifts reflect a $V_g$ dependence of the spectral density of terahertz radiation coupled to the device, $\eta\alpha^2$, rather than PAT. To explain the observed behavior, low-frequency radiation would have to couple poorly to the device for $E_0>E_f$, go through a maximum when $E_0\approx E_f$, and decrease again for $E_0<E_f$. The coincidence of maximum coupling at $E_0\approx E_f$, particularly when the device impedance is varying monotonically, seems unlikely. As a result, we believe that PAT provides the most reasonable description of the data.

In conclusion, this experimental study has demonstrated that PAT provides a consistent explanation for the *dc* current induced across a tunnel barrier by terahertz radiation. The variation in barrier shape deduced from the model is a consequence of the crossover from metallic to dielectric screening. In addition, if we assume that the power coupled to the device is gate voltage independent, the barrier has a parabolic shape, and the Tien-Gordon approach is valid, we obtain a value for the barrier traversal time of 4 and 0.8 ps in the conducting and insulating regimes respectively.

### 6.3.7 Terahertz Interferometry-Magnetic Field Dependence

We now discuss in detail the rectified current response as a function of magnetic field, B. The first experiment that we did was to measure the $\Delta I_{dc}$ due to a single pulse as a function of B. The gate voltage was set to maximize the rectified response. This corresponds to point "O" in Fig. 6.12(a). Next the field was swept from 0 to 0.6 T. The measured $\Delta I_{dc}$ is shown in Figure 6.15 by the dark solid line. It clear from this figure that

$\Delta I_{dc}$ depends dramatically on B. We immediately recognized two important features in these data. The first is the fast oscillations in B with a periodicity that increases at larger B. This behavior is characteristic of the field dependence of the density of states at the Fermi level of the 2DEG. Most commonly, the field dependence of density of states is seen in the Shubnikov-De Hass oscillations in the *dc* source-drain current. If we ignore the fast oscillations in $\Delta I_{dc}$, we also see that $\Delta I_{dc}$ varies on a much slower field scale of 0.6 T. This is exactly the same field scale as cyclotron resonance. At 0.3 T the cyclotron frequency is 120GHz which is near the center frequency of our pulses. In addition, the shape of the $\Delta I_{dc}$ looks similar to the spectrum "O" ($\Delta I_{dc}(\omega)$) in Fig. 6.12(a). To show this explicitly, we have plotted the negative of the spectrum "O" as the dashed curve in Fig. 6.15. To convert from frequency to magnetic field, we have used the cyclotron resonance condition, $\omega = eB/m^*$ with $m^* = 0.07 m_o$ where $m_o$ is the free electron mass. It is clear that there is a strong resemblance between the $\Delta I_{dc}(B)$ and $-\Delta I_{dc}(\omega(B))$.

To investigate the system further, we have made measurements of the spectra as a function of B. Figure 6.16(a) shows the real part of $\Delta I_{dc}(\omega)$ at several magnetic fields, measured at the value of $V_g$ which gives the maximum response (point O in the inset of Figure 6.12(a)). These spectra were taken at those fields where $\Delta I_{dc}$ due to a single pulse was a minimum (see Fig 6.15). As discussed previously, the spectrum with B=0, shown in the lowest curve in Fig. 6.16(a), has two main features: a peak at $\approx$ 25 GHz and a broadband response from $\approx$ 100-200 GHz whose shape is largely determined by the spectral density of the excitation pulse. These two features differ dramatically in their dependence on B, as the spectra above indicate. At a relatively small field, 0.25 T, the 25 GHz peak disappears, and a peak with reversed sign appears at 100 GHz. With increasing B the negative-going peak continues to shift to higher frequency while the broad component of the spectrum remains relatively unchanged for fields up to 1 T.

The dependence of the sharp peak on B is indicative of a bulk magnetoplasmon excitation of the 2DEG. This is similar to the behavior we saw in the first experiments on

the QPC described in Section 6.2.2. The lower panel of Fig. 6.16 is a plot of the peak frequency *vs.* B, including both the positive peak at B=0 and the negative peak at nonzero field. The solid line is the upper branch of the magnetoplasmon spectrum expected for the GaAs 2DEG: $\nu_+^2(B)=\nu_p^2+\nu_c^2$, where $\nu_p$ and $\nu_c$ are the 2D plasma and cyclotron frequency, respectively [6.20]. The fit was obtained with $\nu_p$=25 GHz, which corresponds to a confinement length of 670μm, using the measured 2DEG density and a GaAs band mass of 0.07 $m_e$. The confinement length scale indicates that the plasmon is an excitation of the large 650 μm 2DEG "leads" to the quasi-1D wire. Thus the sharp, field-dependent feature in the spectrum is not due to the properties of the submicron channel/barrier, but rather the macroscopic 2DEG regions. The barrier serves as a detector of this 2DEG resonance.

From the dispersion relation and the spectra in Fig.6.16 it is clear that the low frequency peak is a plasmon associated with the bulk 2DEG. The most surprising and unexpected feature is that the plasmon reverses sign as the field is increased from zero field. In fact at 0.1 T the magnetoplasmon actually disappears as it reverses sign from 0T to 0.25 T. Usually one is not used to a negative going signal in the photocurrent spectrum. In this experiment since we plot the *real* part of the Fourier transform of $\Delta I_{dc}(\tau)$, the sign can actually go negative. The sign in this case simply records the direction of the induced current. Thus at 0 T the broadband response and the plasmon response both drive an induced current in the same direction. This is in contrast to the response at 0.34 T where the magnetoplasmon now drives currents in the opposite direction to the broadband response. These two components nearly cancel so that the *dc* photocurrent induced from a single pulse is nearly zero.

The mechanism for the sign reversal is currently not fully understood. We propose the following preliminary hypothesis. The zero field plasmon is due to heating of the left lead which subsequently leads to an induced current flowing from left to right. As the magnetic field is increased the electronic states begin to evolve into edge states. In this picture electrons at the edge are excited to higher energy edge states and then relax towards

the center of the lead. Electrons near the center will have a lower probability of transmission when they reach the QPC and will in turn lead to an induced current flowing from right to left, opposite to the direction at zero field. This picture was used by E. Dieβel *et al.* to explain cyclotron resonance absorption in a 2DEG at high magnetic fields [6.43].

The behavior of the spectra as a function of B suggests that heating due to the bulk magnetoplasmon absorption by the 2DEG cannot explain the broadband component of the induced current. If this were the mechanism then we expect $\Delta I_{dc}(\omega)$ to peak only near frequencies at which the 2DEG absorbs energy from the electromagnetic field. Instead, the magnetoplasmon appears only as a perturbation of the field-insensitive continuum.

To investigate the fast oscillations of $\Delta I_{dc}$ in Fig. 6.15 further, we have made measurements of the spectrum at two adjacent field points. The results are shown in Fig. 6.17 for B=0.31 T (dotted curve) and 0.328 T (solid curve) which corresponds to an adjacent minimum and a maximum in $\Delta I_{dc}$ of Fig. 6.15 respectively. For reference, cyclotron resonance is at 124 GHz at this magnetic field. For this small change in field, the amplitude of the magnetoplasmon absorption changes by a factor of three and the line width remains constant. Since the line width remains fairly constant, we do not expect that the scattering rate is strongly field dependent. In contrast, since the amplitude of the absorption changes, this implies that the number of carriers available for excitation is strongly field dependent.

To explain this effect, we apply an argument given by J.C. Maan *et al.* [6.44]. They measured cyclotron resonance in a 2DEG (without a tunnel barrier detector) by measuring the rectified current in the presence of a CW far infrared laser as a function of magnetic field in the Quantum Hall regime [6.2]. They found that the strength of the cyclotron absorption was much greater at those magnetic fields where $\rho_{xx}$=0 (Hall plateaus) than when $\rho_{xx}$ was finite (Hall risers). They postulated that this is due to the fact that when $\rho_{xx}$=0 no scattering is allowed. FIR radiation changes this situation since photoexcited carriers in the higher Landau level and the empty states left behind in the

lower Landau level increase the scattering and a large change in $\rho_{xx}$ is expected. The large change in $\rho_{xx}$ leads to a large $\Delta I_{dc}$. In contrast, on a Hall riser, the Fermi level is in the middle of a Landau level, which is partially empty,and $\rho_{xx}$ is finite. Since $\rho_{xx}$ is allready finite, scattering due to FIR photons is expected to induce a much weaker change in $\rho_{xx}$ and hence a smaller $\Delta I_{dc}$. This picture is consistent with the behavior seen in our spectra at low fields, even though we are not fully in the Quantum Hall regime. Thus B=0.31T corresponds to a *Hall Plateau* and B=0.328 T corresponds to a *Hall Riser*. Unfortunately *dc* transport measurements of the $\rho_{xx}$ were not made on this device simultaneously with the $\Delta I_{dc}$ measurements to verify in fact that B=0.31 T is a *Hall Plateau* and B=0.328 T is a *Hall Riser.*

In addition to the data described above, we have made preliminary measurements at B=1 T, where the bulk magnetoplasmon absorption of the 2DEG is well above the spectral range of the pulse. These data are shown in Figures 16.18(a) and 16.18(b). The behavior in Figs. 16.12(a) and 16.12(b) is observed at this high field as well; suppression of the low-frequency response as $E_0$ is varied away from $E_f$, and a much stronger effect when $E_0<E_f$. From the discussion in Section 5.1.2, we know that T(E) should become sharper in a magnetic field. This would imply that the low frequency suppression will be stronger in a field. In the future, more detailed experiments could be performed to verify this prediction. Nevertheless, these preliminary results verify that the observed low frequency suppression is not due to changes in coupling to the magnetoplasmon.

## 6.4 Conclusions

In conclusion, this experimental study has demonstrated that PAT provides a consistent explanation for the *dc* current induced across a tunnel barrier by terahertz radiation. We have made the first measurements of PAT in a tunnel barrier as a function of source-drain voltage and gate voltage. From the gate voltage experiments, we find that the variation in barrier shape deduced from the model is a consequence of the crossover from

metallic to dielectric screening. Other possible mechanisms for the induced current, radiation-induced heating of the bulk 2DEG, heating of the contacts and wire bonds, and classical rectification, that exactly mimic the gate voltage and source-drain voltage dependence of PAT is highly unlikely.

## 6.5 References


[6.1] R. Landauer, *IBM J. Res. Dev.* **1**, 223 (1957); *Phys. Lett.* **85A**, 91 (1981); *J. Phys.: Condens. Matter* **1**, 8099 (1989).

[6.2] K. von Klitzing, G. Dorda, and M. Pepper, *Phys. Rev. Lett.* **45**, 494 (1980).

[6.3] B. J. van Wees, H. van Houten, C. W. J. Beenakker, J. G. Williamson, L. P. Kouwenhoven, D. van der Marel, and C. T. Foxon, *Phys Rev. Lett.* **60**,848 (1988); D. A. Wharam, T. J. Thornton, R. Newbury, M. Pepper, H. Ahmed, J. E. F.Frost, D. G. Hasko, D.C. Peacock, D.A. Ritchie, and G.A.C. Jones, *J. Phys.C* **21**, L209 (1988).

[ 6.4] M. Buttiker and R. Landauer, *Phys. Rev. Lett.* **49**, 1739 (1982).

[6.5] Y. Fu and S.C. Dudley, *Phys. Rev. Lett.* **70**, 65 (1993).

[6.6] M. Buttiker *et. al Phys. Rev. Lett.* **70**, 4114 (1993).

[6.7] H.C. Liu, *Phys. Rev. B* **43**, 12538 (1991).

[6.8] L.P. Kouwenhoven *et al.*, *Phys. Rev. B* **39**, 8040 (1989).

[6.9] For a review of PAT in SIS junctions see J.R. Tucker and M.J. Feldman, *Rev. Mod. Phys.* **57**, 1055 (1985).

[6.10] J. Orenstein, International Workshop on Infrared and Millimeter Waves Spectroscopy, Bad Honnef, FRG 1993; J. Orenstein, *Laboratory Directed Research and Development Program*, Lawrence Berkeley Lab-FY 1993 **PUB-5382**, 65 (1994).

[6.11] C. Karadi, S. Jauhar, L.P. Kouwenhoven, K. Wald, J. Orenstein, P.L. McEuen, Y. Nagamune, and H. Sakaki, J. Opt. Soc. Am. B 11, 2566 (1994).

[6.12] C. Karadi, S. Jauhar, L.P. Kouwenhoven, K. Wald, J. Orenstein, P.L. McEuen, Y. Nagamune, and H. Sakaki, International Conference on Lasers and Optoelectronics, Post Deadline Session, June 94. Optics and Photonics News, ??.

[6.13] C. Karadi, S. Jauhar, L.P. Kouwenhoven, K. Wald, J. Orenstein, P.L. McEuen, Y. Nagamune, and H. Sakaki, OSA Conference on Ultrafast Electronics and Optoelectronics-1995 Technical Digest **13**, 118 (1995).

[6.14] C. Karadi, S. Jauhar, L.P. Kouwenhoven, K. Wald, J. Orenstein, P.L. McEuen, Y. Nagamune, and H. Sakaki, *Phys. Rev. B*, (to be published).

[6.15] N.K. Patel *et al.*, in *20th International Conference on the Physics of Semiconductors Vol. 3*, edited by E. M. Anastassakis and J. D. Joannopoulos (World Scientific, Singapore, 1990), p. 2371

[6.16] Qing Hu, R.A. Wyss, C.C. Eugster, J.A. del Alamo, M.J. Rooks, and M.R. Melloch, DRC Conference (March 1992).

[6.17] R. A. Wyss, C. C. Eugster, J. A. del Alamo, and Q. Hu, *Appl. Phys. Lett.* **63**, 1522 (1993).

[6.18] S. Weiss, D.F. Ogletree, D. Botkin, M. Salmeron, and D.S. Chemla, *Appl. Phys. Lett.* **63**, 2567 (1993). S. Weiss, D. Botkin, D.F. Ogletree, M. Salmeron, and D.S. Chemla, *Phys. Stat. Sol. (b)* **188**, 343 (1995).

[6.19] T.J.B.M. Janssen *et. al*, *J. Phys. Condens. Matter* **6**, L 163 (1994).

[6.20] For an introduction to quantum dots see M. Kastner, *Physics Today* **46**, 24 (1993) and references therein.

[6.21] L. P. Kouwenhoven, S. Jauhar, J. Orenstein, P.L. McEuen, Y. Nagamune J. Motohisa, and H. Sakaki, *Phys. Rev. Lett.* **73**, 3443 (1994); L. P. Kouwenhoven,S. Jauhar, J. Orenstein, P.L. McEuen, Y.V. Nazarov, N.C. van der Vaart, Y. Nagamune J. Motohisa, and H. Sakaki, *Phys. Rev. B* **50,** 2019 (1994).

[6.22] S. Verghese, R.A. Wyss, Th. Schapers, A. Forster, M.J. Rooks, and Q. Hu, submitted 12/19/94.

[6.23] D.W. van der Weide, R.H. Blick, F. Keilmann, R.J. Haug, K. von Klitzing, K. Eberl, OSA Conference on Quantum Optoelectronics-1995 Technical Digest **14**, 103 (1995).

[6.24] N. S. Wingreen, A-P. Jauho, Y. Meir, *Phys. Rev. B* **48**, 8487 (1993).

[6.25] K.R. Wald, L.P. Kouwenhoven, P.L. McEuen, N.C. Vandervaart, C.T. Foxon, *Phys. Rev. Lett.* **73**, 1011 (1994). K.R. Wald, Ph.D. Thesis UC Berkeley, 1995.

[6.26] L. P. Kouwenhoven, Ph.D. Thesis Delft University, 1992.

[6.27] E. B. Foxman, P.L. McEuen, U. Meirav, N.S. Wingreen, Y. Meir, P.A. Belk, N.R. Belk, M.A. Kastner, and S.J. Wind, *Phys. Rev. B* **47**, 10020 (1993).

[6.28] T. N. Theis et al., *Solid State Commun.* **24**, 273 (1977). For a review see D. Heitmann, *Surf. Sci.* **170**, 322 (1986).

[6.29] F. Stern, *Phys. Rev. Lett.* **18**, 546 (1967).

[6.30] D. Weiss, C. Zhang, R.R. Gerhardts, K. von Klitzing, and G. Weimann, *Phys. Rev. B* **39**, 13020 (1989).

[6.31] D. H. Auston, "Ultrafast Optoelectronics," in *Topics in Applied Physics Vol. 60: Ultrashort Laser Pulses Generation and Applications* 2ed., edited W. Kaiser (Springer-Verlag, New York,1992), pp. 183-233.

[6.32] M. van Exter, D. Grischkowsky, *IEEE Trans. Microwave Theory Tech.* **38**, 1684 (1991).

[6.33] Y. Nagamune, H. Sakaki, L. P. Kouwenhoven, L. C. Mur, C. J. P. M. Harmans, J. Motohisa, and H. Noge, *Appl. Phys. Lett.* **64**, 2379 (1994).

[6.34] M. Kominami, D.M. Pozar, D. H. Schaubert, *IEEE Tran. Antennaas Propagat.* **AP-33**, 600 (1985).

[6.35] C.P. Wen, *IEEE Trans. Microwave Theory Tech.* **17**, 1087 (1969). See also K.C. Gupta, R. Garg, I.J. Bahl, Microstrip Lines and Slotlines, Massachusetts: Artech House, 1979.

[6.36] M.Y. Frankel, S. Gupta, J.A. Valdmanis, G.A. Mourou, *IEEE Trans. Microwave Theory Tech.* **39**, 910 (1991).

[6.37] Y. Nagamune, H. Sakaki, L. P. Kouwenhoven, L. C. Mur, C. J. P. M. Harmans, J. Motohisa, and H. Noge, *Appl. Phys. Lett.* **64**, 2379 (1994).

[6.38] H. van Houten, B.J. van Wees, M.G.J. Heijiman, and J.P. Andre, *Appl. Phys. Lett.* **49**, 1781 (1986).

[6.39] S. Feng and Q. Hu, *Phys. Rev. B* **48**, 5354 (1993).

[6.40] Y.R. Shen, The Principles of Nonlinear Optics, New York: John Wiley & Sons, 1984; F. Hekking, Y. V. Nazarov, *Phys. Rev. B* **44**, 11506 (1991).

[6.41] S.M. Sze, Physics of Semiconductor Devices second edition, New York: John Wiley & Sons, 1981.

[6.42] S.E. Laux, D.J. Frank, and F. Stern, *Surf. Sci.* **196**, 101 (1988).

[6.43] E. Dieβel, G. Muller, D. Weiss, K. von Klitzing, K. Ploog, H. Nickel, W. Schlapp, and R. Losch, *Appl. Phys. Lett.* **58**, 2231 (1991).

[6.44] J.C. Mann, Th. Englert, D.C. Tsui, and A.C. Gossard, *Appl. Phys. Lett.* **40**, 609 (1982).

## 6.6 Figure Captions

Figure 6.1: (Baby) Conductance vs. Gate (baby) voltage at T=0.9 K and B=0 T in the presence of a source-drain bias of 50 $\mu$V.

Figure 6.2: Same as Fig. 6.1 with series resistance removed. Step like structure is direct evidence for conductance quantization in units of $2e^2/h$.

Figure 6.3: First measurements of $\Delta I_{dc}$ (x1000) vs. $V_g$ in a QPC in the presence of terahertz pulses at T=0. 5K at different power levels. The step like structure in $I_{dc}$ vs. $V_g$ is also shown. The bipolar structure of $\Delta I_{dc}$ appears near the steps of $I_{dc}$.

Figure 6.4: (inset) Nonlinear I-$V_{sd}$ curve of a QPC in the presence of large negative gate voltage, $V_g$=-1.936 V. (a) Time domain interferogram in a QPC at $V_{sd}$=5.0 mV. (b) Same as (a) but $V_{sd}$ = 2.7 mV. These bias points are labeled in the inset.

Figure 6.5: The main panel shows Fourier transforms of interferograms at source-drain bias voltages of 2.7, 3.5, 4.0, and 4.6 mV. Each spectrum is normalized to the spectrum at $V_{sd}$ =5.0 mV (open circle in inset). (inset) Nonlinear $I_{dc} - V_{sd}$ curve of QPC with markers for bias values. The threshold for absorption moves to higher frequencies as the bias is lowered.

Figure 6.6: Representative time domain interferograms at $V_{sd}$=4.6 mV and at B=0 and B=0.2 T. The dramatic change in the response can be attributed to a magnetoplasmon in the bulk 2DEG.

Figure 6.7: $\Delta I_{dc}$ at fixed frequencies, 110, 150, and 170 GHz as a function of magnetic field. The peak in $\Delta I_{dc}$ moves to higher magnetic field as the frequency is increased. This positive dispersion is plotted in the inset. The dashed curve is a fit to the magnetoplasmon dispersion relation and the solid curve follows the cyclotron resonance condition.

Figure 6.8: New terahertz interferometer. BS=wire grid beam splitter. P=polarizer. PC=photoconductive Auston switch. We measure $\Delta I_{dc}$ in the device as a function of time delay, $\tau$, between the two pulses. Fourier transformation of $\Delta I_{dc}$ gives the frequency response of the device.

Figure 6.9: Schematic diagram of the antenna-transmission line coupling to the device.

Figure 6.10: Scanning electron micrograph of tunnel barrier device.

Figure 6.11: Solid curve is the source-drain current for an applied bias of 100 $\mu$V. The dotted curve is the induced current.

Figure 6.12: Re[$\Delta I_{dc}(\nu)$] at B=0 measured at different gate voltages indicated in the inset. The solid curves correspond to measured data. The dashed lines are a fit to a PAT theory. (a) Re[$\Delta I_{dc}(\nu)$] for $E_0 > E_f$. Inset: The dc current flowing through the tunnel barrier vs. gate voltage in the absence of pulsed excitation.(b) Re[$\Delta I_{dc}(\nu)$] for $E_0 < E_f$. Inset: Ratios of Re[$\Delta I_{dc}(\nu)$] relative to spectra "O".

Figure 6.13: (a) Tunnel barrier with barrier height, $E_0$, greater than the Fermi Energy, $E_f$. An electron incident at energy, E, is scattered by a harmonically varying potential at frequency $\nu$ in the left lead into a direct beam at energy E and two sidebands at energies $E \pm h\nu$. (b) Similar to (a) but with $E_0 < E_f$.

Figure 6.14: Barrier height, $E_0$, and broadening, $\Gamma$, as a function of $V_g$ obtained from fits of the data in Fig. 6.12 to a PAT theory.

Figure 6.15: Solid curve is $\Delta I_{dc}$ due to a single pulse as a function of magnetic field. The gate voltage is adjusted to maximize the photoresponse. Dashed curve is the frequency spectrum [ $-\Delta I_{dc}(\omega(B))$ ] of the coupled terahertz power to the device. The cyclotron resonance formula was used to convert from frequency to magnetic field.

Figure 6.16: (a) Re[$\Delta I_{dc}(\nu)$] at typical magnetic fields. The spectra have been offset for clarity. (b) Plot of low frequency resonance at 25 GHz *vs.* magnetic field (boxes). Solid line is a fit to the magnetoplasmon dispersion relation.

Figure 6.17: Re[$\Delta I_{dc}(\nu)$] at adjacent minima (B=0.31 T) and maxima (B=0.328 T) field points in Fig. 6.15. The strength of the magnetoplasmon absorption at 125 GHz changes dramatically for this relatively small change in field.

Figure 6.18: Preliminary measurements of Re[$\Delta I_{dc}(\nu)$] at B=1 T measured at different gate voltages similar to Fig. 6.12. (a) Re[$\Delta I_{dc}(\nu)$] for $E_0 > E_f$. Decreasing spectral strength corresponds to increasing $E_0$. (b) Re[$\Delta I_{dc}(\nu)$] for $E_0 < E_f$. Decreasing spectral strength corresponds to decreasing $E_0$.

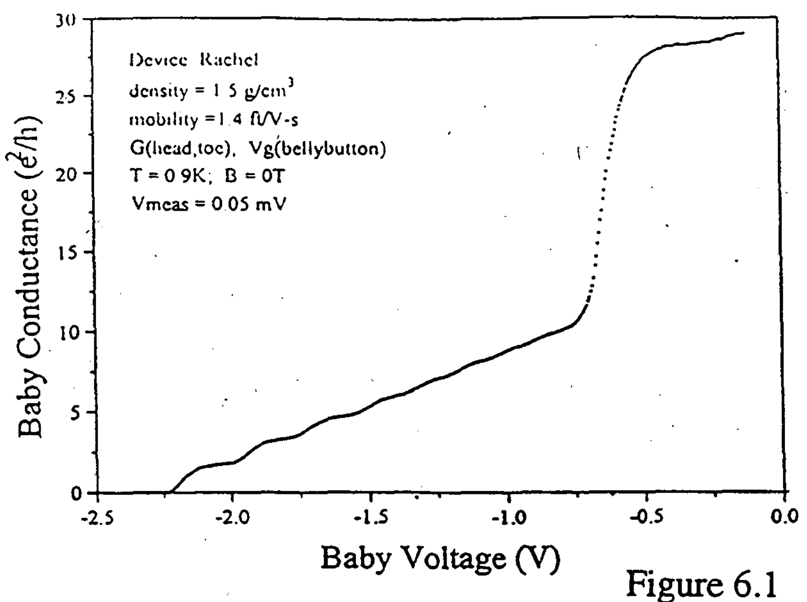


Figure 6.1

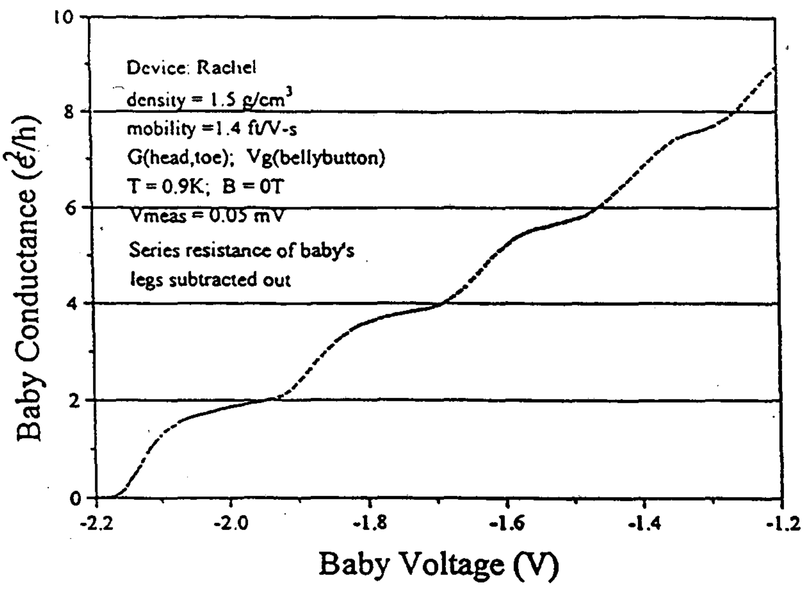


Figure 6.2

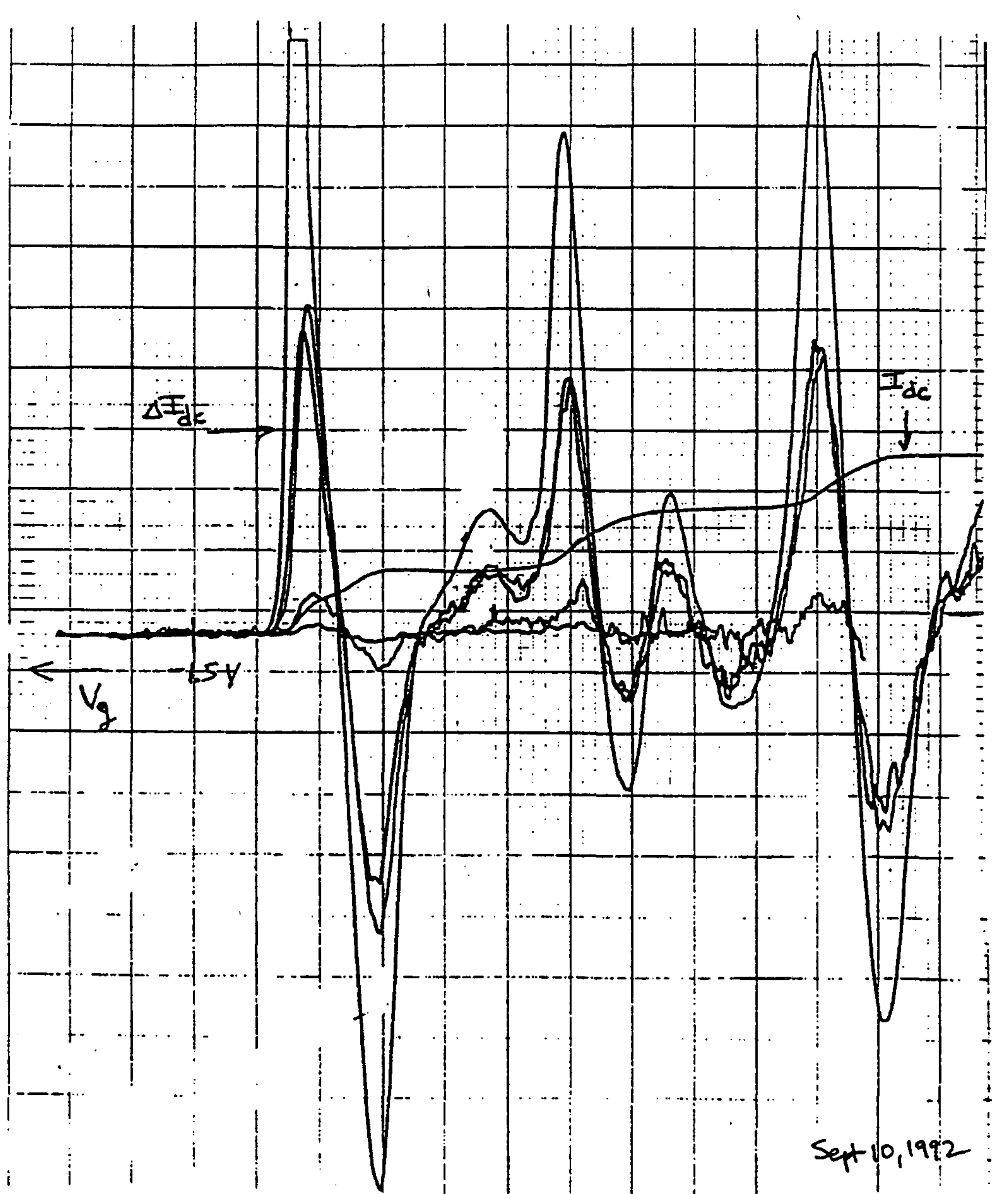


Figure 6.3

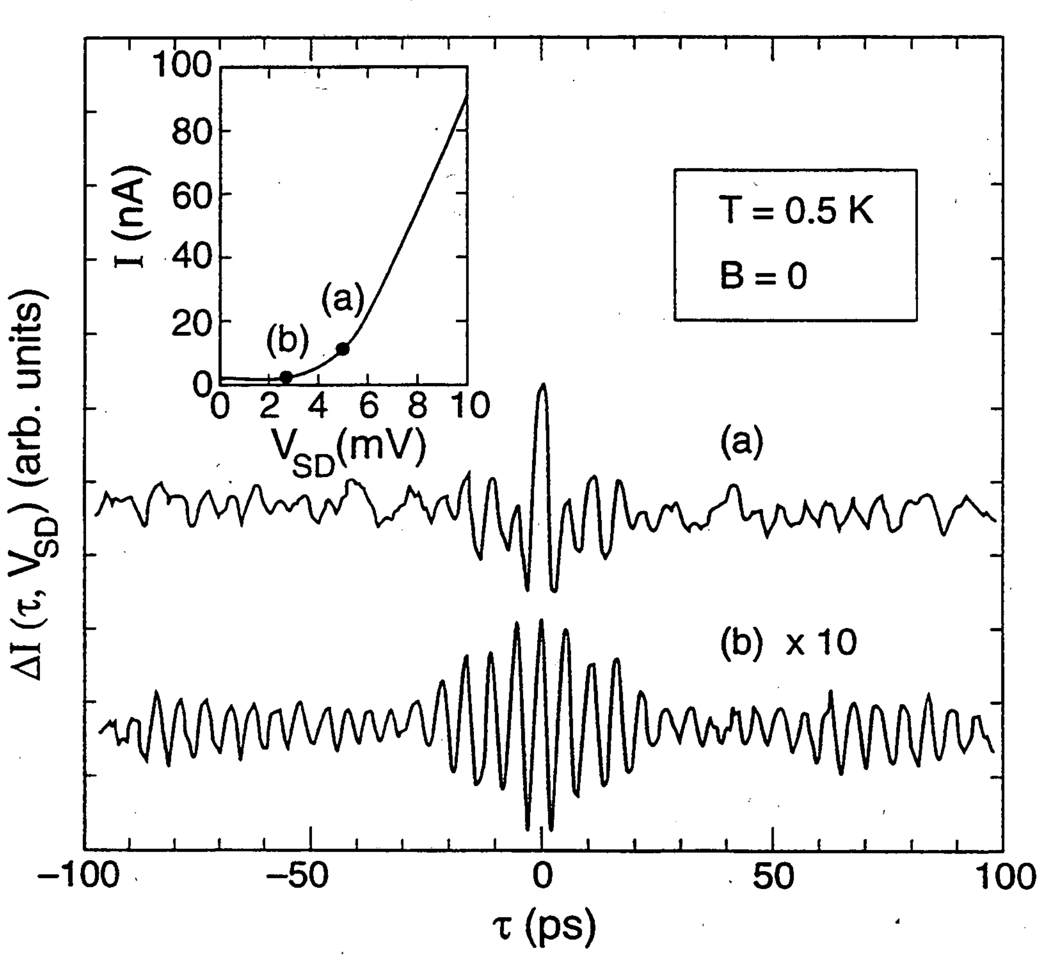


XBL 937-4073

Figure 6.4

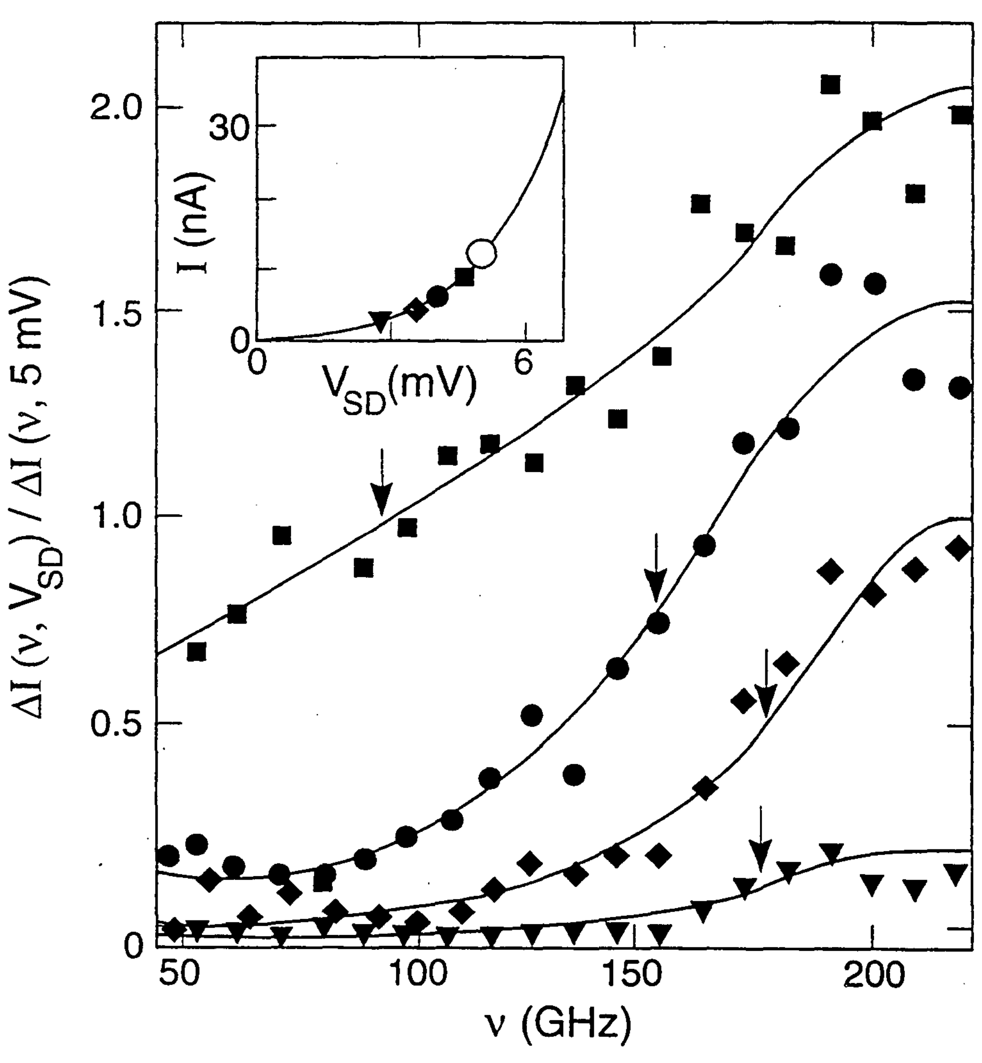


XBL 937-4074

Figure 6.5

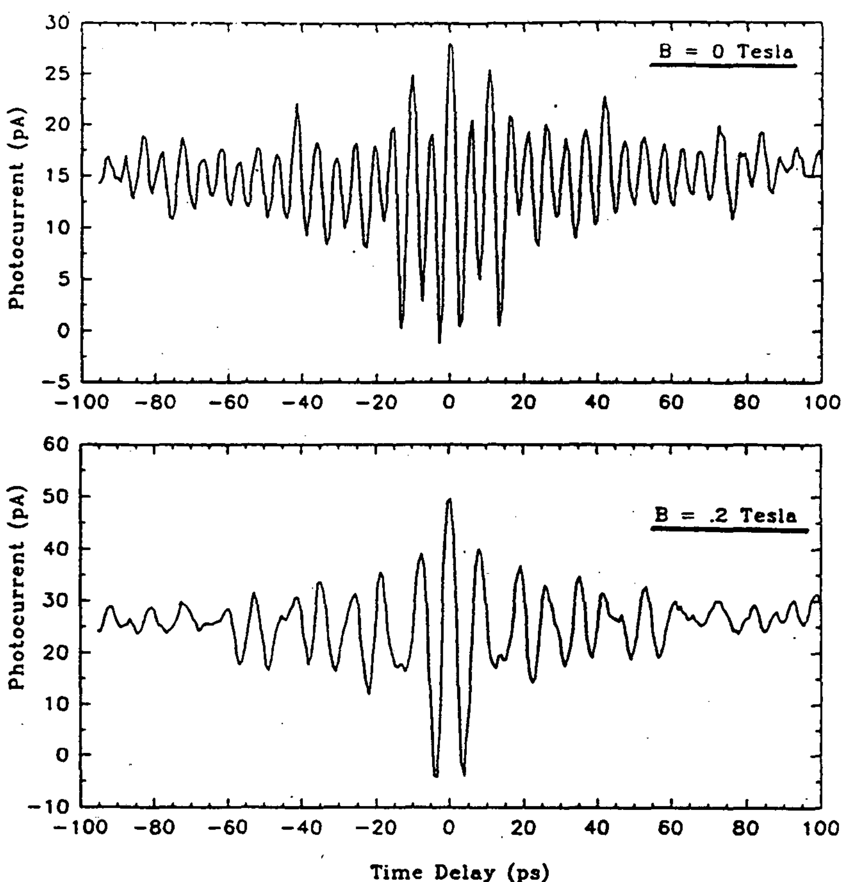


Figure 6.6

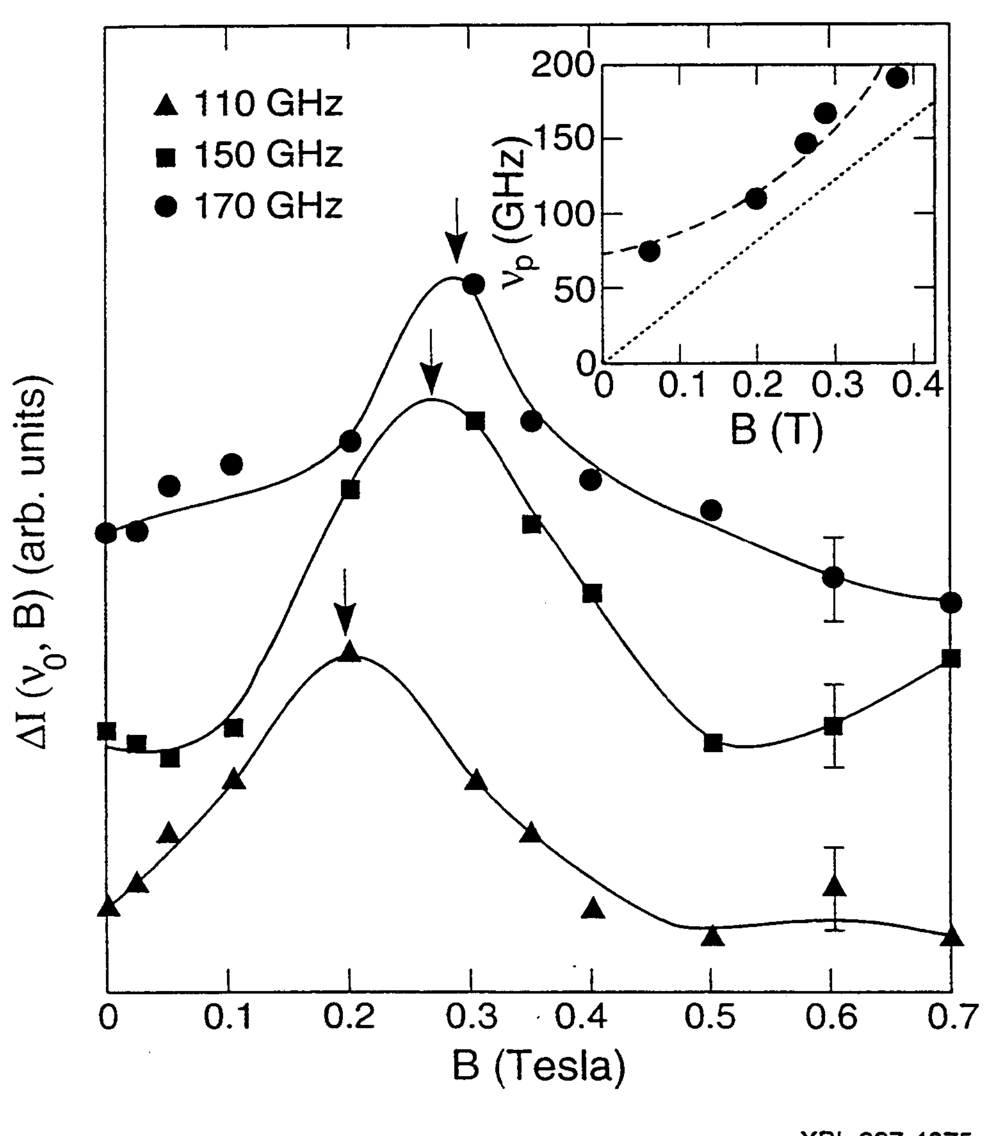


XBL 937-4075

Figure 6.7

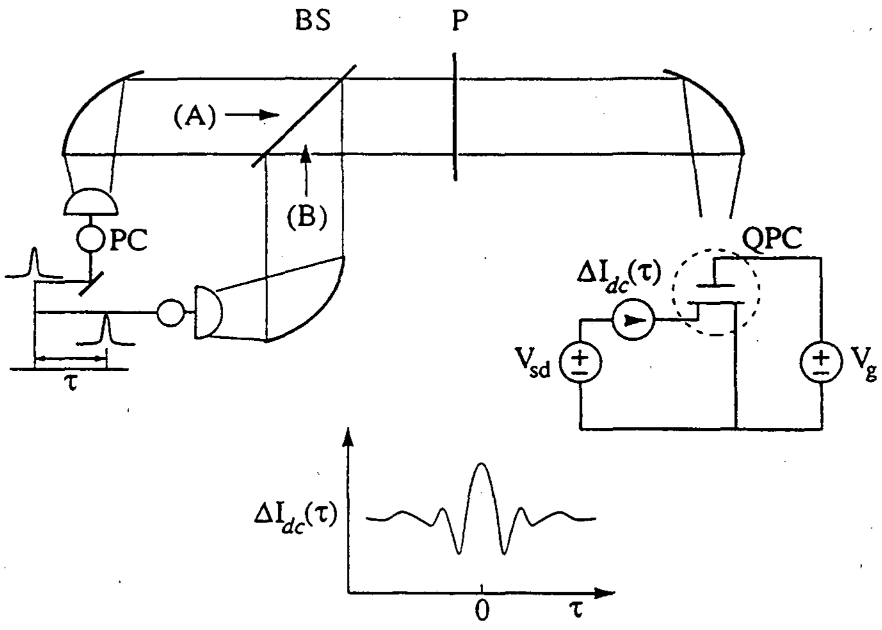


Figure 6.8

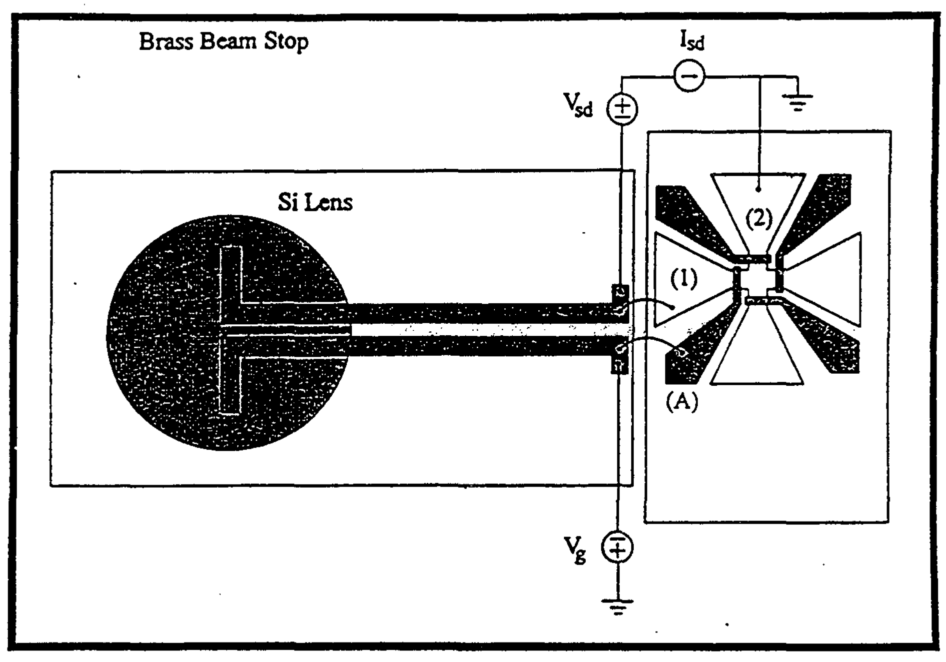


Figure 6.9

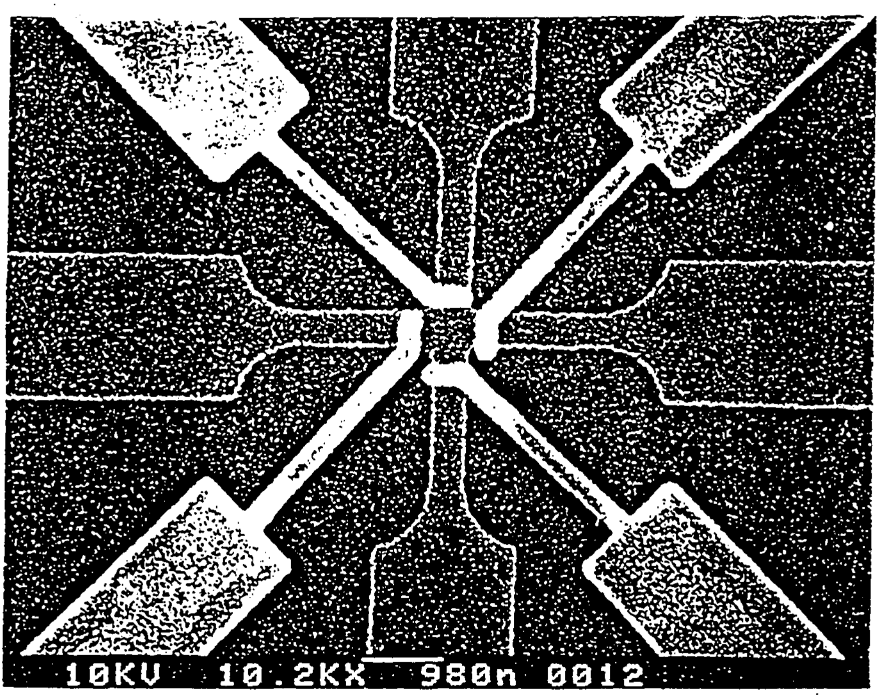


Figure 6.10

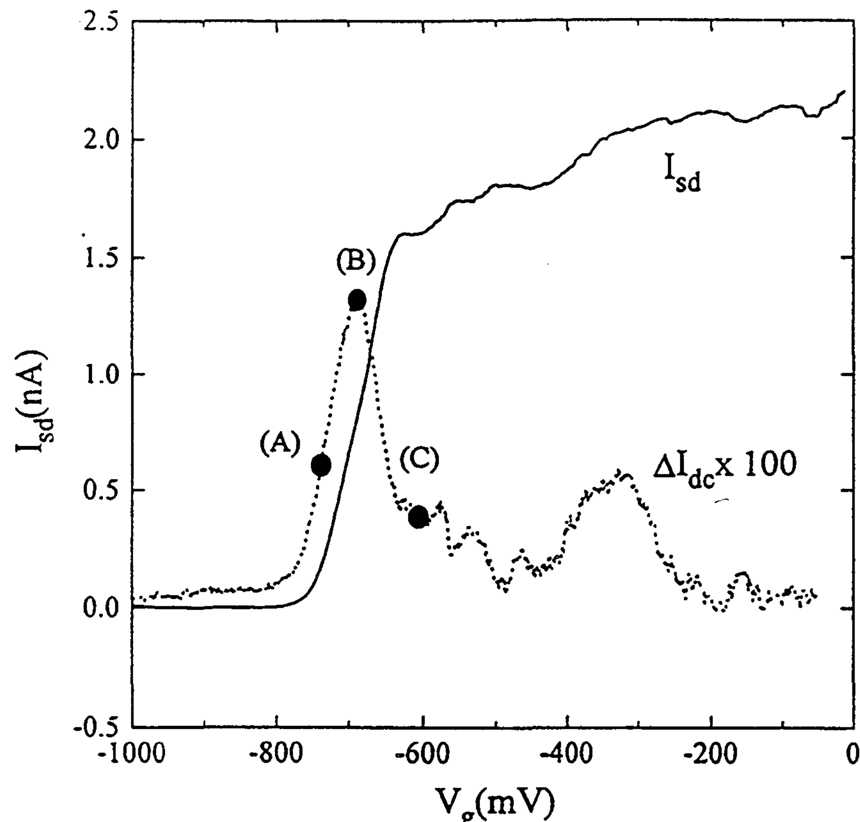


Figure 6.11

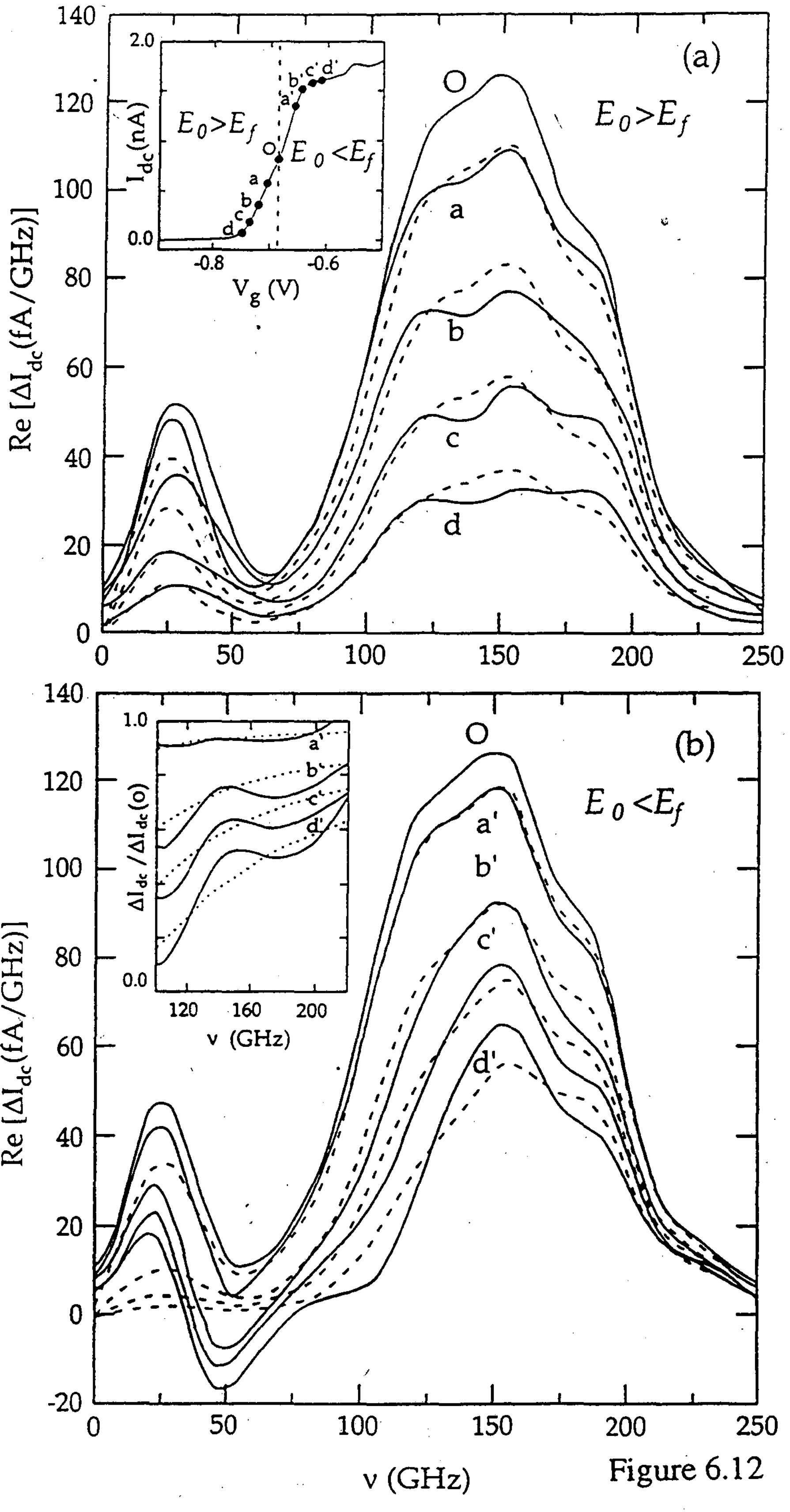


Figure 6.12

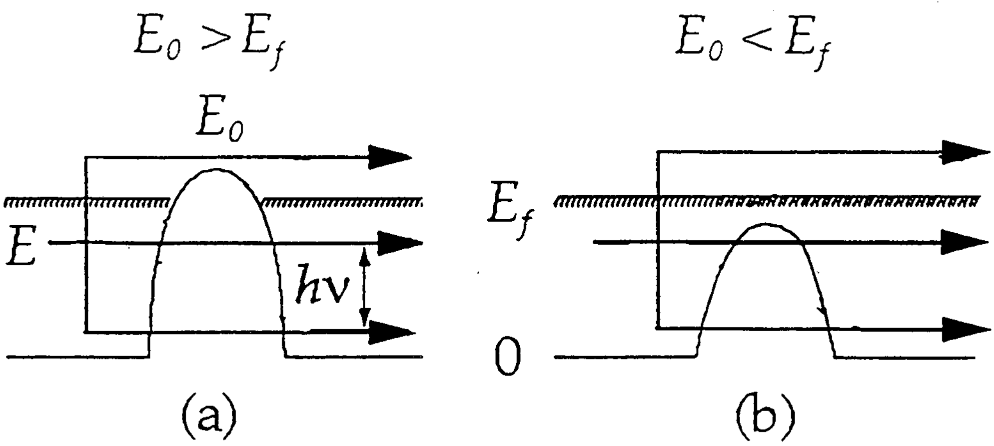


Figure 6.13

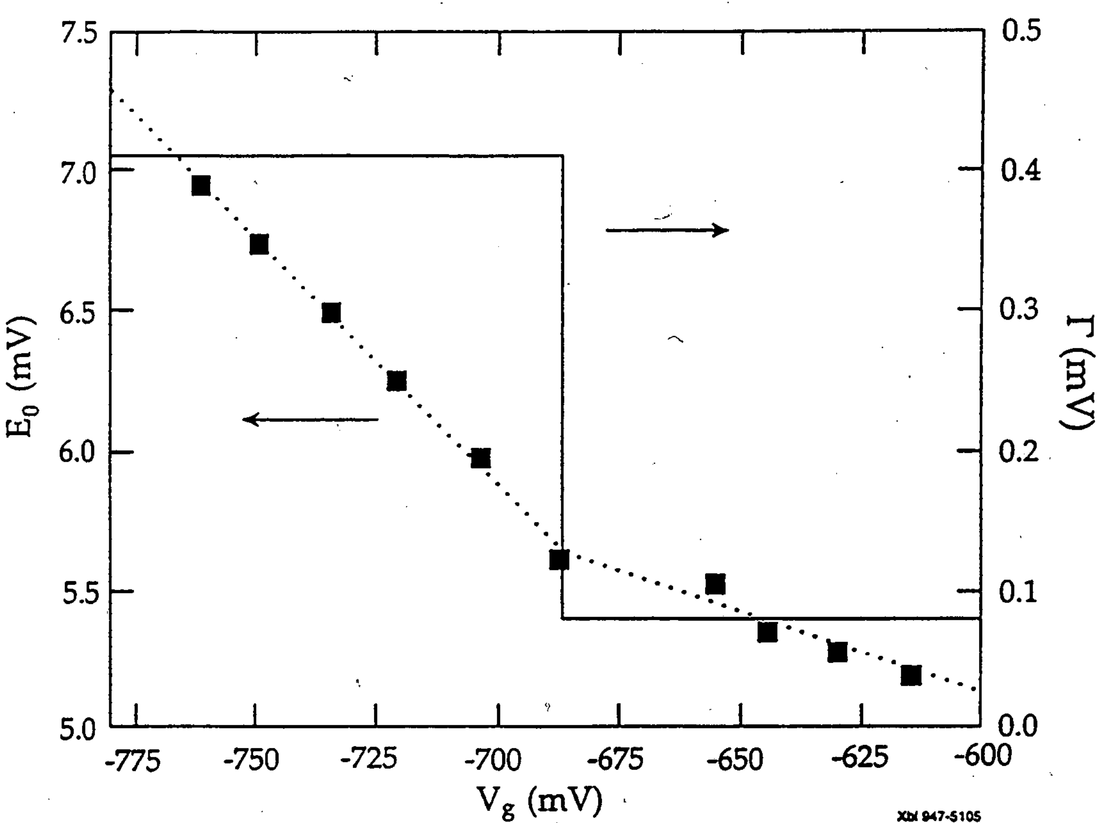


Figure 6.14

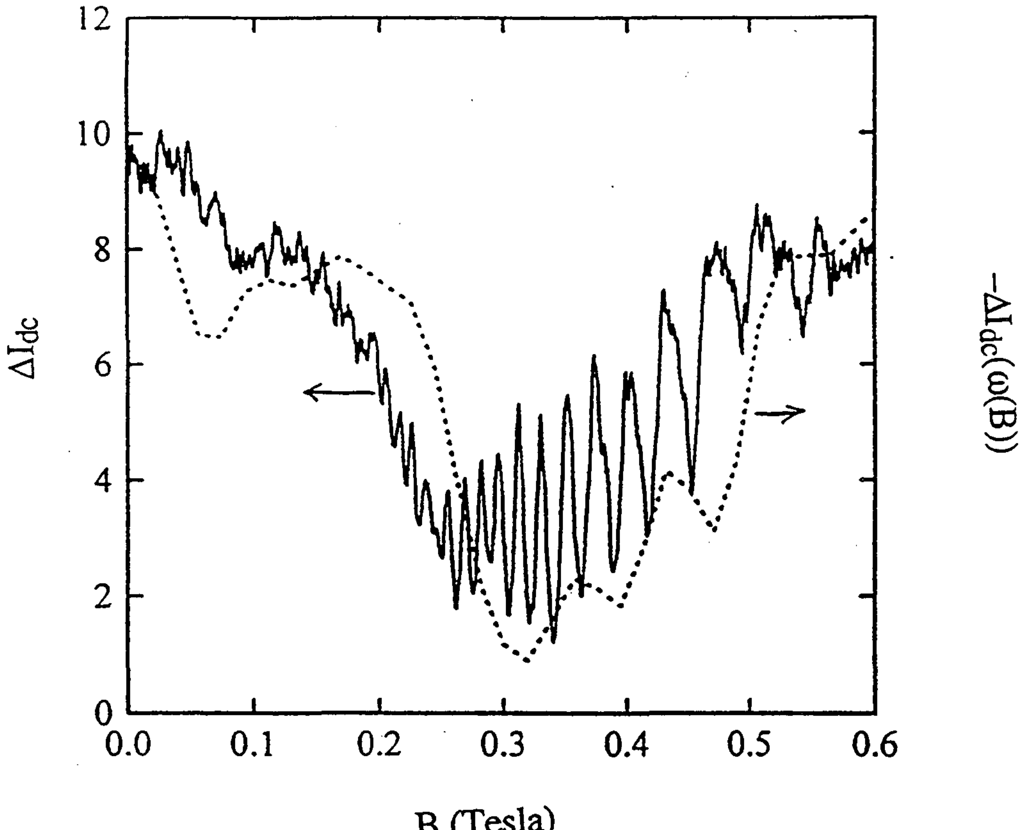


Figure 6.15

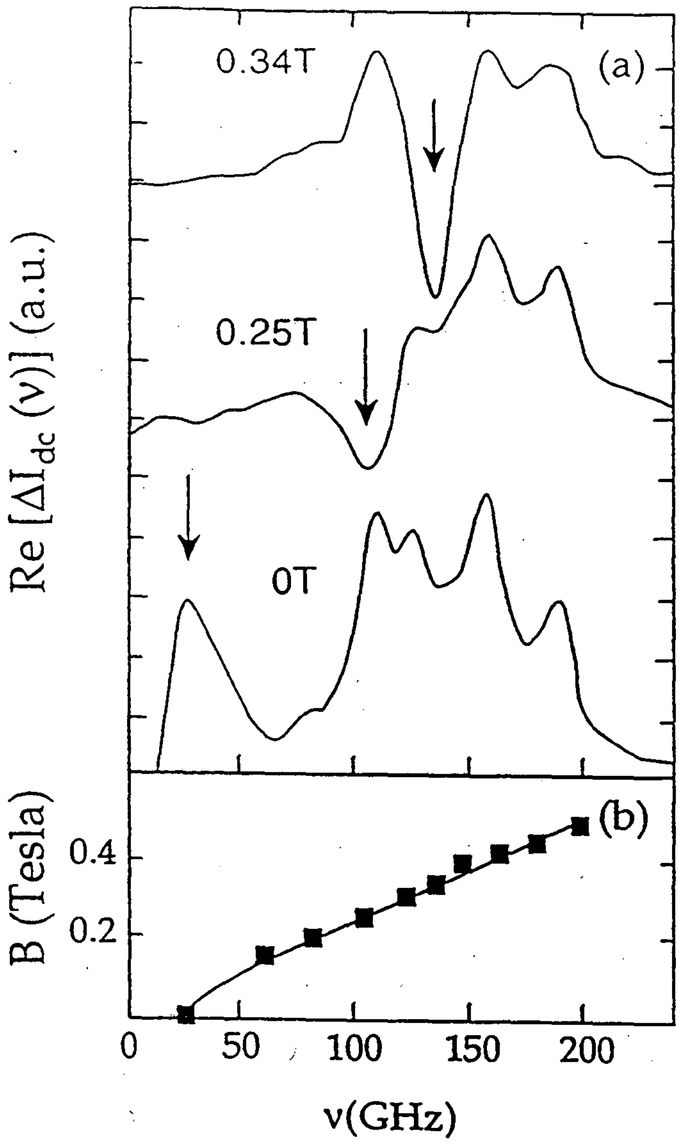


Figure 6.16

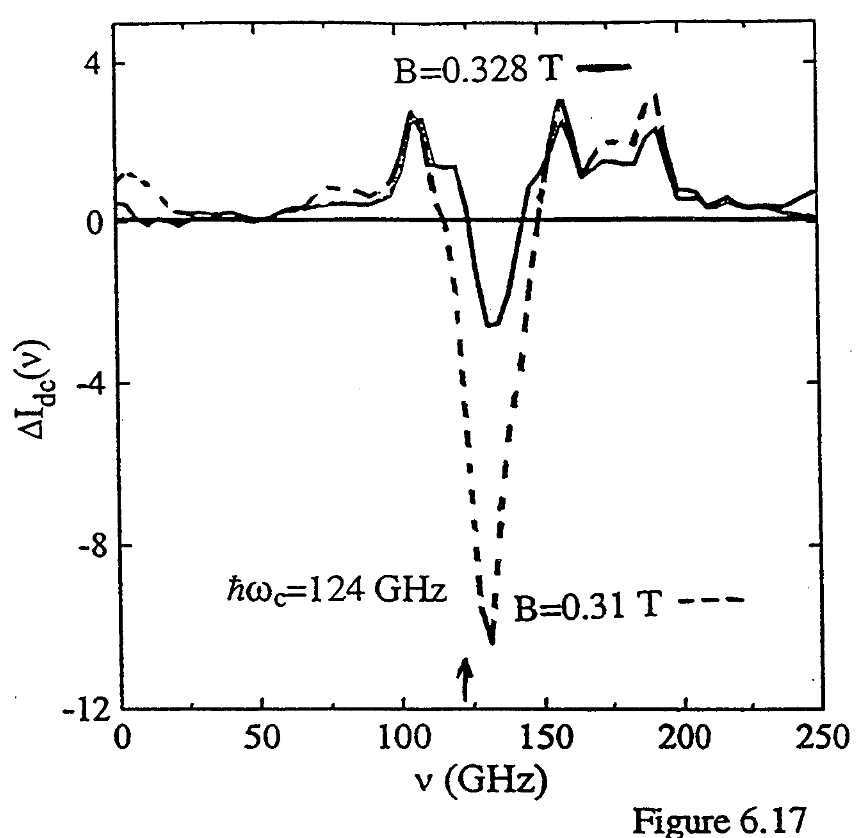


Figure 6.17

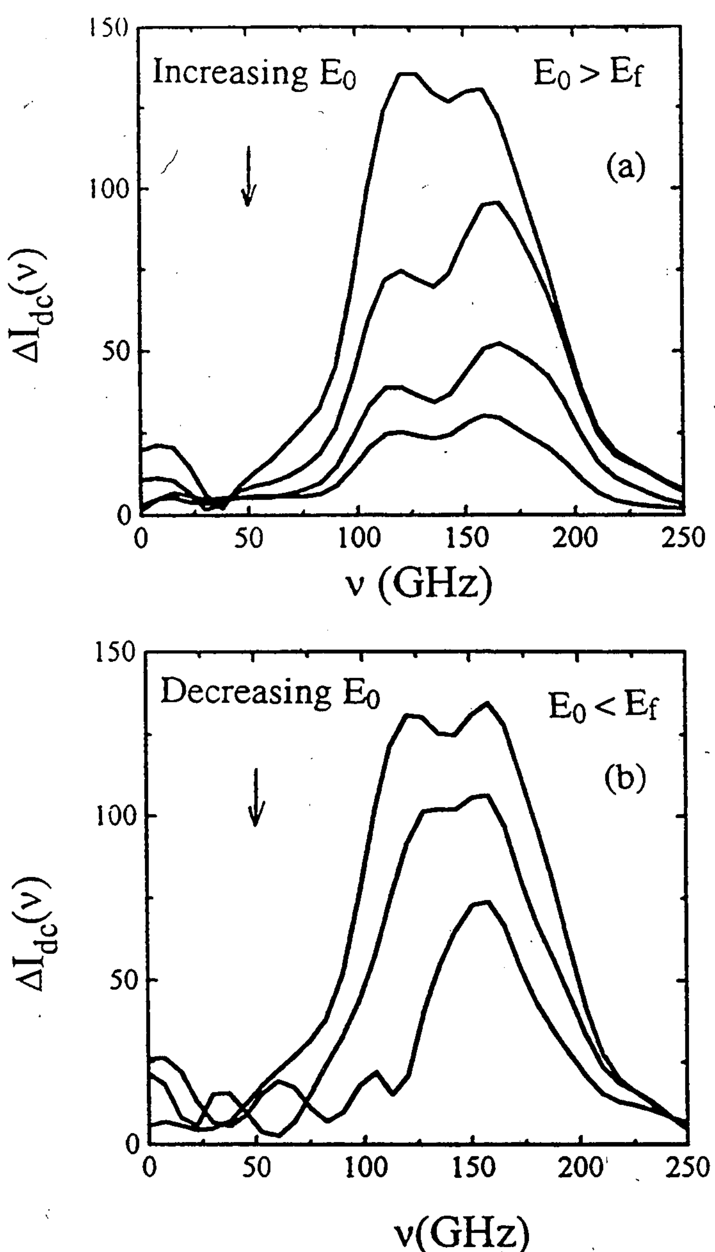


Figure 6.18

# Chapter 7

# Conclusions

In this thesis we began in Chapter 2 with the basic information needed to design terahertz pulsed sources and described how these sources can be implemented in a terahertz time-domain interferometer (THz-TDI) to characterize the dynamic response of an arbitrary nonlinear device. This technique is absolutely general and may be applied to any device that exhibits a non-linearity in its I-V characteristic. We believe that this technique will find its niche in probing devices which operate in exotic environments at ultralow millikelvin temperatures and high magnetic fields.

In Chapter 4 we applied the THz-TDI technique to the measurement of the linear response of the quasiparticle current in a $Nb/AlO_x/Nb$ SIS tunnel junction for frequencies from 75 to 200 GHz. Our results confirm the crucial role the quantum susceptance plays in determining the linear response. Our results are in full agreement with the linear theory for photon assited tunneling described in Chapter 3. In addition, we have described

preliminary nonlinear spectroscopic measurements that may prove useful in the future for measuring the quasiparticle lifetime.

In Chapter 6 we further demonstrated the generality of the THz-TDI technique by applying this method to measuring the dynamic response of a quantum point contact. This experimental study has shown that photon assited transport (PAT) provides a consistent explanation for the *dc* current induced across a tunnel barrier by terahertz radiation. We have made the first measurements of PAT in a tunnel barrier as a function of source-drain voltage, gate voltage, frequency, and magnetic field.

The experiments on the quantum point contact described in this thesis represent only the beginnings of an entire field of study devoted to probing the *ac* response of mesoscopic devices. In the future we fully expect the THz-TDI technique pioneered by our group at Berkeley to become the method of choice in probing the dynamics of semiconductor nanostructured devices in the terahertz frequency domain. Indeed other research groups are beginning to recognize the power of the interferometric method. For example van der Weide *et al* at the Max-Plank-Institute has begun to probe the picosecond response of a quantum dot using a modified form of our interferometric technique [7.1]. A number of interesting dynamical phenomena have been theoretically predicted in a quantum dot, such as the appearance of Rabi like oscillations [7.2]. In addition to the group at Max-Plank, J. Allam's group at Hitachi Cambridge in Europe has initiated a program to apply the interferometeric technique to measure the time of flight of electrons in a mesoscopic nanostructure [7.3].

## 7.1 References

[7.1] D. W. van der Weide, R.H. Blick, F. Keilmann, R.J. Haug, K. von Klitzing, K. Eberl, OSA Conference on Quantum Optoelectronics-1995 Technical Digest **14**, 103 (1995).

[7.2] N. S. Wingreen, A-P. Jauho, Y. Meir, *Phys. Rev B* **48**, 8487 (1993).

[7.3] Private communication with J. Allam of Hitachi Cambridge Laboratory, Hitachi Europe Ltd.

LAWRENCE BERKELEY LABORATORY
UNIVERSITY OF CALIFORNIA
TECHNICAL INFORMATION DEPARTMENT
BERKELEY, CALIFORNIA 94720